Biophysical Simulation of the Functional Magnetic Resonance Signal Formation in Realistic Neurovascular Networks

Dissertation

zur Erlangung des Grades eines

Doktors der Naturwissenschaften

der Mathematisch-Naturwissenschaftlichen Fakultät
und
der Medizinischen Fakultät
der Eberhard-Karls-Universität Tübingen

vorgelegt

von

Mario Gilberto Báez Yáñez, M. Sc.

aus Ciudad de México, Mexiko

Tübingen, Juni 2018

25 Oktober 2018

Tag der mündlichen Prüfung: .....

Dekan der Math.-Nat. Fakultät: Prof. Dr. W. Rosenstiel
Dekan der Medizinischen Fakultät: Prof. Dr. I. B. Autenrieth

1. Berichterstatter: Prof. Dr. Klaus Scheffler
2. Berichterstatter: Prof. Dr. Andreas Bartels

Prüfungskommission: Prof. Dr. Klaus Scheffler
Prof. Dr. Andreas Bartels
Prof. Dr. Dieter Kölle
Dr. Xin Yu

Erklärung / Declaration:

Ich erkläre, dass ich die zur Promotion eingereichte Arbeit mit dem Titel:

"Biophysical Simulation of the Functional Magnetic Resonance Signal Formation in Realistic Neurovascular Networks",

selbständig verfasst, nur die angegebenen Quellen und Hilfsmittel benutzt und wörtlich oder inhaltlich übernommene Stellen als solche gekennzeichnet habe. Ich versichere an Eides statt, dass diese Angaben wahr sind und dass ich nichts verschwiegen habe. Mir ist bekannt, dass die falsche Abgabe einer Versicherung an Eides statt mit Freiheitsstrafe bis zu drei Jahren oder mit Geldstrafe bestraft wird.

I hereby declare that I have produced the work entitled

"Biophysical Simulation of the Functional Magnetic Resonance Signal Formation in Realistic Neurovascular Networks",

submitted for the award of a doctorate, on my own (without external help), have used only the sources and aids indicated and have marked passages included from other works, whether verbatim or in content, as such. I swear upon oath that these statements are true and that I have not concealed anything. I am aware that making a false declaration under oath is punishable by a term of imprisonment of up to three years or by a fine.

Tübingen, den..... 25 Oktober 2018 …….....

Datum / Date Unterschrift / Signature

“Would you tell me, please, which way I ought to go from here?”

“That depends a good deal on where you want to get to,” said the Cat.

“I don’t much care where–” said Alice.

“Then it doesn’t matter which way you go,” said the Cat.

“–so long as I get SOMEWHERE,” Alice added as an explanation.

“Oh, you’re sure to do that,” said the Cat, “if you only walk long enough.”

— Lewis Carroll

Contents

List of Figures

Abbreviations & Physical constants

MRI	Magnetic Resonance Imaging
MR	Magnetic Resonance
NMR	Nuclear Magnetic Resonance
B_0	Static Magnetic Field
B_1	Radiofrequency pulse applied to the system
BOLD	Blood Oxygenation Level-Dependent
CBV	Cerebral Blood Volume
CBF	Cerebral Blood Flow
CMRO2	Cerebral Metabolic Rate of Oxygen
FID	Free Induction Decay
SDR	Static Dephasing Regime
DNR	Diffusion Narrowing Regime
GE	Gradient Echo
SE	Spin Echo
bSSFP	Balanced Steady State Free Precession
TR	Repetition Time
TE	Echo Time
RF	Radio Frequency
PET	Positron Emission Tomography
GPU	Graphics Processing Unit
RAM	Random Access Memory

Gyromagnetic ratio (γ) 267.5E6 [rad/s]

Summary

The human brain is one of the most complex living systems. The scientific study of the brain's anatomy and neurophysiology are fundamental to understand the basic principles of mental processes such as cognition and behavior.

For this reason, in the endeavor to investigate the underlying neural mechanisms that drive these processes, the neuroscientific research has employed all the available technological resources and methodologies from different fields like anatomy, histology, electrophysiology, neurobiology, etc. Likewise, great advances have been provided by neuroimaging techniques such as PET and MRI, in order to comprehend the neural activity and the metabolic reactions that occur in the central nervous system.

In particular, functional MRI provides an indirect measurement of the neural activity throughout local hemodynamic changes, thus related to the neurovascular coupling, as a response to a particular task-evoked stimulus. This MR signal behavior modulated by oxygenation level changes is better known as the BOLD signal.

Although progress has been done in order to understand the BOLD signal change under well-defined nonrealistic vascular geometries, on the other hand, realistic neurovascular networks might give valuable information to resolve the influence on the BOLD signal evolution from a particular vascular tissue and specific hemodynamic responses.

As identified by one of the pioneer's publication in the fMRI field, Ogawa claimed the importance to address an accurate quantitative picture of the nature of the BOLD signal change throughout the use of realistic vessel geometries, intrinsic cerebral hemodynamic responses and the interaction of magnetic perturbed spins to understand the functional signal [Ogawa et al 1993].

Overall, a complete physiological model might give beneficial insights in order to optimize the BOLD signal acquisition parameters, to improve the functional MRI pulse sequences and to quantify the biophysical components that drive this signal.

In addition, the relation between the MR physics and the neurovascular structure presuming hemodynamic responses is crucial to the interpretation of a brain activation map. Likewise, the spatial specificity of the pulse sequence and the tissue contribution to the BOLD signal play an important role on the precision and analysis of the functional images.

Thus, the problem can be resumed to that the BOLD fMRI is a signal that shows a strong dependence on anatomical characteristics and physiological parameters. So far, oxygen concentration changes across different segments of blood vessels and cerebral blood volume variations need to be properly modeled in order to analyze the specific tissue contribution to the functional MR signal.

In this context, among several essential works, the approximations and results obtained by Ogawa et al in 1993, Yablonskiy and Haacke in 1994, Boxerman et al in 1995, Kiselev et al in 1999, Scheffler et al 2001 and Bieri et al in 2007 gave motivation to the development of this thesis.

In these publications, the MR signal formation was analyzed for cylindrical or spherical perturbers, as a geometric alternative model to mimic the neurovascular tissue. Besides, the evolution of the MR signal for different pulse sequences and the impact of physiological properties of the mesoscopic structure were studied.

Furthermore, they demonstrated that the MR signal exhibits particular characteristics influenced by the local frequency variations, produced by susceptibility differences of the tissues, and thermal motion that might therefore be exploited to quantify and infer valuable mesoscopic information.

An additional enthusiasm that drives this work is that, until recently, the three-dimensional vascular network topology of the neocortex is becoming available to be studied in detail due to new imaging technologies like two-photon microscopy.

This imaging method enables the possibility to obtain images from the neurovascular structure at submicron resolution.

In order to extend the analysis of the BOLD signal change obtained by randomly oriented cylinders and spheres, throughout this thesis, the geometrical features of a realistic neurovascular network as well as the biophysical effects related to the hemodynamic response and thermal motion were investigated by means of Monte Carlo simulations in pursuance to resolve the functional MR signal formation.

In the Introduction of this thesis, I made a small recapitulation on the MR physics and spin dynamics; magnetic susceptibility and thermal motion as crucial modulators of the BOLD signal behavior. In addition, a summary of the problem and the aims of the project.

Therefore, I described the importance of the use of the Monte Carlo method to calculate the MR signal under nonrealistic vascular models. I summarized the seminal analytical and numerical results that provide important insights to characterize the main parameters that influence the MR signal formation.

Finally, I described the importance of the use of realistic neurovascular structures in order to disentangle the specific tissue contribution and the direct impact on the BOLD signal change.

In Chapter II, I summarized the results obtained throughout this work, that are attached in the form of Appendices.

Lastly, in Chapter III, I wrote a general discussion and an overview of all the work elaborated in the development of this thesis.

Chapter I. Introduction

1. Synopsis

Nowadays, MRI is the best available technology to obtain images from soft living tissues. In particular, the neuroscientific research relies on this technique due to the offered advantages compared to other imaging modalities, for instance, to study the anatomy with high spatial resolution and to investigate the metabolic processes involved in the function of the brain.

Owing to its non-invasive characteristics, MRI gives the opportunity to examine metabolic processes *in-vivo* on the same experimental subject at different time periods. In addition, clinical studies have also been benefited from this image technology to understand both health and disease in a better manner.

The MRI has been developed during the last 45 years with strong encourage to quantify characteristics of the acquired signal associated to the mesoscopic structure, to improve the spatial and temporal resolution and to optimize the pulse sequence acquisition.

In order to address these challenges (quantify, improve and optimize), a complete scheme of the fundamental physics behind the process of MR signal generation must be comprehended.

Throughout this work, I tried to use the simplest biophysical representation, in order to simulate the evolution of the MR signal, to describe the interaction between soft living tissues (assuming their inherent magnetic and biological properties) and controlled magnetic fields.

1.1. A Voxel as a Simulation Universe

For the sake of simplicity, a cube is presumed as our simulation universe in analogy to a voxel acquired in a three-dimensional MR image. The dimension of the cube varies from some millimeters to hundreds of micrometers.

The voxel contains one or several types of tissues (perturbers) with a generic geometrical shape and inherent magnetic properties. The perturbers occupy a specific volume fraction denoted by $\eta = v/V$, where v is the volume occupied by the tissues or perturbers and V is the volume of the simulation voxel. Throughout this work, the term tissue or perturber refers to the same connotation.

It is worth to note, that all tissues are magnetic, i.e. they have the capability to interact with magnetic fields and this magnetization depends on their inherent physical properties [Jackson D 1999]. So far, when the cube is placed in a static homogeneous magnetic field represented by B_0, two physical effects take place to generate the MR signal.

Inside a strong magnetic field and at thermal equilibrium, a nuclear population with ½-spin value "feel" an attraction to adjust their intrinsic random oriented magnetic moment to a definite orientation, parallel (low-energy) or antiparallel (high-energy), with respect to the direction of the imposed magnetic field (Curie's law).

Due to a slightly difference in this energy-state polarization, a longitudinal macroscopic magnetization vector, oriented in the direction of the magnetic field B_0, is generated by the superposition of all the nuclear magnetic moments inside the voxel. The longitudinal macroscopic magnetization is calculated by the sum of the magnetic moments of the nuclear spin density immerse in the simulation cube,

$$\vec{M} = \frac{1}{V}\sum_{l}\vec{\mu}_l \qquad (1)$$

where $\vec{M}$ is the longitudinal macroscopic magnetization, $\vec{\mu}_l$ the magnetic moment of the l-nuclear spin and V is the volume of the cube [Ziener CH 2007]. As already mentioned, this vector is aligned to the orientation of the strong magnetic field and its magnitude grows exponentially by a certain time constant denoted by T1, until it reaches a steady state.

Therefore, in order to generate a measurable signal, the longitudinal magnetization is manipulated by the use of an external magnetic pulse sequence [Haacke et al 1999, Bloch 1946].

In a simulation, the nuclear spin density is relevant for an accurate approximation of the MR signal. For simplicity, I assumed that the number of simulated nuclear spins were plenty adequate to estimate the MR signal evolution in a given model, and it was similar to a nuclear spin density value of 1.

The second effect produced by the interaction of the nuclear spin with the magnetic field B_0 is the precession motion displayed by the nuclear spins at a particular frequency (see Figure 1). The Larmor frequency depends on the magnitude of B_0 and is calculated by $\omega = \gamma \cdot B_0$, where γ is the gyromagnetic ratio [rad/s] and B_0 is the static magnetic field [Tesla].

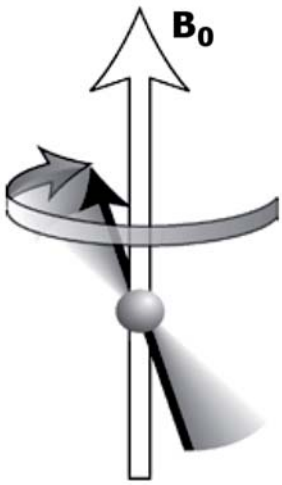

Figure 1. Depiction of a spin magnetic moment vector (black arrow) and its intrinsic precession (gray arrow; clockwise direction) with respect to the main magnetic field B_0 represented by the big white arrow.

In a simulation, a completely homogenous magnetic field B_0 is assumed. Therefore, all nuclear spins precess at the same frequency, although they exhibit a different synchronization in the precession [Ziener CH 2005].

In this sense, to generate a measurable signal, an orthogonal time-dependent RF magnetic pulse is applied to the system to match the precession motion of all nuclear spins. The RF pulse creates a magnetization vector in the transversal plane of the reference frame as a consequence of the alignment of all nuclear spin phases. This magnetization is measured by means of a coil tuned at the Larmor frequency, because the magnetization vector generates an alternating magnetic flux density capable to be detected by any nearby coil (Faraday's law of induction) [Bernstein 2004].

When the time-dependent RF pulse is switched off, the signal detected is exponentially vanished due to a loss of coherence between spin precession as result of local inhomogeneities in the magnetic field and intrinsic thermodynamic interactions. The transversal magnetization disappears over time with a certain time constant known as transverse relaxation time (T2* or T2 dependent on the pulse sequence), and thus the nuclear spin system recovers to its thermal equilibrium state generating again a longitudinal magnetization [Levitt 2001].

1.2. The Bloch-Torrey Equation

In general, to model spin interactions at a mesoscopic scale (understanding for mesoscopic scale a scale-order larger than the microscopic level but smaller than the voxel size), it is important to understand the evolution of the magnetization of the nuclear spin throughout the Bloch equation.

The Bloch equation is fundamental to describe the time-dependent magnetization behavior of the interactions between the external magnetic fields (B_0 and B_1) and the intrinsic relaxation terms (T1 and T2) [Bloch 1946]. Nevertheless, the Bloch equation does not account for a number of sceneries that occur in a real MR experiment. For instance, neither the dephasing of spins produced by susceptibility effects nor the consequences related to thermal motion.

In particular, the MR signal is a complex result from the interaction of spins in thermal motion within a local inhomogeneous magnetic environment, produced by susceptibility effects, and external controlled magnetic pulse sequences.

For this reason, the study of MR signal formation assuming all biophysical variables becomes more challenging and quite interesting to investigate. Likewise, the improvement on the pulse sequences, optimization of signal acquisition and quantification of inherent biophysical features from the measured signal might contribute to a better characterization and understanding of functional and metabolic biological processes [Kiselev et al 1999, Grebenkov DS 2007].

Recent investigations have proved that the obtained MR signal displays a particular behavior for each voxel, referred as the *fingerprint MR signal*, that depends on the embedded tissues inside the voxel, the pulse sequence and the acquisition parameters [Ma et al 2013, Asslaender et al 2017].

In a general scheme, cluster of voxels share some signal characteristics but, in specific, each voxel generates a particular MR signal transient correlated to the mesoscopic structure and the associated biophysical variables. Due to this particularity of the signal, the fingerprint MR behavior opens the possibility to extract features of the mesoscopic composition, such as the susceptibility effects induced by the system under investigation or the structure and arrangement of tissues through the analysis of the diffusion motion [Buschle et al 2017, Puckett et al 2016].

In this context, with the aim of characterizing the MR signal at a mesoscopic level, as well as the BOLD signal change, the time evolution of the magnetization is well described by the Bloch-Torrey equation [Torrey 1956].

$$\frac{d}{dt}m(r,t) = \left[D\nabla^2 + i\omega(r(t)) - \frac{1}{T_2}\right] m(r,t) \qquad (2)$$

This differential equation approximates the behavior of the nuclear spin magnetization $m(r,t)$ undergoing thermal motion, considered in the term $D\nabla^2$

where D is the coefficient of diffusivity, in a spatially-varying magnetic field $\omega(r(t))$. The equation also takes the intrinsic thermodynamic relaxation process T2 of the tissue under investigation into account.

For an ensemble of spins, the MR signal emitted by a voxel is approximated by the average of all the nuclear spin contributions,

$$S(t) = \frac{1}{N} \sum_{spin=1}^{N} e^{-t/T2}\, e^{-i\,\varphi_{spin}(r,t)} \qquad (3)$$

where $\varphi(r,t) = \int_{t=0}^{TE} \omega(r(t))$ is the nuclear spin phase accumulated over time, $S(t)$ is the signal detected and N is the number of simulated spins.

The phase $\varphi(r,t)$ is the most important concept in the characterization and quantification of MR signals and is fundamental in the image contrast of soft living tissues. Further, the phase $\varphi(r,t)$ is the central element of investigation in the analysis of BOLD fMRI signal changes.

For simplicity, the dephasing generated by the spatially encoding gradient system is neglected throughout this thesis. This assumption does not affect the resultant MR signal calculations by the fact that the size of the magnetic perturbers and hence the magnetic induced variations are much smaller than the size of the simulation voxel [Yablonskiy et al 1994].

Therefore, the exact solution of the Bloch-Torrey equation of a certain ensemble of perturbers distributed in a random position inside the voxel is mathematically cumbersome to approximate. However, there are some analytical and numerical approximations that offers an estimation of the MR signal behavior for a particular problem. Hence, the evolution of the magnetization through the Bloch-Torrey equation is fundamental to solve due to its sensibility to a particular set of biophysical variables in the formation of the BOLD fMRI signal.

1.3. Magnetic Susceptibility and Local Inhomogeneous Magnetic Field

A bunch of electrons in a molecule or atom produces a systematic cancellation of their spin magnetic moments for each pair. If an atom contains unpaired number of electrons, the 'solitary' electron tends to align with the external magnetic field and it thus generates an increment on its own magnetic moment. As a consequence of this effect, a modification on the local magnetic field is induced.

As pointed out by Haacke, the electron spin moment is much larger than the nuclear spin moment (~220 times larger) [Haacke 1999]. Therefore, the local magnetic field deviate substantially from the applied magnetic field. This effect is better known as magnetic susceptibility.

In this sense, susceptibility differences in tissues are used in some MRI applications such as: functional magnetic resonance imaging, susceptibility-weighted imaging, quantitative susceptibility mapping and susceptibility tensor imaging [Belliveau et al 1990].

The local magnetic disturbance is calculated by means of the relation

$$\vec{B}_{0mod} = \chi \vec{B}_0 \qquad (4)$$

where $\vec{B}_{0mod}$ is the local modified magnetic field and $\vec{B}_0$ is the applied homogeneous magnetic field. The magnetic susceptibility χ of a tissue or any substance is proportional to a constant or a particular spatial form, for instance the magnetic dipole form.

As mentioned before, all substances and tissues are magnetic and thus they have the capability to interact with magnetic fields, although this magnetization depends on their inherent physical properties. So far, if a biological tissue is placed in a homogeneous magnetic field, dipolar-like effects are created inside and around the

tissue (see Figure 2). This results in a local disturbance of the magnetic field and a modified Larmor frequency of the spins.

It is important to note, that the magnetic susceptibility produces a very small effect, i.e. the Larmor frequency of the spins is deviated in the order of tens to hundreds of Hz, dependent on the magnetic properties. However, such small variations are detected by means of magnetic resonance as a modification on the inherent T2 relaxation time of the tissue under investigation.

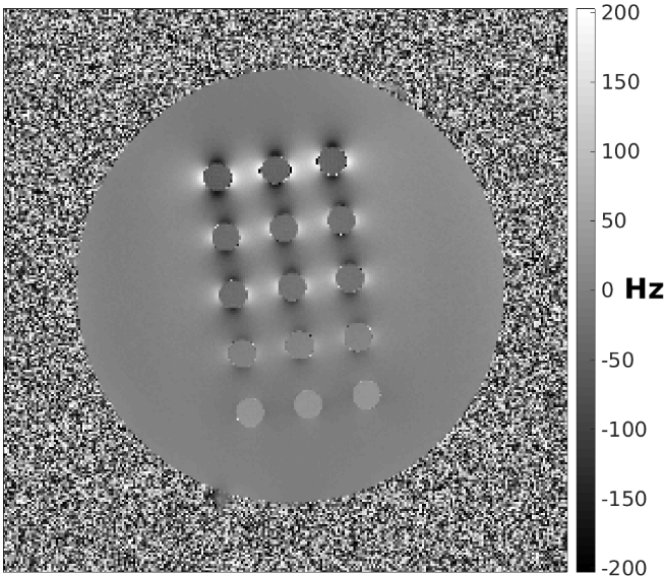

Figure 2. Susceptibility frequency map produced by Dy-DTPA with different concentrations [0 mM, 1.25 mM, 2.5 mM, 3.75 mM and 5mM] at 9.4 Tesla. It is possible to observe the dipole effect produced by the susceptibility difference between the solution with Dy-DTPA and the buffer solution (upper row). Upper row contains water [0 mM Dy-DTPA]. Bottom row contains the same concentration as the buffer solution [5mM Dy-DTPA]. An ascending gradient (from upper row to bottom row) of Dy-DTPA concentration is analyzed in each row.

The consequence of the local magnetic field variation produces a direct influence on the MR signal evolution as an extra-attenuation, due to an accelerated dephasing of the spin and therefore a faster loss of coherence. This dumping factor is known as the R2' (= 1/T2') relaxation time. An important property of the R2' is that, under

certain biophysical conditions and pulse sequences, the influence of this factor on the MR signal, can be reduced or completely eliminated [Hahn 1950, Kiselev et al 2002].

In the particular case of functional MRI, the temporal changes of the signal are correlated to dephasing of the spin system given by the local magnetic field variations [Fujita 2001]. The magnetic field modifications are produced by changes in the oxygen concentration of the neurovascular network triggered by a neural activation. Owing to that, hemoglobin contained in the red blood cells gives a small paramagnetic effect in its oxygenated state and an enlarged paramagnetic effect in its deoxygenated state. The paramagnetic effect is linearly correlated with the level of oxygenation. This is the basis of functional magnetic resonance imaging and it is better known as the blood oxygenation level-dependent (BOLD) contrast [Owaga et al 1993].

In a simulation scheme, blood can be approximated as a two pool model (plasma and red blood cells) [Grgac K et al 2013, Blockley et al 2008]. The volume fraction occupied by red blood cells is known as the hematocrit level and it is approximately 40% in healthy human blood [Yablonskiy et al 2012]. The susceptibility difference between neurovascular tissue (blood carrier) and the surrounding medium (brain tissue) is calculated according to $\Delta\chi = (0.273\,ppm * Htc * (1 - oxygenation\,level))$, where Htc is the hematocrit level. The oxygenation level depends on the type of vascular tissue (artery, capillary or vein) and the intrinsic hemodynamic response [Brooks et al 1995].

1.4. The Brownian Motion of Spins

Life is motion. Living tissues show a dynamical exchange of compounds through a physical process described by diffusion. Molecules move because of their own thermal energy and therefore it also can be considered as they are colliding with each other. Each collision results in a change in the motion direction of every

molecule and the overall process is well described by a stochastic random walk approximation. This process is also known as Brownian motion of molecules [Callaghan 1997].

Diffusion motion was described mathematically for the first time in 1905 in one of the most extraordinary papers of A. Einstein [Einstein 1905]. The major contribution of this paper is the description of the random motion of molecules and the relevant equation to calculate the mean distance exhibited by any atom or molecule by means of statistical approaches.

Diffusion is of fundamental importance in biological systems, as it forms the mechanism by which most of the molecules and chemical signals are transported in a tissue [Beaulieu 2002].

A particle diffusing in a confined medium is a general model for a large number of physical, chemical and biological processes. Mathematically speaking, diffusion is modelled as a stochastic process with particular motion characteristics limited by geometrical restrictions [Grebenkov DS 2007].

In the process of biological diffusion, a substance tends to move from an area of high concentration to an area of low concentration until its concentration becomes equal throughout the space. Molecules can move through the biological tissues by diffusion, whereas some molecules also can diffuse across them [Guyton and Hall 2015]. Each individual substance in a solution or tissue has its own concentration gradient, independent on the concentration gradients of other substances, and will diffuse according to that gradient. In this sense, a compound of tissue exhibits different diffusion rates and directions for different molecules and cells. For example, oxygen exchange between blood vessels and neurons is transferred by diffusion exchange, while at the same time, carbon dioxide moves out in obedience to its own concentration gradient.

In general, the MR signal evolution is dependent on all the molecules depicting motion across a spatially-varying magnetic field, collisions between each other and

the tissue barriers as motion constrain [Le Bihan et al 2007, Barzykin 1998, Bieri et al 2012].

1.5. Monte Carlo Method

The Monte Carlo method is a nondeterministic numerical method, i.e. probabilistic or stochastic, and it is employed to approximate the solution of a mathematical or physical problem. The solution of a particular set of variables is estimated by employing sequences of random numbers. The Monte Carlo method was developed by Ulam and von Neumann at the end of the Second World War (~1946) in order to study the diffusion of neutrons in fissionable material [Rhodes R. 1986].

Based on the fact that the Brownian motion can be mathematically described as a stochastic process, the generation of random numbers produced by a Gaussian distribution simulates the random thermal motion of magnetized molecules or spins in a given medium.

Likewise, the Monte Carlo method can be applied independently of the geometrical structure under investigation or the dimensionality of the problem (1D, 2D or 3D) and it is possible to constrain the motion to certain boundary conditions. For example, the motion can be hindered, restricted or unrestricted to a confined medium or exhibit particular motion characteristic such as an isotropic or anisotropic diffusion.

For the reason that, the Monte Carlo method is a statistical approach, the number of spins or simulation averages has a crucial impact on the MR signal outcome. The larger the number of spins, the more accurate is the simulation. An error factor can be determined by the relation $1/\sqrt{N}$, where N is the number of simulated spins or averages [Hall M 2009].

1.6. Summary and aims of the project

Although progress has been done in order to understand the BOLD signal change under well-defined nonrealistic vascular geometries, on the other hand, realistic neurovascular networks might give valuable information to resolve the influence on the BOLD signal evolution from a particular vascular tissue and specific hemodynamic responses.

Among several essential works, the approximations and results obtained by Ogawa et al in 1993, Yablonskiy and Haacke in 1994, Boxerman et al in 1995, Kiselev et al in 1999, Scheffler et al 2001 and Bieri et al in 2007 gave motivation to the development of this thesis.

In these publications, the MR signal formation was analyzed for cylindrical or spherical perturbers, as a geometric alternative model to mimic the neurovascular tissue. Besides, the evolution of the MR signal for different pulse sequences and the impact of physiological properties of the mesoscopic structure were studied.

An additional enthusiasm that drives this work is that, until recently, the three-dimensional vascular network topology of the neocortex is becoming available to be studied in detail due to new imaging technologies like two-photon microscopy. This imaging method enables the possibility to obtain images from the neurovascular structure at submicron resolution.

Therefore, in order to extend the analysis of the BOLD signal change obtained by randomly oriented cylinders and spheres, the geometrical features of a realistic neurovascular network as well as the biophysical effects related to the hemodynamic response and thermal motion were investigated in pursuance to resolve the functional MR signal formation.

Hence, in this dissertation, the functional MR signal evolution associated to a nonrealistic and realistic neurovascular networks, assuming local frequency variations related to susceptibility differences between tissues and thermal motion,

was analyzed by means of Monte Carlo simulations. For such a purpose, this project addresses the following particular aims, related to the work attached in the manuscripts:

- To develop a Monte Carlo algorithm that simulates the thermal motion of magnetized spins and the local frequency variation induced by a generic or realistic vascular tissue structure, in order to obtain the functional MR signal associated to the model under investigation.

- To understand the impact of the features associated to the topology of the model such as radius size of vessels, orientation with respect to the magnetic field, volume fraction, etc, and the influence on the BOLD signal formation.

- To analyze the sensibility and selectivity of the pulse sequences to hemodynamic responses that influence the BOLD signal change.

- To investigated the dependency of the functional signal change to different imaging parameters like echo time, repetition time, alpha RF excitation, and the impact of the magnetic field strength.

- To disentangle the particular contribution of tissue to the MR signal evolution, particularly, the microvascular and macrovascular contribution to the BOLD signal change for different pulse sequences.

2. Functional MR Signal Formation in a Non-Realistic Neurovascular Network

An exact solution of the Bloch-Torrey equation (equation 2) is mathematically cumbersome to estimate, even in a simple and well parametrized geometry. So far, boundary conditions and assumptions must be presumed. As an alternative, the Monte Carlo method provides a numerical solution in order to approximate the MR signal outcome, taking complex geometrical structures and the intrinsic biophysical interactions into account. Moreover, numerical modelling can provide important insights to particular questions which inherently depend on various parameters defined by the system under investigation.

A distinctive disadvantage of the method is the long computational time required to approximate the MR signal to a specific set of parameters. The calculation can take a couple of hours to some days, dependent on the geometrical model, biophysical interactions and the pulse sequence parameters.

Nevertheless, some effort has been done in order to characterize the variables that influence the MR signal behavior in a BOLD experiment throughout analytical and numerical modeling.

A brief summary of the findings, that I consider fundamental for the development of this thesis, follows. I found important to review these contributions due to the high impact of the results towards to the understanding of the MR signal behavior and BOLD signal evolution. Moreover, this review contributes as a direct comparison to the obtained results.

Owaga et al 1993 calculated by means of Monte Carlo simulation the first insights of the contribution to the BOLD signal formation. In order to estimate the BOLD signal change, he simulated small compartments containing one vessel segment modeled by an infinite cylinder at different orientations.

So far, the basic principles of the BOLD contrast were discussed, such as the intravoxel dephasing of water protons in motion and the local inhomogeneites produced by the deoxyhemoglobin. Likewise, the impact on the transverse relaxation owing to biophysical and pulse sequence interactions.

One of the most important results of this work is the demonstration of the linear increasing behavior of the transversal relaxation R2 (= 1/T2) with respect to the volume fraction. Additionally, he claimed the importance of the use of ultra-high magnetic fields to increase the spatial resolution and enhance the contribution of different tissues.

Yablonskiy et al 1994 approximated by asymptotic methods an analytical solution for the free induction decay (FID), where neglected diffusion was assumed. On that publication they concluded, that the MR signal is modulated by the volume fraction and the level of susceptibility difference induced by the oxygenation. This result is only applicable in vascular tissues that exceed certain dimensions. The impact of the imposed magnetic field strength was also discussed. In addition, the static dephasing regime properties were established.

Boxerman et al 1995 used Monte Carlo simulations in order to complement in a more generic vascular model the MR signal evolution in contrast to the simple vascular model of Owaga. Based on a uniform distributed cylinder model, they calculated the impact of vessel radius on the transversal signal attenuation. Hence, they analyzed the impact of physiological parameters like different oxygen concentrations, volume fraction and the contribution of the perturber features at different echo times.

They concluded, that the intravascular signal is not a negligible contribution to the BOLD signal and sometimes might become dominant at low magnetic fields. Besides, the impermeable boundary condition of the cylinders does not affect in a gross manner the transversal dephasing. As already mentioned before, they confirm the linearly increasing signal attenuation exhibited by an increase of the volume fraction. Additionally, one of the most remarkable results of this publication is the

specificity of the SE pulse sequence to microvascular contribution and the large sensitivity to all vessel calibers of the GE pulse sequence.

Kiselev et al in 1999 extended the analytical approach of Yablonskiy and performed Monte Carlo simulation for the special case, where the effects of diffusion are weak (diffusion dephasing regime). The non-monoexponential time decay of the MR signal is introduced and thus the impact of short-time and long-time signal characteristics for the GE and SE are compared with previous results.

Finally, in 2001 the signal sensitivity in the transition-band of the balanced steady-state free precession (bSSFP) were analyzed by means of frequency shifts in the BOLD signal changes [Scheffler et al 2001]. An extended analysis of the properties of selectivity of the bSSFP in the passband were studied by means of Monte Carlo simulations and experimental approaches [Bieri et al in 2007].

On these publications, it is mentioned, that the zeroth integral of the balanced imaging gradients in bSSFP does not induce any extra-dephasing to the accumulated phase and the intrinsic characteristics of the inhomogeneity can be directly studied without any external distortion.

Further, bSSFP signal changes are dependent on the selection of pulse sequence parameters such as: the selection of flip angle or repetition time, the intrinsic biophysical properties T1 and T2 relaxation times, the size or shape of the perturber and the induced magnetic inhomogeneities.

One of the significant outcomes is the confirmation of bSSFP to be selective to contributions from small capillaries, i.e. contribution from several spin pathways performing an SE-like behavior and thus a selectivity for small vessel calibers.

2.1. Spheres and Cylinders as Magnetic Perturbers

In order to calculate the variations of the local frequency produced by a randomly distributed compound of tissues in a voxel, the equation (5) must be satisfied [Bauer et al 1999, Ziener et al 2006, Ziener et al 2007, Buschle et al 2015, Kurz et al 2006].

$$\omega(r) = \delta\omega \frac{\partial^2}{\partial z^2} \int_G \frac{d^3r'}{|r - r'|} \qquad (5)$$

where $\delta\omega = \gamma \cdot \Delta\chi \cdot B_0$ is the characteristic frequency shift, r and r' represents the spatial position of the perturber and the spatial evaluation point in a Cartesian coordinate system, respectively. This equation describes the spatial variation of the magnetic field at any spatial point of our simulation space. Nevertheless, the calculation of the magnetic field variation created by a set of perturbers with an irregular shape is not so straightforward and thus quite complicated to approximate.

However, the problem can be tractable with regular geometrical figures like spheres or cylinders. In particular, they can mimic the frequency variation induced by different types of magnetic perturbers like cells, fiber bundles or axons, contrast agents or neurovascular tissue [Audoly et al 2003]. Beyond the simplified geometrical shape, an additional advantage is the well-characterized dipolar effect produced by this particular geometry as consequence of the interaction with the imposed magnetic field.

In order to perform Monte Carlo calculations for a specific ensemble of magnetic perturbers, the local frequency variation must be determined at any spatial point of the voxel in a given coordinate system. This can be done in a continuous or a discrete space. The Monte Carlo method is not limited by the dimensionality of the problem, i.e. 1D, 2D or 3D approximations can be employed to estimate the solution.

The main difference of a continuous or discrete space approximation is the precision of the solution and the computational time required to obtain the MR signal. In the

continuous space approximation, the spatial frequency variation resolution is defined by the precision of the used datatype (integer or double). On the other hand, the discrete space approximation divides the voxel into a constrained number of sub-voxels or cells. The sub-voxel limitation is directly dependent on the memory RAM of the computer.

2.1.1. Continuous Space Approximation

If the spatial position of the *n-th* object of an ensemble of magnetic perturbers (randomly distributed and attached to a specific position) and the spatial position of the *i-th* spin in a given Cartesian coordinate system are known, it is straightforward to calculate the local Larmor frequency variation $\omega(r(t))$. The position of the spin and the magnetic perturber across the space are related by the vector $r(t)$. The total perturbation induced by the local frequency $\omega(r(t))$ on a single spin at every spatial and time point is given by the superposition of all perturber contributions [Kiselev et al 1998, Kiselev et al 2001].

In this context, the local frequency variation produced by a cylinder is well characterized by its magnetic dipole moment and is calculated by

$$\omega(r,\vartheta,\theta) = \gamma\, 2\pi\, \Delta\chi\, B_0 \frac{R^2}{r^2} \sin^2(\theta)\cos(2\vartheta)\,, \quad r > R \qquad (6)$$

$$\omega(\theta) = \gamma\, 2\pi\, \Delta\chi\, B_0 \cos^2(\theta - 1/3), \quad r \leq R \qquad (7)$$

where r and ϑ are the polar coordinates of the position of the *i-th* spin with respect to the *n-th* cylinder, R is the radius of the cylinder, γ is the gyromagnetic ratio [rad/s], $\Delta\chi$ is the susceptibility difference induced by the cylinder and the surrounding medium [ppm], B_0 is the imposed main magnetic field [Tesla] and θ is the angle between the magnetic field and the cylinder orientation.

On the other hand, the local frequency variation exhibited by a sphere perturber is calculated by

$$\omega(r,\vartheta) = \gamma\, 2\pi\, \Delta\chi\, B_0\, \frac{R^3}{r^3}\, 3\cos^2(\vartheta) + 1, \quad r > R \qquad (8)$$

$$\omega(r) = 0, \quad r \leq R \qquad (9)$$

where r and ϑ are the polar coordinates of the position of the *i-th* spin with respect to the *n-th* sphere, R is the radius of the sphere, γ is the gyromagnetic ratio [rad/s], $\Delta\chi$ is the susceptibility difference displayed by the sphere and the surrounding medium [ppm] and B_0 is the imposed main magnetic field [Tesla].

Notice, that the sphere does not exhibit any angular dependence with respect to B_0. Nevertheless, the cylinder depicts an orientation dependence with respect to the orientation of the main magnetic field. The maximum value is obtained when the cylinder is positioned orthogonal to the magnetic field.

2.1.2. Discrete Space Approximation

One of the most fundamental concepts in scientific computing is the translation of a physical problem into a discrete numerical treatment to make the computational application of algorithms feasible and to speed up the calculation time.

In this sense, the finite perturber method (FPM) is a fast calculation technique to approximate the local frequency variation produced by a generic geometry [Jenkinson et al 2004, Koch et al 2006, Marques et al 2004, Marques et al 2008, Pathak et al 2008]. The FPM calculates the local frequency variation given by a binary discrete model and a magnetic dipole kernel by means of properties of the Fourier transform in order to solve equation 5.

Briefly, the FPM method relies on the convolution between the model and the kernel in the space domain. To simplify the calculations, the convolution is tractable by means of the Fourier transform of the model and the kernel. Then, the multiplication of these Fourier space domains is calculated and back Fourier transformed in order to obtain the convoluted space domain. The resultant is the spatial frequency variation given by a spherical perturber (kernel) in each non-zero element of the model. Mathematical details are fully described in [Marques et al 2004, Pathak et al 2008].

The FPM provides a fast calculation of the local frequency variation. However, this method suffers from boundary condition problems due to the circular convolution employed in the calculation. Therefore, at the borders of the perturber, the frequency variation is miscalculated. This drawback is not exhibited in the continuous space approximation. As a consequence of these inaccuracies, an error factor must be presumed in the FPM map at any given grid point. In contrast, the continuous space approximation might be considered as the ground truth of the local frequency variation given by a set of perturbers.

2.2. MRI Sequences (GE, SE and SSPF)

As mentioned in previous sections, in order to generate a MR signal capable to be detected from an ensemble of tissues with a nearby coil tuned at the Larmor frequency, an oscillating time-dependent RF pulse must be applied to the system. Based on that, the magnitude and phase of the MR signal are dependent on the exposition time duration and phase applied through the RF pulse.

For simplicity, I excluded the encoding gradient system and I made reference as acquisition sequence or pulse sequence only to the RF pulse applied to the ensemble of spins (unless other statement is mentioned).

The gradient echo (GE) is the most basic pulse sequence, where a 90° RF pulse is applied to the system under investigation. An important detail is that the magnitude

of the RF pulse in a gradient echo does not need to be 90° exclusively. Any RF pulse can created transversal magnetization but with different signal magnitude.

The RF pulse synchronizes the precession of the spins. When the RF pulse is switched off, by means of thermodynamic relaxation and local field inhomogeneities, the spin system recovers to its thermal equilibrium state and the magnetization decreases as an exponential decay described by the Bloch equation [Bloch 1946]. At a certain time, known as the echo time (TE), the magnitude and the phase of the transversal macroscopic magnetization is sampled and translated into a pixel or voxel complex value.

Throughout this work, I did not describe the entire process of image generation, since the topic *per se* goes beyond of the scope of my thesis. Signal codification and image generation are well described on the Haacke's MRI or Bernstein's MR sequence books [Haacke 1999, Bernstein et al 2004].

The spin echo (SE) pulse sequence described by E. Hahn [Hahn 1950] applies a second RF pulse of 180° at the half of the echo time after the initial 90° RF pulse. The advantage of this MR sequence relies on the elimination or reduction of the dephasing contribution of the magnetic field variations and thus sampling a less disturbed MR signal at a certain echo time.

In contrast with the already mention pulse sequence, a multi-rapid RF pulse acquisition with an excitation at repetition times smaller than the relaxation times T1 and T2 of the tissue like the balanced or non-balanced steady-state free precession, has a completely different story.

The magnetization is influenced from different pathways and hence, the MR signal is a composition of diverse spin phase contributions [Scheffler 1999]. Moreover, the MR signal is dependent on stimulation parameters such as the repetition time (TR) and the excitation flip angle (FA). There are plenty review papers describing the complex magnetization behavior of spins under this sort of sequence [Carr 1958, Kaiser et al 1974, Scheffler 1999, Scheffler 2003, Scheffler et al 2001, Miller et al

2008, Miller 2010, Miller 2007, Ganter 2006, Bieri et al 2007, Bieri et al 2013, Bieri et al 2011].

2.3. Results

In the present section I show results that I consider fundamental to review but also, they describe the importance of a nonrealistic vascular model in order to study the BOLD signal formation. Likewise, to demonstrate a direct comparison of the obtained results in this thesis with the well-established analytical and numerical published results.

Figure 3 depicts a rendered simulation model filled with uniform distributed spheres, parallel uniform cylinders and randomly distributed and oriented cylinders with a constant radius. The magnetic perturbers occupy a certain volume fraction. It is worth to mention that the size of the voxel is dependent on the volume fraction and the selected characteristic of the magnetic perturbers. Unless other property is stated, the perturbers in the simulation models throughout this thesis are assumed of being impermeable, the spins are considered to move freely around the external space and the thermal motion is presumed to be isotropic.

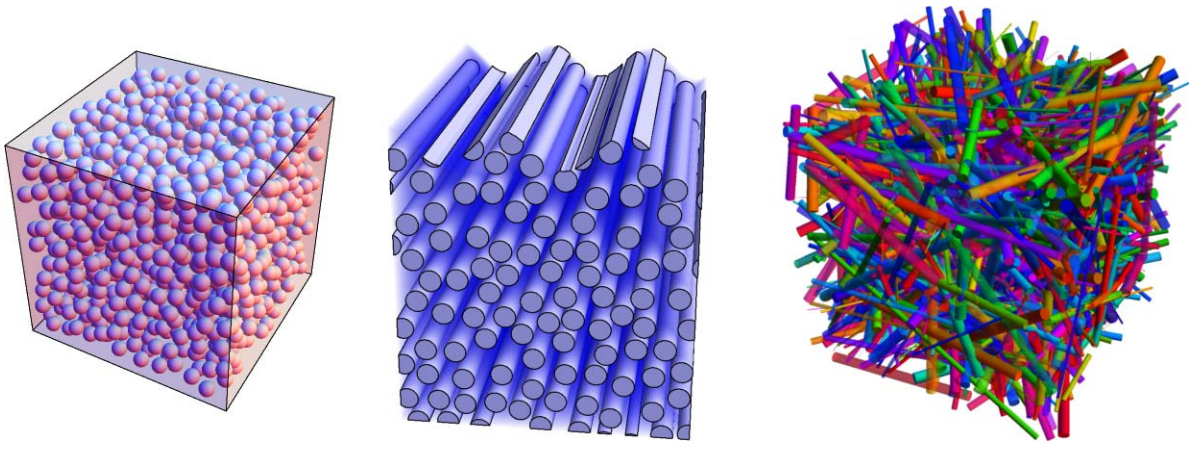

Figure 3. Representation of a simulation model filled with uniform distributed spheres, uniform distributed parallel cylinders and randomly distributed cylinders, respectively. The volume fraction is 5%. The perturbers display the same radius.

When the simulation voxel is placed inside a strong magnetic field, susceptibility differences are induced by the magnetic perturbers and the surrounded medium. As mentioned in the last section, the calculation can be performed by a continuous or discrete method.

The calculation of the inhomogeneous magnetic field in the continuous space approximation shows a higher precision of the frequency variation at every spatial point. Nevertheless, for this method a large computational time is required to calculate the influence of the *n-th* perturber to the MR signal evolution at every time step.

On the other hand, in the discrete space (FPM approximation) the simulation voxel is subdivided in a particular number of subvoxels and the local frequency variations are calculated by means of the FPM algorithm. With the help of element indexation, the calculation of the influence on the MR signal is much faster, but with a lower precision in the outcome. Another drawback is the limitation of memory RAM to store a high resolution grid of the simulation model.

In order to present a direct comparison of the two methods, Figure 4 shows the frequency variation of spherical perturbers. The differences are clearly to observe on the maps. For instance, the FPM or Fourier method miscalculate the frequency variation at the borders of the sphere. This type of error does not appear on the continuous (analytical) space approximation and the resultant frequency map must be assumed as the ground truth.

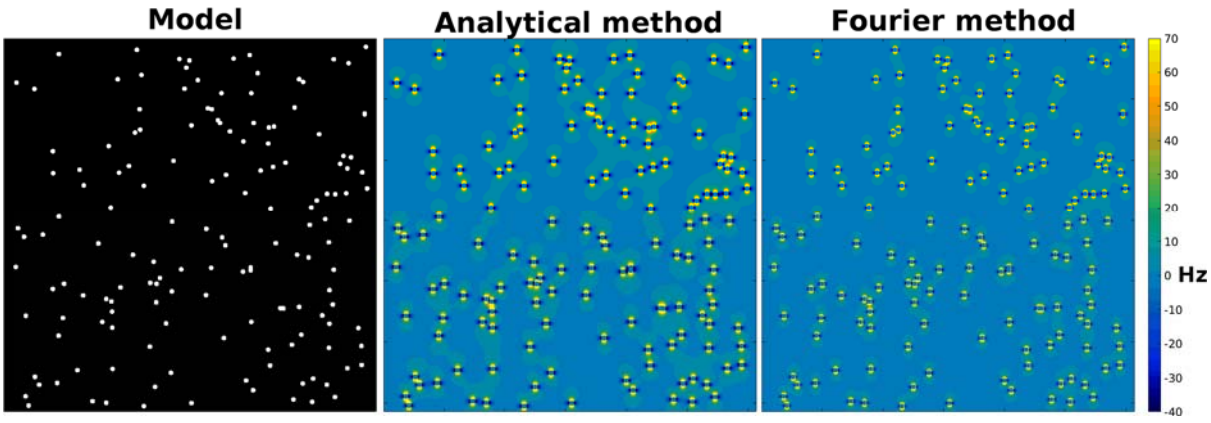

Figure 4. Depiction of a 2D random distributed spherical perturber model and the respective analytical and Fourier spatial inhomogeneous frequency map. Parameters: radius of 5 μm, 2% of volume fraction and susceptibility difference between spheres and the surrounding medium of 0.18 ppm. The similarities that these maps exhibit are remarkable, however, the Fourier method shows a disturbed frequency pattern in comparison to the analytical method. As consequence of this inaccuracy, at any given spatial point in the Fourier method an error factor must be assumed. On the other hand, the analytical calculation might be considered as the ground truth.

In Figure 5 and 6, the frequency line-shape produced by spherical perturbers with different radius are shown for both analytical and discrete spaces in a 2D and 3D model. It is possible to observe the already mentioned differences in the frequency map through the line-shape and the diverse density of the displayed frequencies dependent on the calculation method.

The MR signal can be calculated as the integral of several paths of random spins in motion or simply as the integral of the line-shape with the assumption of zero net diffusion. By this fact, the resultant MR signal shows different evolution behavior for both methods.

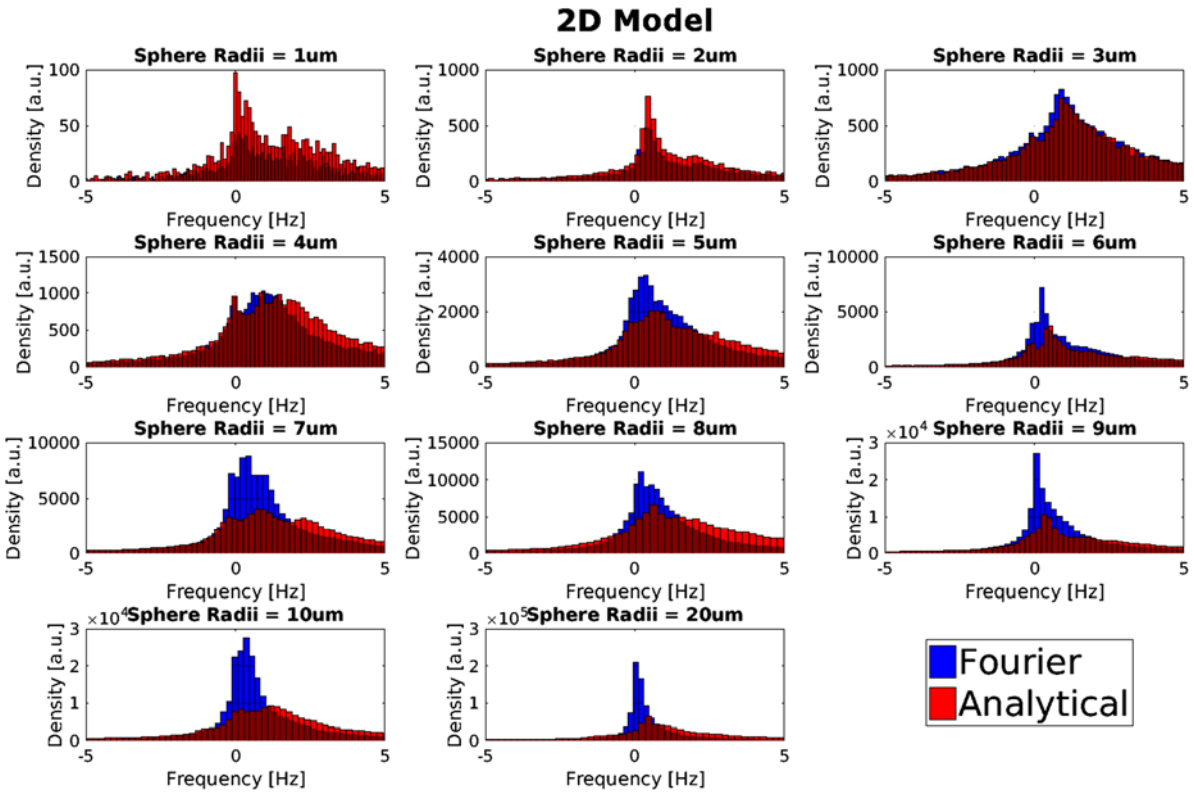

Figure 5. Histogram of the Larmor frequency distribution of a random distributed sphere model calculated by means of the Fourier and analytical approximation. The volume fraction is filled with 2% of spheres and a susceptibility difference exhibited between spheres and the surrounding medium is 0.18 ppm in a 2D space.

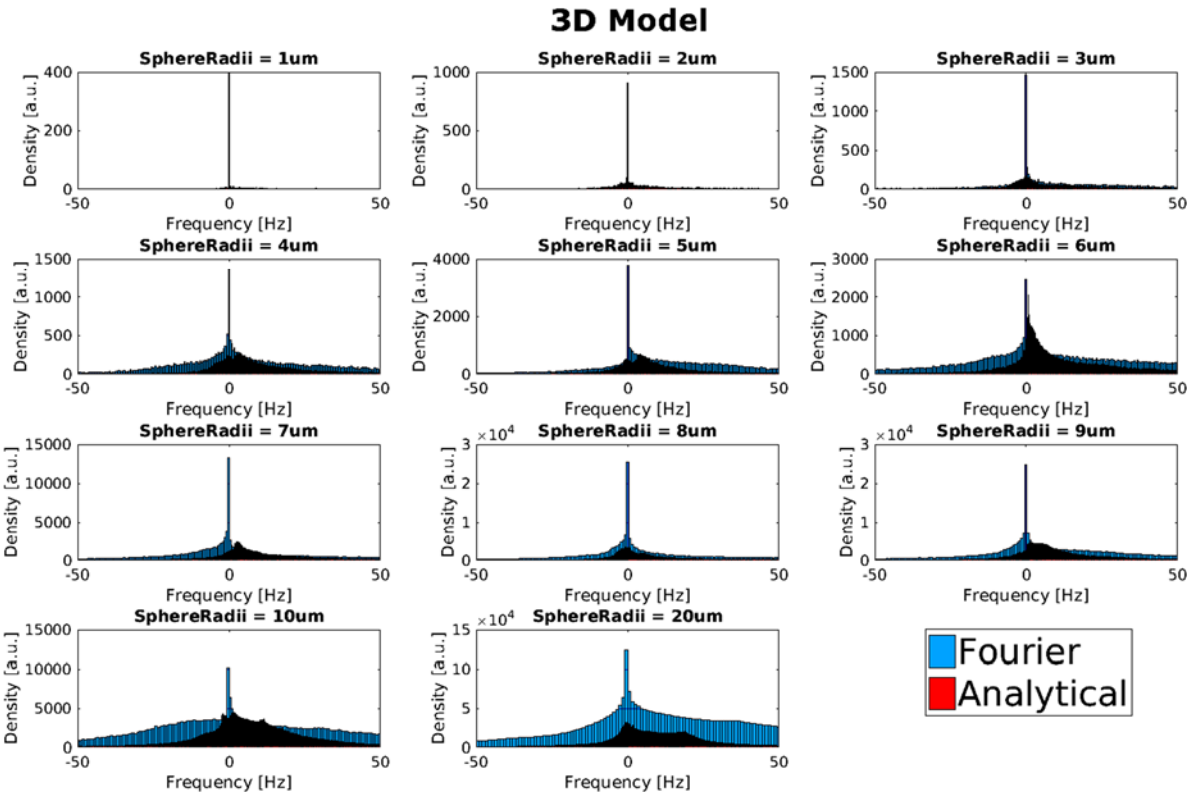

Figure 6. Histogram of the Larmor frequency distribution of a random distributed sphere model calculated by means of the Fourier and analytical approximation. The volume fraction is filled with 2% of spheres and the susceptibility difference exhibited between spheres and the surrounding medium is 0.18 ppm in a 3D space.

An important result in the characterization of MR signal formation was introduced by Boxerman and Weiskoff [Boxerman et al 1995, Weiskoff et al 1994]. In order to develop a reliable Monte Carlo algorithm, some well-established results were reproduced. The sensitivity of GE BOLD to large radius calibers of magnetic perturbers and the BOLD selectivity to small radius in a SE sequence are shown in Figure 7 and 8 for spherical and cylindrical geometrical perturbers.

Details of the performed simulations are described in the figure caption. Furthermore, these results demonstrate the correct MR signal approximation of the developed Monte Carlo algorithm in comparison to well-known analytical and numerical results.

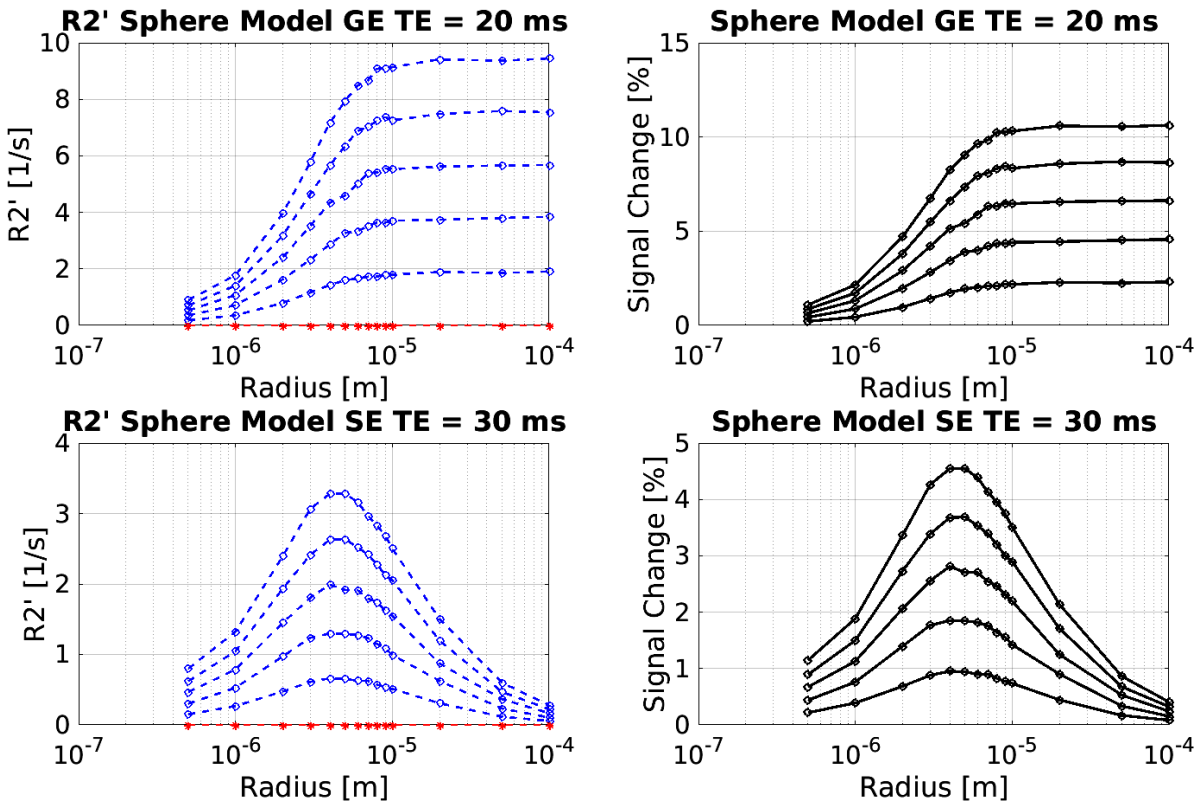

Figure 7. GE and SE relaxation calculated by susceptibility effects and diffusion motion for different sphere perturber sizes in a deoxygenated (80% of oxygen level, blue line) and an oxygenated (100% oxygen level, red line) state for different volume fractions (from 1% to 5%) at 9.4T. In addition, the BOLD signal changes (black lines) produced by uniform distributed spherical perturbers. The simulations were calculated in the continuous space. The used echo times are arbitrary.

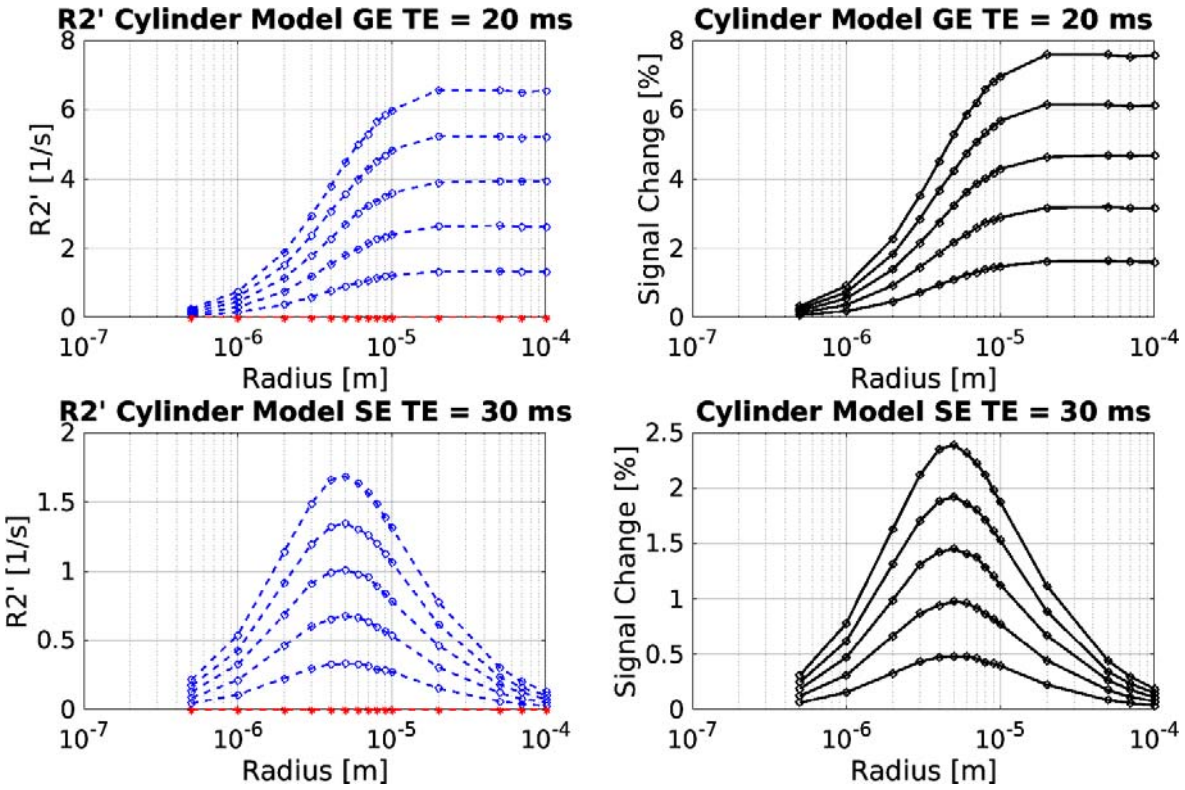

Figure 8. GE and SE relaxation calculated by susceptibility effects and diffusion motion for different cylinder perturber sizes in a deoxygenated (80% of oxygen level, blue line) and an oxygenated (100% oxygen level, red line) state for different volume fractions (from 1% to 5%) at 9.4T. In addition, the BOLD signal changes (black lines) produced by uniform distributed cylinder perturbers. The simulations were calculated in the continuous space. The used echo times are arbitrary.

For comparison, the properties of bSSFP has also been studied by means of Monte Carlo approximations and analytical methods [Kaiser et al 1974, Bieri et al 2007, Scheffler et al 2003, Ganter et al 2006, *Khajehim et al 2017*, Goa et al 2014, Dickson et al 2011, Malekian et al 2018, Dharmakumar et al 2005]. Figure 9 shows the obtained results given by the algorithm developed in this work in order to reproduce the well characterized behavior of bSSFP. Moreover, it is analyzed the impact of the magnetic field strength and the caliber selectivity due to the SE-like behavior of this sort of pulse sequence [Scheffler 2015].

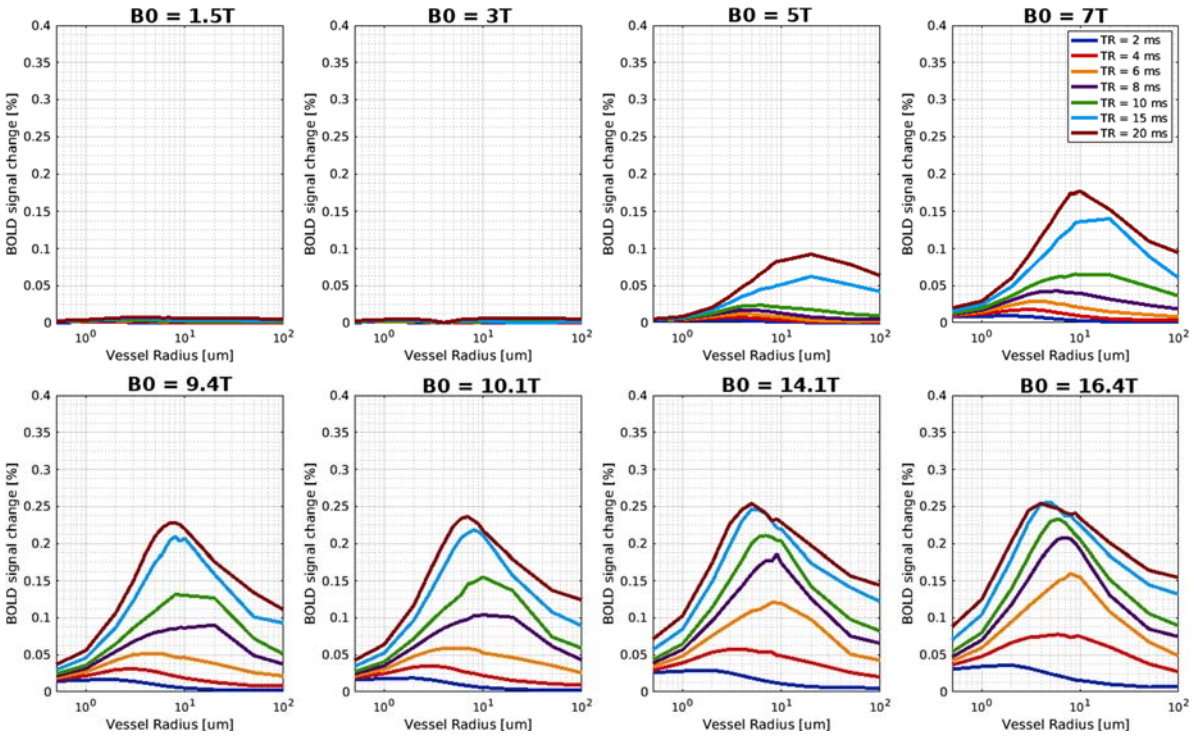

Figure 9. BOLD contrast selectivity exhibited by bSSFP obtained by a uniform distributed cylinder model in a deoxygenated (80% of oxygen level) and an oxygenated (100% oxygen level) state for different magnetic field strengths and different repetition times. The volume fraction was set to 2 %. It is worth to note the low sensitivity of the bSSFP to BOLD signal changes. Moreover, the impact of the repetition time is clearly visible. For larger repetition times, the SE-like behavior suffers an increasing contribution in the SDR. Besides, it is demonstrated the increased sensitivity to BOLD signal changes. This result suggests that the use of stronger magnetic fields, larger than 16.4 T, would improve the sensitivity of the bSSFP to BOLD signal changes [Scheffler 2015, Barth 2010].

Once that the impact of the perturber size (sphere or cylinder) and the volume fraction has been evaluated for a deoxygenated and oxygenated states, it is possible to combine all these responses into a conglomerate model as a direct comparison to a neurovascular network under certain assumptions.

For uniform distributed and oriented cylinders in the range from 0.5 µm to 100 µm in their radius, the BOLD signal change was studied at different magnetic field strengths and different echo times. The results are shown in Figure 10. Likewise, the

optimal echo time was obtained in order to maximize the BOLD contrast signal at different magnetic field strengths.

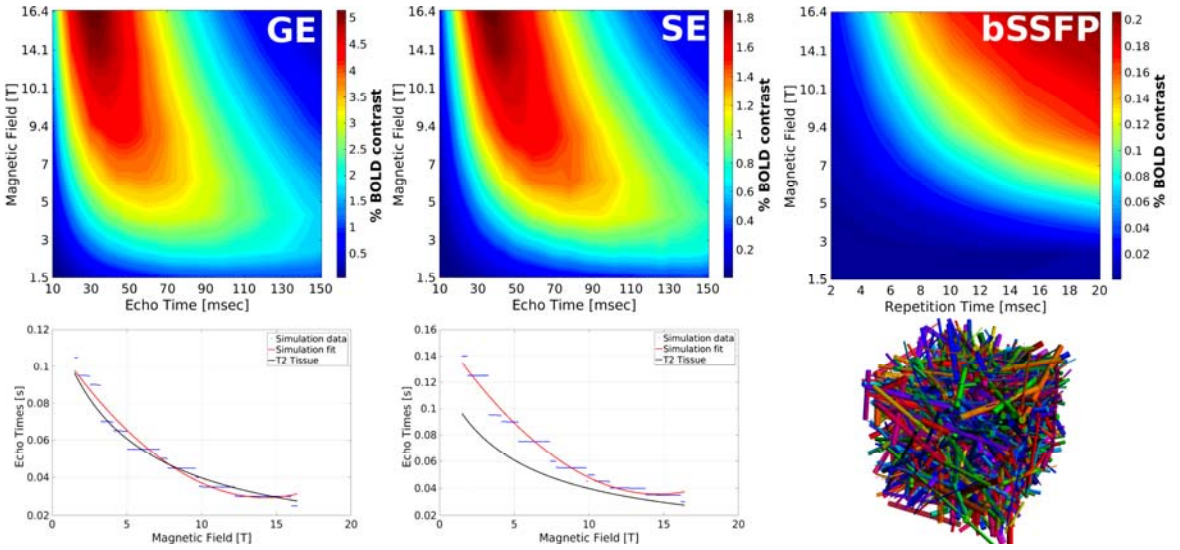

Figure 10. Simulation of BOLD contrast change at different magnetic field strengths and echo times. The simulation model and parameters comprise a random distributed and oriented cylinder model, oxygenation level between active and resting state were selected to be 100% and 80%, respectively. Diffusion coefficient of 1 $\mu m^2/ms$. The volume fraction was set to 2 %. It is clearly to observed the increased BOLD contrast exhibit at higher magnetic fields. The optimal echo time for GE acquisition can be calculated directly from the T2 value of the tissue. On the other hand, the SE sequence shows a modify behavior from the T2 of tissue. This increment depends on the magnetic field and it has a factor of approximately 1.2 of the T2 of tissue. The value of T2 of tissue were obtained by the polynomial expression given by [Khajehim et al 2017]. In addition, bSSFP shows an increased BOLD signal change for larger repetition times and higher magnetic fields.

3. Functional MR Signal Formation in a Realistic Neurovascular Network

The brain is the biggest energy-consumer organ in the human and non-human body. A so high energy-demand must be maintained by a robust and efficient energy delivery system [Chen et al 2013]. The neurovascular system accomplishes this particular task via the blood stream, been distributed by a complex vascular tissue network. Between 15% and 20% of the blood arrives to the brain throughout this system [Blinder et al 2013].

In this context, blood vessels of the cerebral cortex have been the object of numerous studies for more than a century [Duvernoy et al 1981 and references therein]. In sum, the neurovascular system is a complex network of micro tubes. Their principal duty is the proper delivery of oxygen and nutrients to the brain tissue. Moreover, it also performs the task of draining the metabolic residuals to keep the homeostasis of the brain. Therefore, the neurovascular system is very precise in the delivery of oxygenated blood when a neural activation is produced. This relation is known as the neurovascular coupling [Logothethis et al 2001].

In particular, changes in the neural activity are indeed followed by precisely controlled local changes in hemodynamics. In the recent years, this remarkable spatial and time specific neurovascular coupling has been systematically exploited by the use of PET and fMRI to generate detailed maps of the local hemodynamic changes that are triggered by a neural activation.

The spatial resolution and specificity of the functional maps rely not only on the cascade of neurovascular signaling, but also on the vascular architecture and spatial level of blood flow regulation [Fujita 2001]. In this sense, the quantification of the sensitivity and specificity of the pulse sequence to BOLD signal changes is an important characteristic to model, to improve the image acquisition and to disentangle the fundamental contributors of the MR signal evolution.

3.1. Neurovascular Network as Magnetic Perturber

New technologies have made possible, to study the three-dimensional vascular network topology of the neocortex in detail. In order to render the network in three dimensions, imaging methods are required to have a sufficient spatial resolution to resolve capillaries in a large field of view to cover the entire cortical depth. In addition, to estimate the diameter of capillaries, submicron spatial resolution is required.

David Kleinfeld and colleagues have developed the all-optical histology technique, whereby a two-photon microscopy is used to image the fluorescently labeled vasculature and a laser ablation is used to increase the field of view, which would normally be limited to a few hundred micrometers [Tsai et al 2003, Uludag et al 2018].

For technical details of the acquisition of this particular technique and a more complete histological and physiological description of the neurovasculature, the reader is referred to the publications of [Tsai et al 2003, Tsai et al 2009, Blinder et al 2013, Gould et al 2017, Weber et al 2008, Schmid 2017].

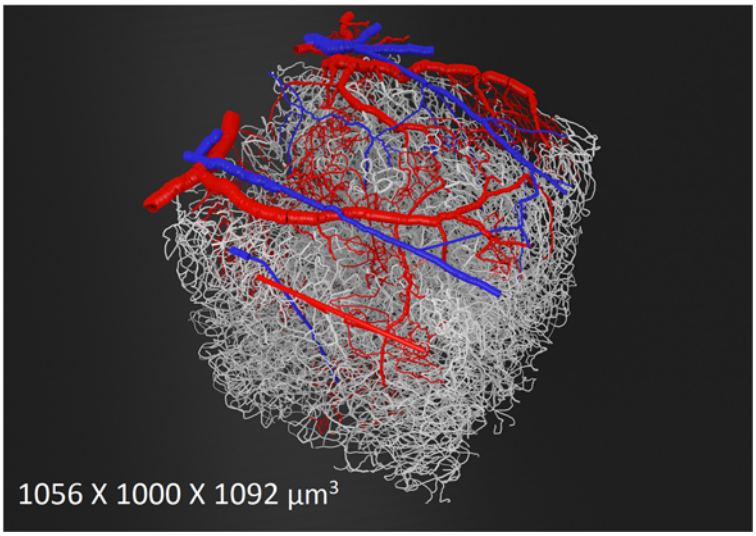

Figure 11. Neurovascular network obtained by means of two-photon imaging techniques from the parietal cortex of mice [Blinder el at 2013]. The spatial resolution of the model is 1 µm³. The model comprises arteries, veins and capillary bed acquired from the cortical surface to the white matter.

Moreover, Appendix 1 and 2 show a detailed description of the neurovascular features used in the Monte Carlo simulations in order to calculated the MR signal throughout this thesis [Baez et al 2017, Baez et al *in preparation*].

3.2. Results

Among the results obtained by the simulations in the neurovascular model described in Apprendix 1 and 2, this section complements those results with one important contribution.

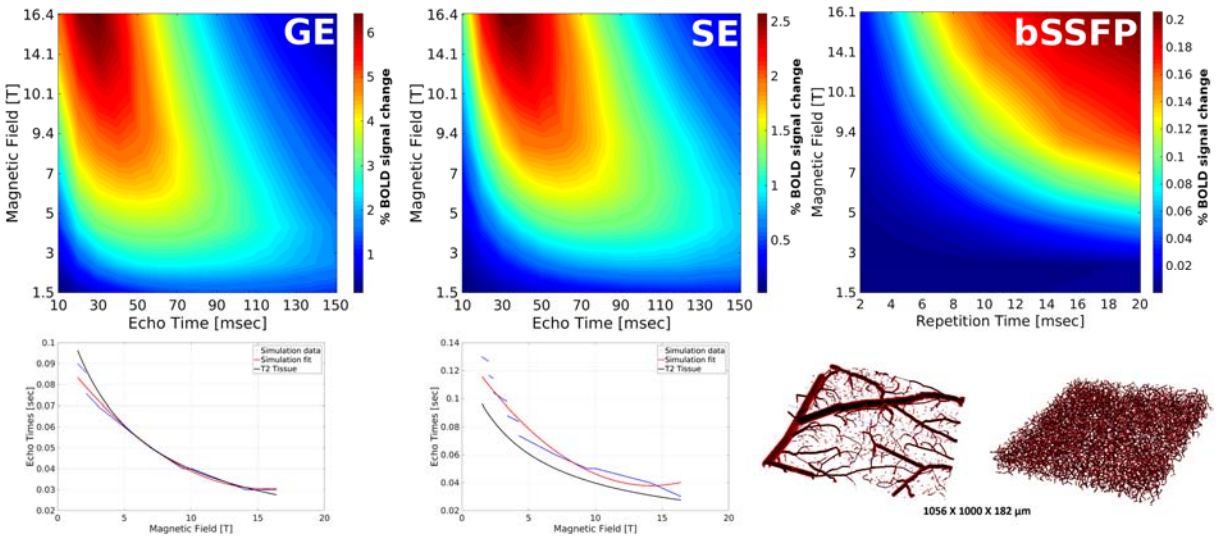

Figure 12. Simulated BOLD signal change produced by macro and micro vascular tissue. The simulation model and parameters comprise a realistic neurovascular network model, oxygenation level between active and resting state were selected to be 100% and 80% respectively. Diffusion coefficient of 1 µm²/ms. Similarly, in comparison to results obtained by random cylinders, it is clearly to observed the increased BOLD contrast displayed at higher magnetic fields. The optimal echo time for GE acquisition can be calculated directly from the T2 value of the tissue. On the other hand, the SE sequence shows a modify behavior from the T2 of tissue as already shown by the cylinder model. This increment depends on the magnetic field and it has a factor of approximately 1.3 larger than the T2 of tissue. The value of T2 of tissue were obtained by the polynomial expression given by [Khajehim et al 2017]. Moreover, bSSFP shows an increased BOLD signal change for larger repetition times and higher magnetic fields. It is worth to note the slightly larger values of the BOLD contrast in comparison to the results obtained by the random cylinder model.

Chapter II. List of papers and statement of contribution

(Darstellung des Eigenanteils bei Gemeinschaftsarbeiten nach §9 para. 2)

1. Paper I

Title: The impact of vessel size, orientation and intravascular contribution on the neurovascular fingerprint of BOLD bSSFP fMRI.

Authors: Mario Gilberto Báez-Yáñez, Philipp Ehses, Christian Mirkes, Philbert S. Tsai, David Kleinfeld, Klaus Scheffler.

Status of paper: Published in NeuroImage (see Baez et al, 2017). Available online at:
https://www.sciencedirect.com/science/article/pii/S1053811917307607?via%3Dihub since 8 September 2017.

Declaration of author contributions: MGBY and KS developed, independently, a Monte Carlo algorithm in order to reproduce well established results on infinitely long cylinder and sphere models. Moreover, to calculate the MR signal evolution in the neurovascular structure. PE programmed the image acquisition sequence. PE performed the image acquisition and fMRI analysis [Scheffler et al, 2015]. PTS and DK performed the two-photon laser scanning microscopy of the neurovascular tissue [Blinder et al 2013]. MGBY and CM performed the reconstruction of the neurovascular model to perform the Monte Carlo simulations in the discrete space. MGBY performed the calculation of the frequency maps by the use of the FPM method. KS performed the Monte Carlo simulations in order to obtain the BOLD signal changes. CM and KS produce the figures. The draft was written by KS. All authors provided critical feedback on the manuscript. KS supervised the research. MGBY and KS revised the manuscript according to the critique of anonymous expert reviewers.

Summary: In this publication, Monte Carlo simulations were implemented in order to calculate the attenuation signal induced by a static oxygenation level in artificial and neurovascular networks acquired from the mouse parietal cortex by two-photon laser scanning microscopy at 1 µm isotropic resolution for a GE, SE and pass-band bSSFP acquisition schemes. The impact of vessel size, blood volume and tissue orientation were analyzed. Moreover, the contribution of the intravascular signal at ultra-high magnetic fields and orientational dependence of the BOLD signal with respect to the magnetic field is described.

2. Paper II

Title: Disentangling the layer-specific BOLD signal change: a hemodynamic PSF simulation in a realistic neurovascular network.

Authors: Mario Gilberto Báez-Yáñez, Philbert S. Tsai, David Kleinfeld, Klaus Scheffler.

Status of paper: Manuscript in preparation for NeuroImage

Declaration of author contributions: PTS and DK performed the two-photon laser scanning microscopy of the neurovascular tissue [Blinder et al 2013]. MGBY designed the analytical analysis of the vascular model in the continuous space. MGBY performed the Monte Carlo simulations. MGBY produced the figures of the manuscript. The draft of the manuscript was written by MGBY. KS supervised the research and provided critical feedback on the draft.

Summary: The purpose of this work was to resolve the laminar-specific tissue contribution assuming a hemodynamic point spread function (PSF) in a realistic neurovascular network [Blinder et al 2013]. To achieve this goal, we investigated by means of Monte Carlo simulations the independent functional MR signal contribution of macrovessels (vessels larger than 5 μm in diameter) and microvessels (vessels smaller than 5 μm in diameter), assuming a hemodynamic response. Likewise, we analyzed the impact of pulse sequence parameters and the magnetic field strength.

First, we calculated the impact on the BOLD contrast for a homogeneous oxygenated (active) and deoxygenated (resting) state condition across the cortical depth for optimized BOLD parameters of a gradient echo (GE), spin echo (SE) and passband balanced steady-state free precession (bSSFP) pulse sequences at different magnetic field strengths (from 1.5 to 16.4 Tesla).

Second, in order to characterize the specificity of the neural activation, and thus the neurovascular blurring to the BOLD signal change towards to the cortical surface, we examined the hemodynamic PSF tissue response (macrovesels and microvessels independently) for optimized BOLD parameters of GE, SE and passband bSSFP sequences at 9.4 Tesla.

Overall our results demonstrate, that the BOLD signal is dependent on pulse sequence, acquisition parameters and magnetic field strength. In addition, the laminar-specific activation is blurred by tissue contribution originated by macrovessels, although their effect can possibly be reduced by pulse sequences that are selective to microvascular contributions such as SE and bSSFP.

3. Paper III

Title: The BOLD sensitivity of rapid steady state sequences

Authors: Klaus Scheffler, Rahel Heule, **Mario Gilberto Báez-Yáñez**, Bernd Kardatzki, Gabriele Lohmann.

Status of paper: Manuscript under review in MRM

Declaration of author contributions: KS and GL supervised the research. RH and MGBY performed the experimental acquisition. RH programmed the steady-state sequences to be used at the 3T scanner. MGBY and KS analyzed the experimental data. KS performed the Monte Carlo simulations. KS produced the figures of the manuscript. The draft of the manuscript was written by KS and BK. All authors revised the manuscript according to the critique of anonymous expert reviewers.

Summary: In this contribution we present an analysis of the BOLD sensitivity of non-balanced and balanced SSFP across field strength as a function of vessel size for several different coherence pathways, including the F^{+}_{0} “gradient echo”, the F^{-}_{0} “S2-echo”, the balanced echo, and higher order coherences. All calculations are based on Monte Carlo simulations of randomly oriented cylinders across different vessels diameters, repetition times, flip angles, and field strength. In addition, experimental measurements on dispersed microspheres of the F^{+}_{0} and F^{-}_{0} echo were performed to confirm the predicted dependence of these echo pathways on the radius of the measured spheres.

4. Other Contributions

- **Báez-Yáñez MG**, Scheffler K (June 2018): The angular dependence of the gradient echo and spin echo BOLD signal change induced by cortical capillaries and large vessels, 26th Annual Meeting and Exhibition of the International Society for Magnetic Resonance in Medicine (ISMRM 2018), Paris, France.

- Scheffler K, **Báez-Yáñez MG**, Lohman G (June 2018): The vascular fingerprint of non-balanced BOLD SSFP coherence pathways: gradient echos show spin echo behavior, 26th Annual Meeting and Exhibition of the International Society for Magnetic Resonance in Medicine (ISMRM 2018), Paris, France.

- **Báez-Yáñez MG**, Tsai PS, Kleinfeld D and Scheffler K (May 2018) Vascular point spread function in real cortical vessel networks. Laminar-specific fMRI Workshop, Magdeburg, Germany

- **Báez-Yáñez MG**, Tsai PS, Kleinfeld D and Scheffler K (November 2017) The impact of vessel size, orientation and intravascular contribution on the neurovascular fingerprint of BOLD bSSFP fMRI, 20. Jahrestagung der Deutschen Sektion der International Society for Magnetic Resonance in Medicine (ISMRM-DS 2017), 83-87.

- Ehses P, **Báez-Yáñez MG**, Erb M and Scheffler K (April 2017): Asymmetries of the balanced SSFP profile allow to probe microstructure anisotropy at 9.4 Tesla, 25th Annual Meeting and Exhibition of the International Society for Magnetic Resonance in Medicine (ISMRM 2017), Honolulu, HI, USA.

- **Báez-Yáñez MG**, Ehses P and Scheffler K (April 2017): The Impact of the Local, Mesoscopic Frequency Distribution and Diffusion in Gray and White Matter to the

Static bSSFP Signal Profile, 25th Annual Meeting and Exhibition of the International Society for Magnetic Resonance in Medicine (ISMRM 2017), Honolulu, HI, USA.

- Scheffler K, Kleinfeld D, Tsai P, **Báez-Yáñez MG** and Ehses P (April 2017): The neurovascular fingerprint of BOLD bSSFP: the impact of vessel size, orientation and intravascular contribution, 25th Annual Meeting and Exhibition of the International Society for Magnetic Resonance in Medicine (ISMRM 2017), Honolulu, HI, USA.

- **Báez-Yáñez MG**, Ehses P and Scheffler K (May 2016) Abstract Talk: The BOLD-sensitivity of balanced SSFP at very high fields is similar to GE-EPI but more selective to small vessels, 24th Annual Meeting and Exhibition of the International Society for Magnetic Resonance in Medicine (ISMRM 2016), Singapore

Chapter III. General Discussion and Conclusion

1. Synopsis

The MR signal is the result of complex biophysical interactions of spin magnetic moments depicting thermal motion within a susceptibility-induced inhomogeneous magnetic field [Buxton 2013, Chen et al 2013]. Additionally, the MR signal evolution is dependent on intrinsic tissue properties, pulse sequence parameters and the imposed magnetic field strength [Cheng et al 2001].

In order to approximate the fingerprint MR signal behavior of a particular mesoscopic model, analytical or numerical methods are employed to solve the Bloch-Torrey equation. The selection of the method (analytical or numerical approximation) depends on the characteristics of the problem and thus the presumed assumptions and boundary conditions that need to be resolved [Frohlich et al 2005, Jensen et al 2000, Jensen et al 2006].

In the particular problem analyzed in this thesis, Monte Carlo method is a well-established technique to simulate the Brownian motion of spins by the generation of random numbers with a specific frequency distribution such as a Gaussian or uniform distribution and therefore mimic the molecule displacement across a generic topological system. In addition, the implementation of intrinsic tissue properties and biophysical perturbations are straightforward employing this method in order to find the solution of equation (5) in a given coordinate system and the assumption of simplified geometrical shapes.

In this context, Monte Carlo method gives the opportunity to simulate MR interactions in the continuous- or discrete-space. Nevertheless, the continuous-space discrete-time depicts a bigger precision and accuracy on the resultant MR signal. On the contrary, the discrete-space discrete-time presents some drawbacks like a limited number of grid divisions of the model and a related error factor as already discussed in section 2.1.2.

As already mentioned before, a disadvantage of the Monte Carlo method is the long computational time employed in order to approximate the solution to a particular ensemble of perturbers and parameters [Mueller-Bierl et al 2007]. For example, the computational time required to approximate the calculation of the MR signal for a GE and SE pulse sequence and obtaining a significant result, can takes around a couple of hours (~8 hrs). On the other hand, a bSSFP simulation can run for some days or even for weeks. However, the computational time is strongly correlated to the biophysical features of the generic model and pulse sequence parameters.

In order to improve the performance of the calculation time, the first implemented Monte Carlo simulations throughout this work were approximated on a workstation CPU with 4 cores and an algorithm running in Matlab. This method employed long calculation time to approximate an outcome. Therefore, the Matlab code was improved and parallelized in a cluster CPU with 128 cores dedicated only for the Monte Carlo calculations. Besides the faster calculation shown by the cluster, the code was upgraded to C/C++ mex-files and thus gives the opportunity to speed up the calculations, whereas the main pipeline of the simulation remains on Matlab.

It is important to mention, that the Monte Carlo calculation might be accelerated with the use of novel and better suited numerical repositories and the use of graphics processing units (GPU's).

2. Functional MR signal simulation in a nonrealistic neurovascular model

The basic nature of the BOLD contrast is given by an induced dephasing of extravascular and intravascular spins depicting motion within a local inhomogeneous magnetic field produced by oxygenation changes in the blood vessels [Koopmans et al 2010]. However, this simple phrase cannot include all the hemodynamic transition and metabolic processes immerse on the BOLD effect. It is necessary to take all the vascular dynamics, blood oxygen, blood pressure and blood flow changes into

account, in order to approximate the real effect involved in a neural activation [Krieger et al 2012, Vazquez et al 2014, Boas et al 2008].

A limitation on my simulations were the absence of hemodynamic or volume fraction changes. These dynamic contributions might give a different result of the displayed BOLD signal changes. However, the static functional states give a general approximation of the BOLD contrast and signal evolution expected for different biophysical scenarios and pulse sequences.

The essence of the functional MR signal simulation studies is to solve numerically or analytically the Bloch-Torrey equation assuming specific biophysical and intrinsic tissue features in order to quantify the BOLD effect, optimize the pulse sequence parameter and improve the signal acquisition [Uludag et al 2009, Pflugfelder et al 2011].

In this context, the random distributed and oriented perturber model is well suited to characterize the response of the MR signal evolution for specific biophysical and pulse sequence parameters. Nevertheless, it is important to remember that the geometrical topology has a strong influence on the MR signal formation.

The biophysical variables, that disturb directly the MR signal evolution, can be characterized through the associated transversal relaxation modification R2', assuming a monoexponential decay. In this sense, the R2' modification given by GE, SE and bSSFP exhibits different signal evolutions, although they present some common behaviors. For instance, all sequences demonstrate a linear increment with respect to the blood volume fraction and the magnetic field strength [Baez et al 2017, Boxerman et al 1995, Figure 7, 8 and 9].

Moreover, as already shown by [Boxerman et al 1994], the GE shows a large sensitivity to all sort of radius of perturbers on the spherical and cylinder model. Additionally, the SE is more selective to small calibers from about 1μm to 20 μm [see Figure 7 and 8]. This selectivity of the SE depends on biophysical parameters such

as the intrinsic tissue characteristics, the diffusion coefficient, the imposed magnetic field strength and the level of oxygenation [Yablonskiy et al 2015].

Likewise, bSSFP in a random sphere or cylinder model demonstrates the same selectivity behavior like SE. However, this selectivity curve depends on, among the biophysical features, in the selected pulse sequence parameters like repetition time or flip angle excitation [Bieri et al 2006, Zielinski et al 2003]. Besides, note that the sensitivity of BOLD changes for bSSFP is smaller in contrast to GE and SE, but with a higher SNR and a reduced signal dropout [Scheffler et al 2015].

In particular, an advantage of image acquisition at ultra-high magnetic field, beyond the increased SNR and the high spatial resolution that can be achieved, is that the functional MR signal displays a linear increased gain for all sequences with respect to an increasing on the magnetic field strength [Petridou et al 2017, Yu et al 2014, Baez et al in preparation].

Further, the larger the magnetic field strength, the shorter the transversal relaxation time. This feature can be exploited at ultra-high magnetic fields in order to diminish the intravascular contribution to the BOLD signal change [Gardener et al 2010, Kennan et al 1994, Van derZwaag et al 2009]. Besides, the B_0 dependency shows a significantly increased contribution of the capillary bed at ultra-high fields [Yu et al 2012].

The random spatial distributed and oriented sphere or cylinder model gives, in general, a good approximation of the MR signal evolution, in order to study the pulse sequence parameters. For example, the echo times used for BOLD acquisition are selected to be approximated to the T2 value of the tissue. However, the obtained results suggest, that for SE this assumption is not correct and the selection of the echo time depends on a gross manner on biophysical and hemodynamic characteristics.

3. Functional MR signal simulation in a realistic neurovascular network

One of the most remarkable progress of this work is the use of a realistic neurovascular networks in order to calculate the BOLD contrast [Baez et al 2017, Gagnon et al 2015]. As demonstrated in several results throughout this thesis and in different seminal publications, the MR signal formation is sensitive to the geometrical shape of the mesoscopic structure, intrinsic magnetic properties and thermal motion.

The random cylinder model gives a good approximation of the overall contribution to the BOLD signal changes for specific biophysical parameters. However, in order to disentangle a particular tissue contribution of the functional MR signal, realistic neurovascular models must be used.

In this work, four neurovascular datasets are used in order to calculated the MR signal. To the best of my knowledge, the obtained datasets belong to the same region of the mice brain. Nevertheless, there are some evidently differences across the vascular structures and tissue characteristics. Owing to that, the BOLD signal change is dependent on the vascular architecture and the direct comparison of neural activity produced by different brain areas, such as the visual cortex or the motor cortex, might be carefully analyzed.

As mentioned before, one limitation on my simulations were the absence of hemodynamic or volume fraction changes. Simulation of hemodynamic changes in a real vasculature, assuming oxygenation, flow and pressure changes, is quite complicated to model. However, simplification of the functionality of the hemodynamic system might give a solution to tackle the problem [Boas et al 2008]. These dynamic contributions might give a different result of the displayed BOLD signal changes. However, the static functional states give a general approximation of the BOLD contrast and signal evolution expected for different biophysical scenarios and pulse sequences.

In Paper I, the impact of the radius on a random cylinder model is calculated for GE, SE and bSSFP. Besides, for the same sequences, the impact of a neurovascular geometry is analyzed. This paper contributes to the understanding of the BOLD signal formation, mainly, for the bSSFP sequence. This pulse sequence behavior was not studied on realistic vasculature topology before.

In the particular case of laminar-specific fMRI studies, hemodynamic vascular changes are not only specific to the neuronal activity across individual cortical layers, but also sensitive to changes in blood oxygenation that propagate across the cortex [Fracasso et al 2018, Baez et al in preparation].

In order to analyze this contribution to the laminar-specific BOLD signal change, the Paper II analyzes the contribution of large vessels and the blurring effect related to the diluted blood in the ascending veins. To the best of my knowledge, the only publication that models the point spread function on a neurovascular feature based model has been developed by [Markuerkiaga et al 2016]. On that publication, GE and SE were only analyzed. The analysis of the contribution from large vessels and oxygen diluted across the cortical depth was extended in the Paper II for the bSSFP, as well as GE and SE.

With the motivation to explore the BOLD signal response and the selectivity offered by the bSSFP, in Paper III the selectivity to microvascular contribution of the non-balanced SSFP was demonstrated for different magnetic field strengths and the impact of the selected pulse sequence parameters into the microvascular selectivity.

Besides the influence of the non-balanced gradient encoding system into the spin dephasing, the contribution of different spin pathways gives a SE-like behavior avoiding the band artifacts obtained in the balanced sequence. Moreover, dependent on the acquisition parameters, the ratio of micro/macro vascular contribution is similar to the SE BOLD pulse sequence, with reduced SAR constrains and a widely coverage of the brain.

4. Conclusion

Characterizing the dynamical process of mesoscopic structures, like vascular dilatation and temporal oxygenation levels, into measurable BOLD signal assuming a real neurovascular topology, is an important step towards to a physiological interpretation of neural activation maps and a general understanding of the neurovascular response in a BOLD fMRI experiment.

Modelling the BOLD signal over real vasculature data represents a significant improvement over the classical models based on infinitely cylindrical shapes in order to disentangle the functional and anatomical contribution to the MR fingerprint signal.

Therefore, modelling the MR signal opens the possibility to go beyond the actual spatial resolution, to quantify characteristics of the acquired signal, to improve the signal acquisition and temporal resolution and to optimize the pulse sequence parameters.

Acknowledgements

It has been a period of intense learning for me, not only in the scientific arena, but also on a personal level. The spatiotemporal events that took place during my PhD have had a huge impact on my life. Hence, I would like to reflect on the people who have supported and helped me so much throughout my scientific formation.

Foremost, I would like to express my sincere gratitude to my supervisor and mentor Prof. Dr. Klaus Scheffler. I am thankful for his continuous support of my PhD research, for his patience, motivation, enthusiasm and immense knowledge that he provided throughout this time. His observations and comments helped me to establish the overall direction of the research and to move forward with investigation in depth. Thank you Professor.

I want to thank my Advisory Board Members Dr. Xin Yu and Prof. Dr. Dieter Kölle for their time, fruitful discussions and guidance through my investigation. Besides, I want to thank Prof. Dr. Andreas Bartels to accept the invitation to be part of the committee and evaluate the thesis.

A very special gratitude goes out to the Consejo Nacional de Ciencia y Tecnología (CONACYT, México), who provided me with a scholarship and made possible my Master and Doctoral studies. Also, I am especially thankful to Tina Schröder, for the given support and all help provided on my arrival to Germany.

I am thankful to the Universidad Autónoma Metropolitana and their Professors for all the knowledge provided, to encouraged me to work in and for science, to taught me to use the critical thinking and to guided me to look for big challenges in science and life. Special mention goes to my former supervisors Prof. Dr. Gustavo Pacheco, Prof. Dr. Salvador Carrasco, Prof. Dr. Tomás Aljama and Prof. Dr. Salvador Cruz. I miss our interesting and long-lasting chats about any topic.

I want to thank Prof. Dr. Alfredo O. Rodriguez, Dr. Fabián Vázquez, Dr. Sergio Solis, Dr. Rodrigo “El Flaco” Martin and Dr. Oscar Marrufo, who have shown me the fascinating field of MRI and supported me to focus my PhD on this field.

I am also grateful to all my friends and colleagues that I met on my former University with special mention to: Andrés Hernández, Andrea García, Javier Reyes, Omar Piña, Jorge Luis and Eliseo Islas.

Completing this work would have been more difficult without the support and friendship provided by my friends and colleagues at the Max Planck Institute and in Tübingen. Especially, I want to thank Andre Antunes, Irena Zivkovic, Nevenka Cakić, Vladimir Cakić, José Arcadio, Diego García Corona, Juan F. Ramirez, Daniel Zaldivar, Marlon Pérez, Marco A. Flores, Carlos Valenzuela, David Izurrieta, Mihai Vintiloiu, Diego "El Loco" Sánchez and Filip Sobczak. To my dear office colleagues: Jens Hoffmann, Martin Eschelbach, Ali Aghaeifar and Alex Loktyushin and all my colleagues at the Institute. Thank you all for so much encouragement, good beer times, funny moments and your help and support at any time.

Further, I have an increasing debt with them for all their support, owing that, I am completely thankful to my parents D. Noemí Yáñez Anaya (D´Lors) and Pedro Báez Razo (Pedrito). Por todo lo que me han dado, por su apoyo incondicional, por todos sus consejos y por todo lo que me enseñaron. Les agradezco infinitamente. To my brothers Francisco Daniel y Mauricio, por todo su apoyo y por ser muy buenos hermanos, muchas gracias. I am also grateful to Sieglinde and Detlev Pitschak who have received me in their home, allowed me to take all food from their fridge and supported me all time.

Last but not least, I am especially grateful to Silke Pitschak, for all her love and for being extremely supportive of me throughout this entire process. She has made countless sacrifices to help me to get to this point. I want to thank for all her time, for all the delicious dishes prepared (particularly tacos al pastor), for all our *vancanciones* and so on, but mostly for being always here by my side. Thank you mi amor.

References

- Asslaender J, Glaser S, Henning J. Pseudo steady state free precession for MR-fingerprinting. Magn Reson Med (2017) 77:1151-1161
- Audoly B et al. Correlation functions for inhomogeneous magnetic field in random media with application to a dense random pack of spheres. J Magn Reson (2003) 154-159
- Báez-Yáñez MG et al, The impact of vessel size, orientation and intravascular contribution on the neurovascular fingerprint of BOLD bSSFP fMRI, NeuroImage (2017) 163:13-23
- Barth M et al. T2-weighted 3D fMRI using S2-SSFP at 7T. Magn Reson Med (2010) 63:1015-1020
- Barzykin A. Exact solution of the Bloch-Torrey equation for a spin echo in restricted geometries. Phys Rev B (1998) 58:14171-14174
- Bauer W et al. The relationship between the BOLD induced T2 and T2*: a theoretical approach for the vasculature of myocardium. Magn Reson Med (1999) 42:1004-1010
- Bauer W et al. Theory of the BOLD effect in the capillary region: an analytical approach for the determination of T2* in the capillary network of myocardium. Magn Reson Med (1999) 41:51-62
- Beaulieu C. The basis of anisotropic water diffusion in the nervous system-a technical review. NMR Biomed (2002) 15:435-455
- Belliveau J et al. Functional cerebral imaging by susceptibility contrast NMR. Magn Reson Med (1990) 14:538-546
- Benkert T et al. Dynamically phase-cycled radial balanced SSFP imaging for efficient banding removal. Magn Reson Med (2015) 73:182-194
- Bernstein M, King K, Zhou X. Handbook of MRI Pulse sequences. Elsevier (2004) 1st edition
- Bieri O Scheffler K. Effect of diffusion in inhomogeneous magnetic fields on balanced steady state free precession. NMR Biomed (2007) 20:1-10
- Bieri O, Ganter C, Scheffler K. Quantitative in vivo diffusion imaging of cartilage using double echo steady state free precession. Magn Reson Med (2012) 68:720-729
- Bieri O, Scheffler K. Fundamentals of balanced steady state free precession MRI. J Magn Reson Imaging (2013) 38:2-11
- Bieri O. An analytical description of balanced steady state free precession with finite radio-frequency excitation. Magn Reson Med (2011) 65:422-431

- Blinder P et al, The cortical angiome: an interconnected vascular network with noncolumnar patterns of blood flow. Nature Neurosci (2013) 16:889-897
- Bloch F. Nuclear Induction, Physical Review (1946) 1: 4604–73
- Blockley NP et al. Field strength dependence of R1 and R2*relaxivitiesof human whole blood to prohance, vasovist and deoxyhemoglobin. Magn Reson Med (2008) 60:1313-1320
- Boas D et al. A vascular anatomical network model of the spatio-temporal response to brain activation. NeuroImage (2008) 40:1116-1129
- Boxerman J et al. MR contrast due to intravascular magnetic susceptibility perturbations. Magn Reson Med (1995) 34:555-566
- Boxerman J et al. The intravascular contribution to fMRI signal change: Monte Carlo modeling and diffusion weighted studies in vivo. Magn Reson Med (1995) 34:4-10
- Brooks R et al. Comparison of T2 relaxation in blood, brain and ferritin. J Magn Reson (1995) 4:446-450
- Buschle L et al. Dephasing and diffusion on the alveolar surface. Phys Rev (2017) 95:022415
- Buschle L et al. Diffusion mediated dephasing in the dipole field around a single spherical magnetic object. Magn Reson Med (2015) 33:1126-1145
- Buxton R et al. Signal intensity in fast NMR imaging with short repetition times. J Magn Reson (1989) 83:576-585
- Buxton R. The physics of functional magnetic resonance imaging (fMRI). Rep Prog Phys (2013) 76:1-30
- Callaghan P. A simple matrix formalism for spin echo analysis of restricted diffusion under generalized gradient waveforms. J Magn Reson (1997) 129:74-84
- Carr HY. Steady state free precession in nuclear magnetic resonance. Phys Rev (1958) 112:5
- Chen et al. Layer-specific BOLD activation in awake monkey V1 revealed by ultra-high spatial resolution functional magnetic resonance imaging. Neuroimage (2013) 64:147-155
- Chen W, Foxley S, Miller K. Detecting microstructural properties of white matter based on compartmentalization of magnetic susceptibility. NeuroImage (2013) 70:1-9
- Cheng Y, Haacke M, Yu Y. An exact form for the magnetic field density of states for a dipole. Magn Reson Ima (2001) 19:1017-1023
- Concha L. A macroscopic view of microstructure: using diffusion weighted images to infer damage, repair, and plasticity of white matter. Neurosci (2014) 276:14-28

- Dharmakumar R et al. Oxygen sensitive contrast in blood for steady state free precession imaging. Magn Reson Med (2005) 53:574-583
- Dharmakumar R, Wright G. Understanding steady state free precession: a geometric perspective. Concep Magn Reson Part A (2005) 26:1-10
- Dickson J et al. Quantitative phenomenological model of the BOLD contrast mechanism. J Magn Reson (2011) 212:17-25
- Dortch R et al. Characterizing inter-compartmental water exchange in myelinated tissue using relaxation exchange spectroscopy. Magn Reson Med (2013) 70:1450-1459
- Durrant C, Hertzberg M, Kuchel P. Magnetic susceptibility: Further insights into macroscopic and microscopic fields and the sphere of Lorentz. Concep Magn Reson (2003) 18:72-95
- Duvernoy HM et al. Cortical blood vessels of the human brain. Brain Res Bull (1981) 7:519-579
- Duyn J, Schenck J. Contributions to magnetic susceptibility of brain tissue. NMR Biomed (2017) 30:1-37
- Duyn J. MR susceptibility imaging. J Magn Reson (2013) 229:198-207
- Einstein, A. Über die von der molecularkinetischen Theorie der Wärme geforderte Bewegung von in ruhenden Flüssigkeiten suspendierten Teilchen. Ann. Phys. (1905) 17: 549–569
- Elst L et al. Dy-DTPA derivatives as relaxation agents for very high field MRI: The beneficial effect of slow water exchange on the transverse relaxivities. Magn Reson Med (2002) 47:1121-1130
- Fisel R et al. MR contrast due to microscopically heterogeneous magnetic susceptibility: numerical simulations and applications to cerebral physiology. Magn Reson Med (1991) 17:336-347
- Fracasso A et al, Laminar imaging of positive and negative BOLD in human visual cortex at 7T, Neuroimage (2018) 164: 100-111
- Freed D et al. Steady state free precession experiments and exact treatment of diffusion in a uniform gradient. J Chem Phys (2001) 115:4249-4258
- Frohlich A et al. Theory of susceptibility induced transverse relaxation in the capillary network in the diffusion narrowing regime. Magn Reson Med (2005) 53:564-573
- Fujita N. Extravascular contribution of blood oxygenation level dependent signal changes: a numerical analysis based on a vascular network model. Magn Reson Med (2001) 46:723-734
- Gagnon L. et al, Quantifying the microvascular origin of BOLD fMRI from first principles with two-photon microscopy and an oxygen-sensitive nanoprobe, J Neurosci (2015) 35:3663-3675

- Ganter C. Static susceptibility effects in balanced SSFP sequences. Magn Reson Med (2006) 56:687-691
- Ganter C. Steady state of gradient echo sequences with radiofrequency phase cycling: analytical solution, contrast enhancement with particular spoiling. Magn Reson Med (2006) 55:98-107
- Gardener A et al. Dependence of blood R2 relaxivity on CPMG echo-spacing at 2.35 and 7T. Magn Reson Med (2010) 64:967-974
- Glasser M, Van Essen D. Mapping human cortical areas in vivo based on myelin content as revealed by T1- and T2- weighted MRI. J Neurosc (2011) 31:11597-11616
- Goa P et al. BOLD fMRI signal characteristics of S1- and S2- SSFP at 7 Tesla. Front in Neurosc (2014) 49:1-6
- Goense J et al. fMRI at high spatial resolution: implications for BOLD models. Front Comput Neurosci (2016) 10:66
- Goense J, Logothetis N. Laminar specificity in monkey V1 using high resolution SE-fMRI. Magn Reson Ima (2006) 24:381-392
- Gould IG et al. The capillary bed offers the largest hemodynamic resistance to the cortical blood supply. J Cereb Blood F&Met (2017) 37:52-68
- Grebenkov DS. NMR survey of reflected Brownian motion. Rev Moder Phys (2007) 69:1077-1137
- Grgac K et al. Hematocrit and oxygenation dependence of blood 1H2o T1 at 7T. Magn Reson Med (2013) 70:1153-1159
- Guyton and Hall. Textbook of medical physiology. Elsevier (2015) 13th edition
- Haacke M et al. Susceptibility weighted imaging: technical aspects and clinical applications, part I. Phys Rev (2009) 30:19-30
- Haacke, E M. Magnetic Resonance Imaging: Physical Principles and Sequence Design. New York: Wiley (1999)
- Haenicke W, Vogel H. An analytical solution for the SSFP signal in MRI. Magn Reson Med (2003) 49:771-775
- Hahn E. Spin echoes. Phys Rev (1950) 80:580-594
- Hall M, Alexander D. Convergence and Parameter choice for Monte Carlo simulations of diffusion MRI. IEEE Trans Med Ima (2009) 28:1354-1364
- Hall M. Continuity, the Bloch Torrey equation and diffusion MRI. Med Phys (2016) arXiv:1608.02859
- Hargreaves B et al. Characterization and reduction of the transient response in steady state MR imaging. Magn Reson Med (2001) 46:149-158
- He X, Yablonskiy A. Biophysical mechanisms of phase contrast in gradient echo MRI. PNAS (2009) 106:13558-13563
- Huber L et al. Cortical lamina-dependent blood volume changes in human brain at 7T. NeuroImage (2015) 107:23-33

- Jackson, John D. Classical Electrodynamics (3rd ed.). New York: John Wiley & Sons (1999)
- Jain V et al. Investigating the magnetic susceptibility properties of fresh human blood for noninvasive oxygen saturation quantification. Magn Reson Med (2012) 68:863-867
- Jenkinson M, Wilson J, Jezzard P. Perturbation method for magnetic field calculations of nonconductive object. Magn Reson Med (2004) 52:471-477
- Jensen J et al. Magnetic field correlation imaging. Magn Reson Med (2006) 55:1350-1361
- Jensen J, Chandra R. NMR relaxation in tissue with weak magnetic inhomogeneities. Magn Reson Med (2000) 44:144-156
- Kaiser R et al. Diffusion and field gradient effects in NMR Fourier spectroscopy. J Chem Phys (1974) 60:2966-2978
- Kalantari S et al. Insight into in vivo magnetization exchange in human white matter regions. Magn Reson Med (2011) 66:1142-1151
- Karch et al. A Gibbs point field model for the spatial pattern of coronary capillaries. Physica A (2006) 369, 599-611.
- Keller AL et al. Vascularization of cytochrome oxidase rich blobs in the primary visual cortex of squirrel and macaque monkeys. J Neurosci (2011) 31:1246-1253
- Kenkre V et al. Simple solutions of the Bloch-Torrey equations in the NMR study of molecular diffusion. J Magn Reson (1997) 128:62-69
- Kennan R, Zhong J, Gore J. Intravascular susceptibility contrast mechanisms in tissues. Magn Reson Med (1994) 31:9-21
- Khajehim et al. Investigating the spatial specificity of S2-SSFP fMRI: A Monte Carlo simulation approach. Magn Reson Im (2017) 37:282-289
- Kim SG, Ogawa S. Biophysical and physiological origins of blood oxygenation level dependent fMRI signals. J Cereb Blo Flo Met (2012) 32:1188-1206
- Kim TS et al. Analysis of the BOLD characteristics in pass-band bSSPF fMRI. Int J Imaging Syst Technol (2012) 22:23-32
- Kiselev V, Novikov D. Transverse NMR relaxation as a probe of mesoscopic structure. Phys Rev Lett (2002) 89:1-4
- Kiselev V, Posse S. Analytical theory of susceptibility induced NMR signal dephasing in a cerebrovascular network. Phys Rev (1998) 81:5696-5699
- Kiselev V. On the theoretical basis of perfusion measurements by dynamic susceptibility contrast MRI. Magn Reson Med (2001) 46:1113-1122
- Kiselev V. Posse S. Analytical model of susceptibility induced MR signal dephasing: effect of diffusion in a microvascular network. Magn Reson Med (1999) 41:499-509

- Kjolby B, Ostergaard L, Kiselev V. Theoretical model of intravascular paramagnetic tracer effect on tissue relaxation. Magn Reson Med (2006) 56:187-197
- Kleinnijenhuis M et al. Layer-specific diffusion weighted imaging in human primary visual cortex in vitro. Cortex (2013) 49:2569-2582
- Koch K et al. Rapid calculations of susceptibility-induced magnetostatic field perturbations for in vivo magnetic resonance. Phys Med (2006) 51:6381-6402
- Koopmans P, Barth M, Norris D. Layer-specific BOLD activation in human V1. Hum Bra Map (2010) 31:1297-1304
- Krieger S et al. Cerebral blood volume changes during brain activation. J Cereb Bl Fl Metab (2012) 32:1618-1631
- Krishnamurthy L et al. Dependence of blood T2 on oxygenation at 7T: in vivo calibration and in vivo application. Magn Reson Med (2014) 71:2035-2042
- Kurz F et al. CPMG relaxation rate dispersion in dipole fields around capillaries. Magn Reson Ima (2016) 34:875-888
- Kurz F et al. Generalized moment analysis of magnetic field correlations for accumulationsof spherical and cylindrical magnetic perturbers. Front Phys (2016) 4:1-16
- Kurz F et al. Microstructural analysis of peripheral lung tissue through CPMG inter-echo time R2 dispersion. PlosOne (2015) 10:1-22
- Kurz F et al. Spin dephasing in a magnetic dipole field around large capillaries: Approximative and exact results. J Magn Reson (2016) 273:83-97
- Kurz F et al. Theoretical model of the single spin-echo relaxation time for spherical magnetic perturbers. Magn Reson Med (2014) 71:1888-1895
- Kurz FT et al. The influence of spatial patterns of capillary networks on transverse relaxation. Magn Reson Img (2017) 40:31-47
- L Bihan D. Diffusion, confusion and functional MRI. NeuroImage (2012) 62:1131-1136
- Landman B et al. Complex geometric models of diffusion and relaxation in healthy and damaged white matter. NMR Biomed (2009) 23:152-162
- Lauwers F et al. Morphometry of the human cerebral cortex microcirculation: general characteristics and space related profiles. NeuroImage (2008) 39:936-948
- Le Bihan D. Diffusion MRI: what water tell us about the brain. EMBO Molec Med (2014) 6:569573
- Le Bihan D. The wet mind: water and functional neuroimaging. Phys Med Biol (2007) 52:1-13
- Lee J et al. Mechanisms of T2* anisotropy and gradient echo myelin water imaging. NMR Biomed (2016) 30:1-13

- Lee J et al. Sensitivity of MRI resonance frequency to the orientation of brain tissue microstructure, PNAS (2010) 107: 5130-5135
- Lee J et al. T2* based fiber orientation mapping. NeuroImage (2011) 57:225-234
- Lee JH et al. Full brain coverage and high resolution imaging capabilities of passband bSSFP fMRI at 3T. Magn Reson Med (2008) 59:1099-1110
- Lee SP et al. Diffusion weighted spin echo fMRI at 9.4T: microvascular/tissue contribution to BOLD signal changes. Magn Reson Med (1999) 42:919-928
- Leupold J, Hennig J, Scheffler K. Alternating repetition time balanced steady state free precession. Magn Reson Med (2006) 55:557-565
- Levitt M. Spin Dynamics: Basics of Nuclear Magnetic Resonance. Wiley (2001). 2nd edition
- Li L, Leigh J. Quantifying arbitrary magnetic susceptibility distributions with MR. Magn Reson Med (2004) 51:1077-1082
- Liu C. Susceptibility tensor imaging. Magn Reson Med (2010) 63:1471-1477
- Logothetis N et al. Neurophysiological investigation of the basis of the fMRI signal. Nature (2001) 412:150-157
- Luo J et al. Protein-induced water 1H MR frequency shifts: contributions from magnetic susceptibility and exchange. J Magn Reson (2010) 202:1-15
- Luo J, He X, Yablonskiy A. Magnetic susceptibility induced white matter MR dignal frequency shifts-experimental comparison between Lorentzian sphere and Generalized Lorentzian approaches. Magn Reson Med (2014) 71:1251-1263
- Lyons D et al. Mapping oxygen concentration in the awake mouse brain. eLife (2016) 5:1-16
- Ma D et al, Magnetic resonance fingerprinting, Nature (2013) 495:187-192
- Malekian et al. A robust SSFP technique for fMRI at ultra-high field strengths. Magn Reson Med (2018) 50:17-25
- Malekian V et al. A robust SSFP technique for fMRI at ultra-high field strengths. Magn Reson Imag (2018) 50:17-25
- Markuerkiaga I et al. A cortical vascular model for examining the specificity of the laminar BOLD signal. NeuroImage (2016) 132:491-498
- Marques J, Bowtell R. Aplication of a Fourier based method for rapid calculation of field inhomogeneity due to spatial variation of magnetic susceptibility. Conc Magn Reson Part B (2004) 25:65-78
- Marques J, Bowtell R. Using forward calculations of the magnetic field perturbation due to a realistic vascular model to explore the BOLD effect. NMR Biomed (2008) 21:553-565

- Miller K, Jezzard P. Modeling SSFP functional MRI contrast in the brain. Magn Reson Med (2008) 60:661-673
- Miller K. Asymmetries of the balanced SSFP profile. Part I: theory and observation. Magn Reson Med (2010) 63:385-395
- Miller K. Asymmetries of the balanced SSFP profile. Part II: white matter. Magn Reson Med (2010) 63:396-406
- Miller K. FMRI using balanced steady state free precession. NeuroImage (2012) 713-719
- Miller KL. Signal and noise characteristic of SSFP fMRI: a comparison with GRE at multiple field strengths. NeuroImage (2007) 37:1227-1236
- Mueller Bierl B et al. Magnetic field distribution and signal decay in functional MRI in very high fields (up to 9.4T) using Monte Carlo diffusion modeling. Int J Biomed Ima (2007) 10:1-7
- Mueller-Bierl B et al, Compensation of magnetic field distortions from paramagnetic instruments by added diamagnetic material: measurements and numerical simulations. Med Phys (2004) 32:76-84
- Murase K et al. Numerical solutions to the time dependent Bloch equations revised. Magn Reson Med (2011) 29:126-131
- Ogawa S et al. Functional brain mapping by blood oxygenation level dependent contrast magnetic resonance imaging: a comparison of signal characteristics with a biophysical model. J Biophys (1993) 64:803-812
- Panagiotaki E et al. Compartment models of the diffusion MR signal in the brain white matter: a taxonomy and comparison. NeuroImage (2012) 59:2241-2254
- Pannetier N et al. Numerical modeling of susceptibility related MR signal dephasing with vessel size measurement: phantom validation at 3T. Magn Reson Med (2014) 72:646-658
- Park SH et al. Sensitivity and specificity of high resolution balanced steady state free precession fMRI at high field of 9.4T. NeuroImage (2011) 58:168-176
- Pathak A. et al. A novel technique for modeling susceptibility based contrast mechanism for arbitrary microvascular geometries: the finite perturber method. NeuroImage (2008) 40:1130-1143
- Patil S, Bieri O, Scheffler K. Echo dephased steady state free precession. Magn Reson Mater Phy (2009) 22:277-285
- Petridou N, Siero J. Laminar fMRI: what can the time domain tell us?. NeuroImage (2017) 164:100-111
- Pflugfelder D et al. On the numerically predicted spatial BOLD fMRI specificity for spin echo sequences. Magn Reson Med (2011) 29:1195-1204

- Puckett AM et al. The spatiotemporal hemodynamic response function for depth-dependent functional imaging of human cortex. NeuroImage (2016) 139:240-248
- Reichenbach J. The future of susceptibility contrast for assessment of anatomy and function. NeuroImage (2012) 62:1311-1315
- Reichold J et al. Vascular graph model to simulate the cerebral blood flow in realistic vascular networks. J Cer Blo Flo Met (2009) 29:1429-1443
- Reisert M et al. Disentangling micro from mesostructure by diffusion MRI: a Bayesian approach. NeuroImage (2017) 147:964-975
- Rhodes R. The making of the atomic bomb. Simon & Schuster (1986)
- Rozenman Y et al. Signal loss by superparamagnetic iron oxide particles in NMR spin echo images: the role of diffusion. Magn Reson Med (1990) 14:31-39
- Rozenman Y et al. Signal loss induced by superparamagnetic iron oxide particles in NMR spin-echo images: the role of diffusion. Magn Reson Med (1990) 14:31-39
- Ruh A, Scherer H, Kiselev V. The Larmor freuqnecy shift in magnetically heterogeneous media depends on their mesoscopic structure. Mag Reson Med (2018) 79:1101-1110
- Scheffler K et al. Detection of BOLD changes by means of a frequency sensitive trueFISP technique: preliminary results. NMR Biomed (2001) 14:490-496
- Scheffler K, Ehses P. High-resolution mapping of neuronal activation with balanced SSFP at 9.4 Tesla. Magn Reson Med (2015) 76:1522-2594
- Scheffler K, Henning J. Is TrueFISP a Gradient-Echo or a Spin-Echo Sequence? Magn Reson Med (2003) 49:395-397
- Scheffler K, Lehnhardt S. Principles and applications of balanced SSFP techniques. Eur Radiol (2003) 13:2409-2418
- Scheffler K. A pictorical description of steady-state in rapid magnetic resonance imaging. Conc. Magn Reson (1999) 11: 291-304
- Scheffler K. On the transient phase of balanced SSFP sequences. Magn Reson Ima (2003) 49:781-783
- Schmid F et al, Depth-dependent flow and pressure characteristics in cortical microvascular networks. PloS Comput Biol (2017) 13:1-22
- Schmid F et al. Vascular density and distribution in neocortex. NeuroImage (2017) in press
- Semmineh N et al. An efficient computational approach to characterize DSC-MRI signals arising from three dimensional heterogeneous tissue structures. PlosOne (2014) 9:1-13

- Sen P. Time dependent diffusion coefficient as a probe of geometry. Conc Magn Reson Part A (2004) 23:1-21
- Seppenwoolde J et al. Spectral characterization of local magnetic field inhomogeneities. Phys Med Bio (2005) 50:361-372
- Shmuel A et al. Spatio-temporal point spread function of fMRI signal in human gray matter at 7 Tesla. NeuroImage (2007) 35:539-552
- Shmueli K et al. The contribution of chemical exchange to MRI frequency shifts in brain tissue. Magn Reson Med (2011) 65:35-43
- Speck O, Scheffler K, Henning J. Fast 31P chemical shift imaging using ssfp methods. Magn Reson Med (2002) 48:633-639
- Stanisz G et al. Water dynamics in human blood via combined measurement of T2 relaxation and diffusion in the presence of gadolinium. Magn Reson Med (1998) 39:223-233
- Stejskal E, Tanner J. Spin diffusion measurements: spin echoes in the presence of a time dependent field gradient. J Chem Phys (1965) 42:1
- Sukstanskii A, Yablonskiy D. Effects of restricted diffusion on MR signal formation. J Magn Reson (2002) 157:92-105
- Sukstanskii A, Yablonskiy D. Gaussian approximation in the theory of MR signal formation in the presence of structure-specific magnetic field inhomogeneities. J Magn Reson (2003) 163:236-247
- Sukstanskii A, Yablonskiy D. Theory of FID NRM signal dephasing induced by mesoscopic magnetic field inhomogeneities in biological systems. J Magn Reson (2001) 151:107-117
- Sun H et al. Steady state functional MRI using spoiled small tip fast recovery imaging. Magn Reson Med (2015) 73:536-543
- Torrey HC. Bloch Equations with Diffusion Terms. Phys. Rev. (1956) 104, 563
- Tsai P et al. All-optical histology using iltrashort laser pulses. Neuron (2003) 39:27-41
- Tsai PS et al. Correlations of neuronal and microvascular densities in murine cortex revealed by direct counting and colocalization of nuclei and vessels. J Neuroscie (2009) 29:14553-14570
- Uludag K, Blinder P. Linking brain vascular physiology to hemodynamic response in ultra-high field MRI. NeuroImage (2018) 168:279:295
- Uludag K, Mueller-Bierl B, Ugurbil K. An integrative model for neuronal activity-induced signal changes for gradient and spin echo functional imaging. NeuroImage (2009) 48:150-165
- Van der Zwaag W et al. FMRI at 1.5, 3 and 7T: characterizing BOLD signal changes. NeuroImage (2009) 47:1425-1434

- Vazquez AL et al. Neural and hemodynamic responses elicited by forelimb and photostimulation in channelrhodopsin-2 mice: insights into the hemodynamic point spread function. Cer Cor (2014) 24:2908-2919
- Vuong Q, Gillis P, Gossuin Y. Monte Carlo simulation and theory of proton NMR transverse relaxation induced by aggregation of magnetic particles used as MRI contrast agents. J Magn Reson (2011) 212:139-148
- Weber B et al. The microvascular system of the striate and extricate visual cortex of the macaque. Cereb Cortex (2008) 10:1093
- Weisskoff R. The characterization of dynamic susceptibility effects. NeuroImage (2012) 1014-1016
- Weisskoff RM et al. Microscopic susceptibility variation and transverse relaxation: theory and experiment. Magn Reson Med (1994) 31:601-610
- Wells J et al. Measuring biexponential tranverse relaxation of the ASL signal at 9.4T to estimate arterial oxygen saturation and the time of exchange of labeled blood water into cortical brain tissue. J Cereb Blo Flo Met (2013) 33:215-224
- Wharton S, Bowtell R. Effects of white matter microstructure on phase and susceptibility maps. Magn Reson Med (2015) 73:1258-1269
- Woessner D. Effects of diffusion in nuclear magnetic resonance spin echo experiments. J Chem Phys (1961) 34:6
- Yablonskiy D, Haacke M. Theory of NMR signal behavior in magnetically inhomogeneous tissues: the static dephasing regime. Magn Reson Med (1994) 32:1522-2594
- Yablonskiy D, Sukstanskii A, He X. Blood oxygenation level dependent based thechinques for the quatification of brain hemodynamic and metabolic properties, theoretical models and experimental approaches. NMR Biomed (2012) 26:963-986
- Yablonskiy D, Sukstanskii A. Generalized Lorentzian tensor approach (GLTA) as a biophysical background for quantitative susceptibility mapping. MAgn Reson Med (2015) 73:757-764
- Yablonskiy D, Sukstanskii A. Theoretical models of the diffusion weighted MR signal. NMR Biomed (2010) 23:661-681
- Ye F, Allen P. Relaxation enhancement of the transverse magnetization of water protons in paramagnetic suspensions of red blood cells. Magn Reson Med (1995) 34:713-720
- Yeh C et al. Diffusion microscopist simulator: a general Monte Carlo simulation for diffusion magnetic resonance imaging. PlosOne (2013) 8:1-12
- Yu X et al. Deciphering laminar-specific neural inputs with line-scanning fMRI. Nature Methods (2014) 11, 55–58

- Yu X et al. Direct imaging of macrovascular and microvascular contributions to BOLD fMRI in layers IV-V of the rat whisker-barrel cortex. NeuroImage (2012) 59:1451-1460
- Zhong K et al. Systematic investigation of balanced steady state free precession for functional MRI in the human visual cortex at 3T. Magn Reson Med (2007) 57:67-73
- Zhou I et al. Balanced steady state free precession fMRI with intravascular susceptibility contrast agent. Magn Reson Med (2012) 68:65-73
- Zielinski L. Sen P. Combined effects of diffusion, non-uniform gradient magnetic fields and restriction on an arbitrary coherence pathway. J Chem Phys (2003) 119:1093-1104
- Ziener C et al. Frequency autocorrelation function of stochastically fluctuating fields caused by specific magnetic field inhomogeneities. J Chem Phys (2008) 129:014507
- Ziener C et al. Scaling laws for transverse relaxation times. J Magn Reson (2007) 184:169-175
- Ziener C et al. Signal evolution in the local magnetic field of a capillary: analogy to the damped driven harmonic oscillator. Magn Reson Ima (2012) 30:540-553
- Ziener C et al. Structure-specific magnetic field inhomogeneities and its effect on the correlation time. MAgn Reson Med (2006) 24:1341-1347
- Ziener C, Bauer W, Jakob P. Frequency distribution and signal formation around a vessel. MAGMA (2005) 18:225-230
- Ziener C, Bauer W, Jakob P. Transverse relaxation of cells labeled with magnetic nanoparticles. Magn Reson Med (2005) 54:702-706
- Ziener CH et al. Local frequency density of states around field inhomogeneities in magnetic resonance imaging: effects of diffusion. Phys Rev E (2007) 76:1-16
- Zur Y et al. Motion Insensitive, steady state free precession imaging. Magn Reson Med (1990) 16:444-459

Appendix 1

The impact of vessel size, orientation and intravascular contribution on the neurovascular fingerprint of BOLD bSSFP fMRI

Mario Gilberto Báez-Yánez [1,2], Philipp Ehses[1,3], Christian Mirkes[1,4], Philbert S. Tsai[5], David Kleinfeld[5,6] and Klaus Scheffler[1,7*]

[1]Department of High-Field Magnetic Resonance, Max Planck Institute for Biological Cybernetics, Tuebingen, Germany.

[2]Graduate Training Centre of Neuroscience, University of Tuebingen, Tuebingen, Germany.

[3] German Center for Neurodegenerative Diseases (DZNE), Bonn, Germany.

[4]Skope Magnetic Resonance Technologies, Zurich, Switzerland.

[5]Department of Physics, University of California at San Diego, La Jolla, CA, USA.

[6]Section of Neurobiology, University of California, La Jolla, CA, USA .

[7]Department of Biomedical Magnetic Resonance, University of Tuebingen, Tuebingen, Germany.

[*]Correspondence to:

Klaus Scheffler, PhD

MPI for biological Cybernetics

Spemannstrasse 41

72076 Tübingen, Germany

klaus.scheffler@tuebingen.mpg.de

Keywords

Vascular cortical network

Layer specific BOLD fMRI

Orientation-dependent BOLD fMRI

Extra- and intravascular contribution

Balanced SSFP

Abstract

Monte Carlo simulations have been used to analyze oxygenation-related signal changes in pass-band balanced steady state free precession (bSSFP) as well as in gradient echo (GE) and spin echo (SE) sequences. Signal changes were calculated for artificial cylinders and neurovascular networks acquired from the mouse parietal cortex by two-photon laser scanning microscopy at 1 µm isotropic resolution. Signal changes as a function of vessel size, blood volume, vessel orientation to the main magnetic field B_0 as well as relations of intra- and extravascular and of micro- and macrovascular contributions have been analyzed. The results show that bSSFP is highly sensitive to extravascular and microvascular components. Furthermore, GE and bSSFP, and to a lesser extent SE, exhibit a strong dependence of their signal change on the orientation of the vessel network to B_0.

Introduction

The signal-to noise ratio of the MR signal increases more than linear with field strength (Ocali and Atalar, 1998; Wiesinger et al., 2004), and an increase with a power of about 1.7 was recently reported for brain imaging between 3T and 9.4T (Pohmann et al., 2016). Imaging at 7T or 9.4T therefore opens the possibility to resolve structures far below the thickness of 2-3 mm of the human neurocortex. Anatomical images with an isotropic resolution below 200 µm have been obtained at 9.4T (Budde et al., 2014; Lüsebrink et al., 2017) that clearly resolve subcortical structures such as the line of Gennari or subcortical units within the brain stem (Federau and Gallichan, 2016; Keuken et al., 2013; Deistung et al., 2013). Functional images based on the blood oxygenation level dependent (BOLD) effect and acquired with gradient echo or spin echo methods, in principle, may offer the same spatial resolution as anatomical images. Therefore, at very high fields the BOLD response from single cortical layers or other mesoscopic substructures might be resolved. However, while the spatial point-spread-function in structural images is basically given by a *sinc* function with a width given by the inverse of the sampled k-space

coverage, in functional BOLD imaging the neurovascular point-spread-function defines the resolution of a point-like neuronal event that is blurred by vascular-related changes related to tissue oxygenation, blood flow and blood volume.

So far, MR imaging is only able to detect vascular-related changes triggered by neuronal events or other physiological changes, like vasomotion (Murphy et al., 2013). Observed signal changes related to changing blood oxygenation levels within the neurovascular network depend on the chosen imaging modality. For example, it is well-known that spin echoes are selective to oxygenation changes from only small vessels in the range of 5 - 20 µm, whereas gradient echoes are sensitive to all vessel calibers larger than about 5 µm (Weisskoff et al., 1994; Boxerman et al., 1995). Furthermore, the neurovascular system is not a randomly oriented network of micro vessels but has a distinct geometry of surface vessels that are oriented parallel and penetrating vessels that are oriented perpendicular to the cortex surface (Weber et al., 2008; Blinder et al., 2013). Thus the orientation of the cortex to the main magnetic field might significantly influence the detected BOLD signal (Gagnon et al., 2015).

The susceptibility difference between (partially) deoxygenated blood and surrounding tissue produces a pattern of local magnetic fields. The protons of water molecules that diffuse within these local fields accumulate a certain phase of the transverse magnetization, which is then collectively detected within the volume of the imaging voxel via a gradient or spin echo (GE and SE), or after a train of refocusing pulses in the case of multiple gradient or spin echoes, or via a balanced steady state free precession (bSSFP) sequence. The dependence of single gradient and spin echoes as a function on the vessel size, vessel orientation, and blood volume fraction has been analyzed and described in several papers (Weisskoff et al., 1994; Boxerman et al., 1995). An open question is the origin of signal formation in bSSFP, which is of crucial importance to interpret the quality of BOLD bSSFP data with respect to the underlying neurovascular point spread function.

This paper focuses on the analysis and description of the neurovascular fingerprint of pass-band bSSFP, an imaging modality that has been introduced for functional

BOLD imaging in 2001 (at the stop-band, Scheffler et al., 2001), and that was further advanced by several groups (e.g. Bowen et al., 2005; Miller 2012; Scheffler and Ehses 2015). The formation of MR signal from water proton magnetization during a random walk through the neurovascular network is modeled using Monte Carlo simulations for artificial cylinders with different diameter and orientation, as well as for four different sets of neurovascular networks acquired from the mouse parietal cortex measured with two-photon laser scanning microscopy at 1 µm isotropic resolution (Blinder et al., 2013). In addition, selected Monte Carlo simulations of GE and SE have been performed to serve as a comparison to pass band bSSFP.

Models and simulations

Vascular model of the cortex

The underlying vascular structure for Monte Carlo simulations is based on cylinders with different diameter, blood volume (BV) fraction and orientation to the main magnetic field B_0, as well as on four vectorized vessel data sets of the mice parietal cortex that was acquired in a different study by Bilnder et al, 2013. In this study, the brains of adult mice were perfused for a fluorescent gel that preserved the volume of vessels. Approximately 1 mm^3 regions of primary vibrissa cortex, from the pia down to the white matter, were isolated and automated optical sectioned with 1 µm resolution. The resultant fluorescence was transformed into interconnected microvessels by matched filtering against cylindrical segments; corrections were made for breaks in the labeling (Kaufhold et. al., 2012). Finally, the fully reconstructed image was transformed into an annotated graph, where vessels are branches with a length and median width. Spatial and temporal changes in the local blood oxygenation, blood volume and flow have not been included both for the models based on the artificial cylinders and for the realistic neurovascular data sets. This represents an instantaneous change of blood oxygenation in all vessels. Thus, all vessels structures were either set to a nearly oxygenated state, i.e., a small

susceptibility difference between vessels and tissue mimicking the activated state, or to a partially deoxygenated state for the resting state condition.

Monte Carlo simulations

Monte Carlo simulations closely followed the recipes given by Boxermann et al. (1995), Weisskoff et al. (1994) and Bieri and Scheffler (2007). The susceptibility difference between blood and tissue for fully deoxygenated blood was set to $\Delta\chi$ = 0.11 ppm in cgs units, based on a hematocrit level of 40% and a susceptibility difference of fully deoxygenated red blood cells to tissue of $\Delta\chi$ = 0.273 ppm (Spees et al., 2001; Jain et al., 2012). A blood oxygenation level of Y = 77% for the resting state was assumed and Y = 85% for the fully oxygenated state (Vovenko, 1999; Gagnon et al., 2015). Applying a field strength of B_0 = 9.4T, a cylinder filled with Y = 77% oxygenated blood and oriented perpendicular to B_0 induces in a frequency shift of ±64 Hz at the cylinder surface and 21 Hz within the cylinder, according to the formula shown below (Chu et al., 1990).

$$\Delta\omega(\vec{r}) = 2\pi\gamma B_0 (1-Y)\Delta\chi \cdot \frac{R^2}{r^2} \cdot \cos 2\phi \cdot \sin^2\theta, \qquad r > R \qquad (1)$$

$$\Delta\omega(\vec{r}) = 2\pi\gamma B_0 (1-Y)\Delta\chi \cdot \left(\cos^2\theta - \frac{1}{3}\right), \qquad r \le R \qquad (2)$$

R is the cylinder radius and *r* is the distance between the spin and the central axis of the cylinder. The cylinder is at an angle θ with respect to B_0, and φ is the polar angle of the vector *r* in the plane perpendicular to the cylinder axis.

Similarly to the cylinders, a susceptibility difference $\Delta\chi$ of (1-Y) x 0.11 ppm was assigned to all vessels from the data sets of the parietal cortex of the mice. For simplicity, only the resting state using Y = 80% ($\Delta\chi$ of 0.022 ppm) was compared to the activated, fully oxygenated state with Y = 100% ($\Delta\chi$ = 0 ppm, resulting in a completely homogeneous field within the vessel network). The Finite Perturber Method was used to calculate the resulting frequency map (for a field strength of 9.4T) generated by the vessel models (Pathak et al., 2008; Jenkinson et al., 2004). This method applies a 3D Fourier transform to both the structural data and the field

distortion produced by a single finite perturber (sphere). The resulting Fourier-transformed maps are then multiplied and back Fourier-transformed to derive the final frequency distribution of the vessel network oriented at different angles to B_0 (0° to 90°).

Random walks of protons were calculated with a diffusion constant of D = 1.0 $\mu m^2/ms$ and time steps of Δt = 50 µs. For the simulation of the GE signal, an echo time TE of 20 ms was used and $1x10^5$ random walks were averaged. For the simulation of the SE signal, an echo time TE of 30 ms was used and $2x10^5$ random walks were averaged. The choice of TE = 20 ms versus 30 ms for GE versus SE roughly corresponds to the values used for fMRI at 9.4T (Budde et al., 2014). Pass-band bSSFP was simulated for different TEs, or repetition times TR = 2*TE, ranging from 5 to 20 ms with flip angles between 5° to 30° (using 180° phase cycling), and averaging between $5x10^3$ and $1x10^4$ random walks. Depending on the selected TR, the bSSFP signal was taken after 500 to 2500 dummy excitations to ensure a steady state signal. The fractional BV was varied between 1% and 5% for the artificial cylinders, and was between 0.7% and 5% for the measured vessel data sets. The contribution of intra- and extravascular protons was calculated separately, and the overall BOLD signal change is calculated as BV-weighted sum of these contributions. Diffusion of water protons through the vessel-tissue boundary was prohibited.

Relaxation times

In addition to dephasing effects produced by the inhomogeneous fields, signal changes are heavily dependent on the relaxation times of tissue and the times of oxygenated (active state) or partially deoxygenated (resting state) blood. The chosen relaxation times for tissue and blood strongly influence the resulting signal changes, especially for bSSFP but to a lesser extent for the GE and SE signals.

Relaxation times are closely related to the field strength. This has a significant impact on the relation of intra- and extravascular contributions. In particular, while intra- and extravascular T1 relaxation times are relevant for bSSFP simulations, as

both T1 and T2 contribute to the steady state signal, T1 does not contribute to single-echo GE or SE signals. We followed to literature vales (summarized in Fig. 2 in Khajehim and Nasiraei Moghaddam (2017)) and set both intra- and extravascular T1 to 2200 ms for 9.4T. Furthermore, no dependence of intravascular T1 on blood oxygenation was assumed (Blockley et al. 2008). As the steady state signal of bSSFP is approximately proportional to $\sqrt{(T2/T1)}$ (Sekihara K., 1987) and T2 is much smaller than T1 , 10 to 40 ms versus 2200 ms (see below), possible variations of T1 with blood oxygenation will hardly influence the results of the Monte Carlo simulations. In contrast, selection of appropriate T2 and T2* relaxation times is critical for both GE and SE, and also for bSSFP. In addition, for blood these relaxation times are closely linked to the oxygenation level Y and thus strongly control the intravascular contribution to the overall signal change. Currently there is no experimental data available for T2* of blood at 9.4T. For GE simulations we thus took the experimental data from 1.5 T, 3 T and 7 T (Blockley et al. 2008), and extrapolated the R2* relaxivity to 90 s^{-1} per mM deoxyhemoglobin at 9.4 T. For oxygenation levels of 77 % (rest) and 85 % (activated), this corresponds to T2* relaxation times of about 4 ms and 8 ms, respectively.

For GE, SE and bSSFP, T2 of the extravascular space was set to 41 ms (Uludağ et al. 2009). As the signal decay in extravascular space is mainly driven by dephasing effects within the inhomogeneous fields around the vessels, the choice of T2 is not critical. For SE with a single echo, a T2 of blood of 12 ms (Y = 77 %) and 20 ms (Y = 85 %) was used (Uludağ et al. 2009). In the case of rapidly refocused bSSFP or trains of spin echoes, T2 also depends on the refocusing interval, and becomes longer with shorter TR (Dharmakumar et al., 2005; Kurz et al., 2016; Gardener et al., 2010; Grgac et al., 2017). As currently no T2 data of blood with rapid bSSFP refocusing is available, multiple values for the relaxation time T2 were compared in Monte Carlo simulations, i.e., T2 for Y = 77% of 12 ms (corresponding to T2 of a single echo) and 20 ms (narrowing by rapid refocusing), and 20 ms (single echo) and 40 ms (rapid refocusing) for Y = 85%. This choice of T2 for Y = 77 % of 12 and 20 ms, and T2 for Y= 85 % of 20 and 40ms roughly corresponds to estimations from

literature performed under slightly different conditions (Khajehim and Nasiraei Moghaddam, 2017; Dharmakumar et al., 2005). However, no significant differences of intravascular contributions in bSSFP between the T2 pairs of 12 and 20 ms (rest) and 20 and 40 ms (activated) have been observed. Therefore, all bSSFP simulations shown below are based on a blood T2 of 12 ms at rest (Y = 77%), and 20 ms for activation (Y = 85%).

All BOLD-related signal changes shown in Figs. 1-6 are relative signal changes in percent of $(S_{Y=85\%}-S_{Y=77\%})/S_{Y=85\%}$ separately for intra- and extravascular or combined signal contributions. An overview of the parameters used for Monte Carlo simulations are given in Table 1.

	Y_{rest}	Y_{act}	Vessel radius	Blood volume	TR for bSSFP	Flip angle for bSSFP	Blood T1/T2 for bSSFP	Blood T1/T2 for SE	Blood T1/T2* for GE	Extra-vascular T1/T2
Random/ parallel cylinders	77 %	85%	0.5 – 200 µm	1% - 5%	5 - 20 ms	5° - 30°	Rest: 2200/ 12 ms Act: 2200/ 20ms	Rest: 2200/ 12ms Act: 2200/ 20ms	Rest: 2200/ 4 ms Act: 2200/ 8 ms	2200/ 41 ms
Vessel data	80 %	100 %	1.0 – 40 µm	0.1% - 5%	5 ms	20°				

Table 1: Summary of parameters used in Monte Carlo simulations. Rest/Act refers to the resting/activated state with different oxygenation levels Y_{rest}/Y_{act}.

In vivo measurements

A high-resolution functional pass-band bSSFP experiment was performed at 9.4 T on a healthy volunteer with approval by the local ethics committee. The parameters of the 3D bSSFP protocol were as follows: TR = 4.2 ms, TE = 2.1 ms, nominal FA = 15°, resolution = 0.6x0.6x0.6 mm^3, 16 slices. To accelerate imaging, GRAPPA R=3 acceleration was used in combination with 5/8 partial Fourier (POCS reconstruction) and elliptical scanning. This resulted in a volume TR of 3.76 s (Scheffler and Ehses, 2015). A flickering radial checker-board was used as a visual stimulus (7 Hz), which was presented for 9 min in alternating 13 s off- and 20 s on-periods. Functional analysis was performed after motion correction using AFNI (Cox, 1996) with FSL's FEAT (Smith et al., 2004) using standard parameter settings and no spatial smoothing. For comparison and vein detection, a high-resolution T2*-weighted GE reference was acquired with the following sequence parameters: TR = 700 ms, TE = 12 ms, nominal FA = 70°, resolution = 0.4x0.4x0.7 mm^3, 40 slices.

Results

We first consider a comparison of the sensitivity to the vessel radius between GE, SE and pass-band bSSFP (FIg. 1). These simulations are based on cylinders at random orientation occupying different BV fractions from 1 % to 5 %. In accordance with past results (Boxermann et al. 1995 and Weisskoff et al. 1994), GE has an unspecific sensitivity to all vessel sizes larger than about 5 µm as a consequence of static dephasing, and a linear dependence of the signal change with BV (Fig. 1a). Similarly, SE shows its typical selectivity to vessel radii between 2 to 10 µm and almost no signal change for larger vessels in the static refocusing regime (Fig. 1b). As for GE, the peak sensitivity in SE scales linearly with the fractional BV. The bSSFP profile is similar to the SE profile (Fig. 1b, c), however, it does not return to zero sensitivity for larger vessels, and has a slightly broader response to the vessel size in accordance to previous work (Bieri and Scheffler, 2007; Kim et al., 2012).

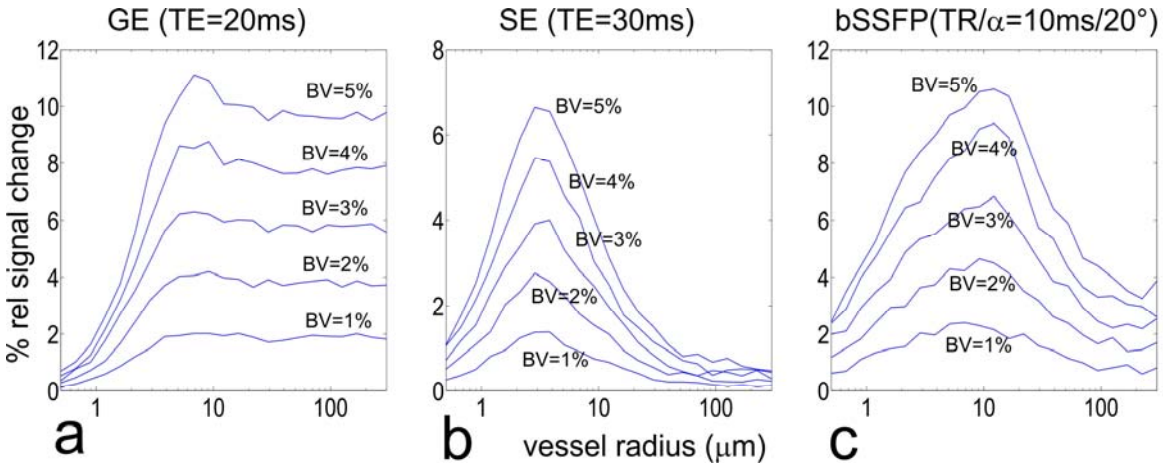

Fig. 1: BOLD signal change of GE, SE and bSSFP as a function of vessel radius (randomly oriented cylinders) for different fractional BV. Blood oxygenation of Y=77% and Y=85% was assumed for the resting and activated state, respectively, at a field strength of 9.4T.

We next consider the dependence of the BOLD bSSFP signal change as a function of different TRs and flip angle (Fig. 2). All simulations show a peak around small vessel radii of about 2 to 10 μm which slightly varies with the chosen TR. With increasing TR (Fig. 2a-c) the vessel size selectivity shifts to larger radii and the peak signal change is strongly increased, i.e., by a factor of 3-4 going from TR=5ms to 20 ms. Also, for longer TR, greater than approximately 10 ms, the contribution from larger vessels (> 100 μm) increases to up to 50% of the peak signal. The BOLD-related signal change increases with flip angle up to about 20° by a factor of about 2-3, and shows no further increase for higher flip angles (Fig. 2d-f).

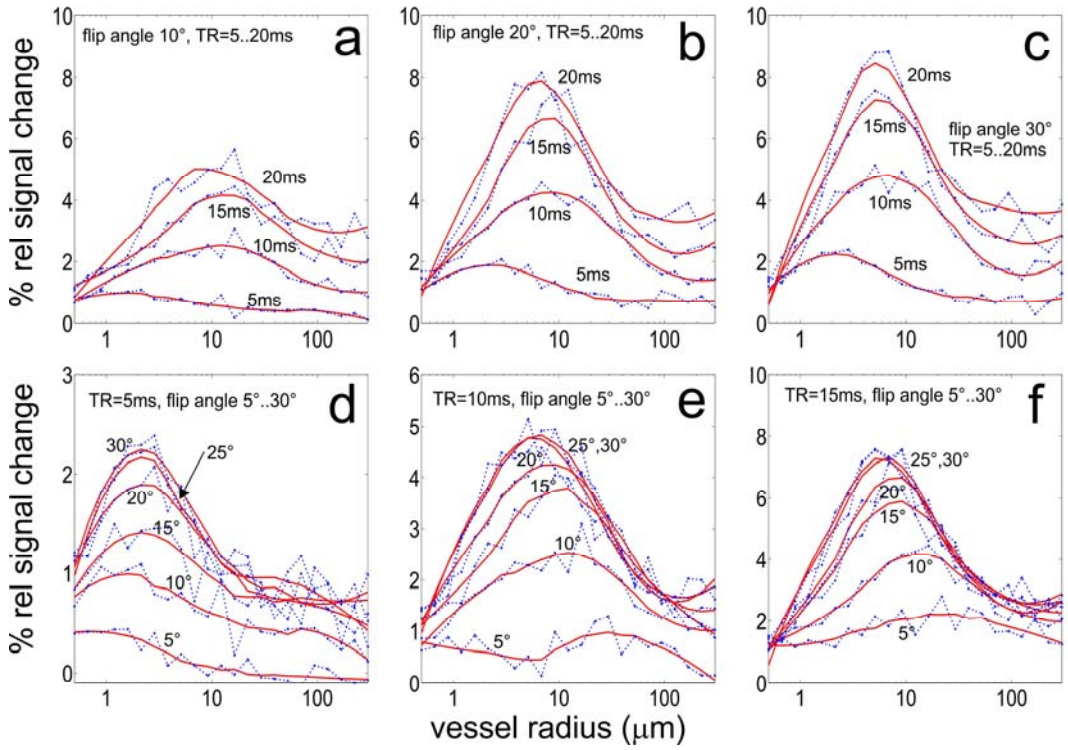

Fig. 2: Extravascular BOLD signal change for bSSFP for different TR and flip angles as a function of the vessel radius (red lines are polynomial fits to the simulation results (in blue)). Blood oxygenation of Y=77% and Y=85% was assumed for the resting and activated state, respectively, at a field strength of 9.4T. Intravascular blood T2 was set to T2=12ms for the resting state and T2=20ms for the activated state. The fractional BV of the randomly oriented cylinders was set to 2% for all simulations.

The intra- and extravascular signal contribution as a function of BV, for vessel radii between 2 and 100 μm, was calculated for GE, SE and bSSFP (Fig. 3). For GE, where a blood T2* of 4 ms (resting state Y=77%) and 8 ms (activated state Y=85%) at 9.4T was assumed, the intravascular contribution is negligible for all BV and vessel radii (Fig. 3a). Similarly, for SE with blood T2 of 12 ms and 20 ms the intravascular contribution is small compared to the extravascular contribution for vessel radii between 2 and 12 μm (Fig. 3b). However, the extravascular SE signal drops for

larger vessel radii and is comparable to the intravascular signal change for vessels radii between 20 to 100 µm. In bSSFP, the relation between intra and extra vascular contribution is similar to SE for small vessels between 2 to 20 □m, so it is mainly dominated by extravascular contributions (Fig. 3c). As the BOLD signal change for bSSFP at vessel radii larger than 50 µm does not completely disappear (but in SE; Fig. 1), intra- and extravascular contributions become comparable at this domain.

The images in Fig. 3d show the response in the visual cortex upon checker board simulation with a T2*-weighted GE image (top) and functional activation in a 0.6 mm isotropic resolution bSSFP acquisition (bottom) with TR = 4.2 ms and nominal flip angle of 15°. The small vein penetrating into the cortex shows a strong BOLD response. The BV of pixels close or within this vein is close to 100%, and thus the signal change is only produced by the intravascular signal. This signal change only depends on the T2 change of blood from 12 ms (rest) to 20 ms (activated), and as the bSSFP signal is proportional to about √(T2/T1) this change is in the range of 20 - 50%.

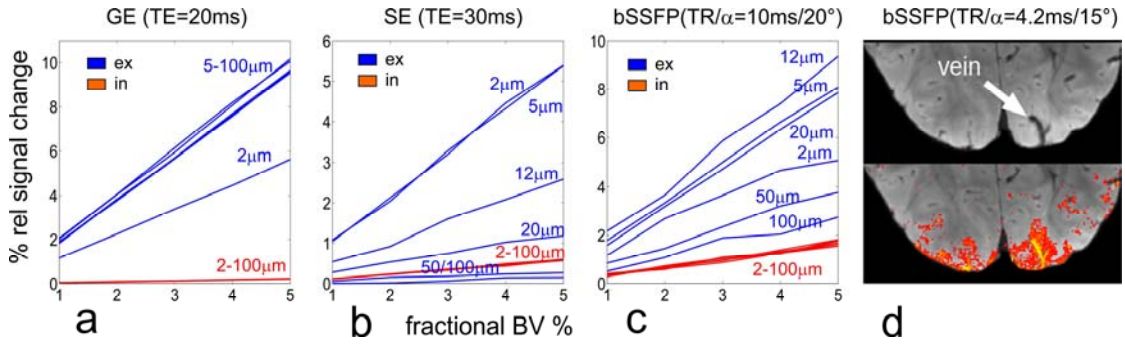

Fig. 3: Relation between intra- (red) and extravascular (blue) contribution for GE, SE and bSSFP based on randomly oriented cylinders as a function of fractional BV and for radii varying from 2 to 100 □m. Blood T2* was set to T2*=4ms and 8ms for GE, T2=12ms and 20ms for SE and bSSFP for the resting and activated state, respectively. The image on the right top shows a GE measurement (TE= 12 ms) depicting a larger vein (white arrow). Below is a functional activation map (visual

checkerboard stimulation, 0.6 mm isotropic resolution) overlaid onto the GE image. The strong intravascular signal from a draining vein is clearly visible.

In Figure 4, only parallel cylinders with a certain angle to B_0 have been simulated. This mimics a very simplified model of parallel diving (penetrating) veins and arteries oriented perpendicular to the cortical surface. For GE, basically all vessel radii exhibit a strong dependence of the signal change on the cylinder orientation to B_0. For bSSFP simulated at TR = 5 ms, only small vessels (1 to 10 µm) depend on their angle to B_0, larger vessels just give a very small signal change, which is similar to the SE behavior shown right. As the bSSFP sensitivity to larger vessels increases with TR (see Fig. 2), the bSSFP simulation using TR = 15 ms shows some signal dependence on orientation to B_0 also for larger vessels around 50 to 200 µm.

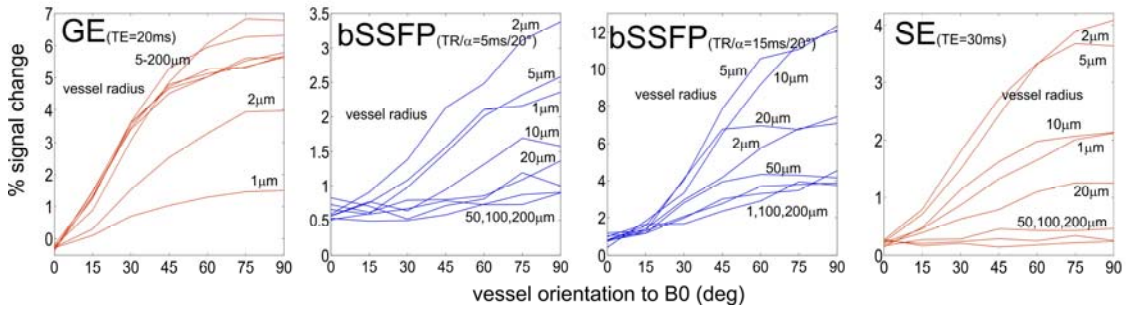

Fig. 4: BOLD signal change as a function of the orientation of the vessel (cylinder) to B_0 for GE, bSSFP and SE for different vessel radii ranging from 1 to 200 µm, and for a fractional BV of 2%.

Figure 5 summarizes the distribution of vessel length, the orientation angle of vessels to the surface normale and the diameter and tortuosity, calculated from the vessel data sets (Blinder et al., 2013). Both venules and arterioles are mostly oriented parallel to the surface normal. However, due to the curvilinear nature of the cortical surface, the vertical axis of the dataset did not always locally match the surface perpendicular. We quantify the average offset of the local surface norm from the

vertical axis of the dataset to be 6.2 +/- 3.1 degrees. Regarding capillary orientation, the data show a clear bias to be perpendicular to the normal.

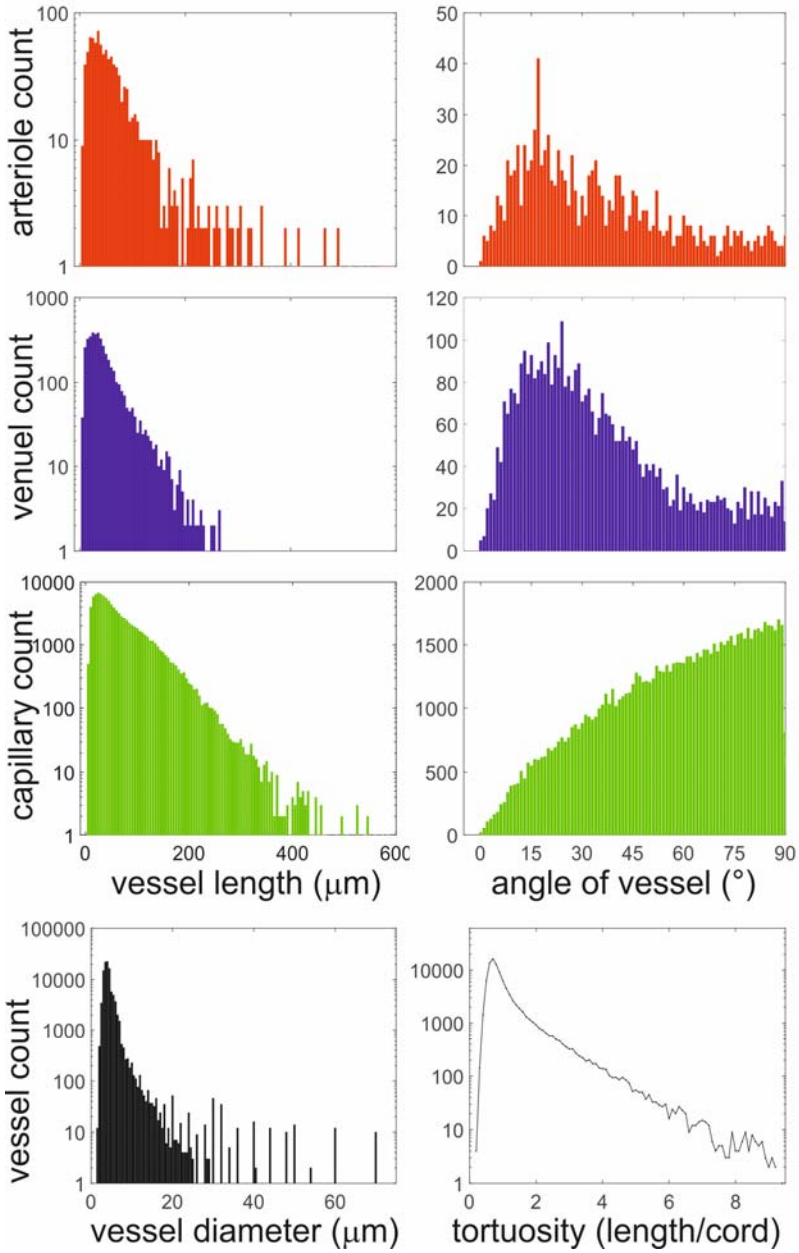

Fig. 5: Top: Vessel length and angle of vessels to the surface normal for arterioles, venules and capillaries (diameter < 7mm), averaged over the four data sets shown in Figure 7. Bottom: Distribution of vessel diameter and tortuosity (length divided by the cord (end-to-end length)) for all vessel types.

Simulations based on reconstructed cortical neurovascular network were performed by dividing each network into six equally spaced layers starting from the top showing the large cortical surface vessels (layer 1) down to the boundary of grey and white matter (layer 6) (right panels, Fig. 6A-D). The Larmor frequency distribution within the layers was calculated by the Finite Perturber Method. As layer 1 includes the large cortical surface vessels, the corresponding frequency distribution is much broader compared to deeper layers (left panels, Fig. 6A-D). However, the layer-specific frequency distributions show a large variation across the four different data sets. The width of the frequency distribution for layers 2 to 6 varies between ±5 and ±15 Hz. In addition, the frequency distribution of data sets B, C and D is more symmetric compared to A. The signal changes shown in the right part of Fig. 6 are strongest for the surface layer 1, and they decrease by about a factor of 4 to 6 for GE and about 2 to 3 for SE and bSSFP going towards the deeper layers. The simulated functional signal change for GE (TE=20ms), SE (TE=30ms) and bSSFP (TR/α=5ms/20°), as well as local fractional BV for each layer, is seen (right panels, Fig. 6A-D). Functional signal changes were calculated for two orientations of the vessel network to B_0, 0° (dotted line, surface perpendicular to B_0) and 90° (solid line, surface parallel to B_0). For GE, a very strong signal change increase can be observed towards the surface layer 1 which is less pronounced for bSSFP and SE. A certain dependence on the orientation to B_0 is visible for all modalities, but is strongest for GE. The effect on orientation is inverted, starting from the surface layer to deeper layers, and occurs since surface vessels are mostly perpendicular to the penetrating vessels.

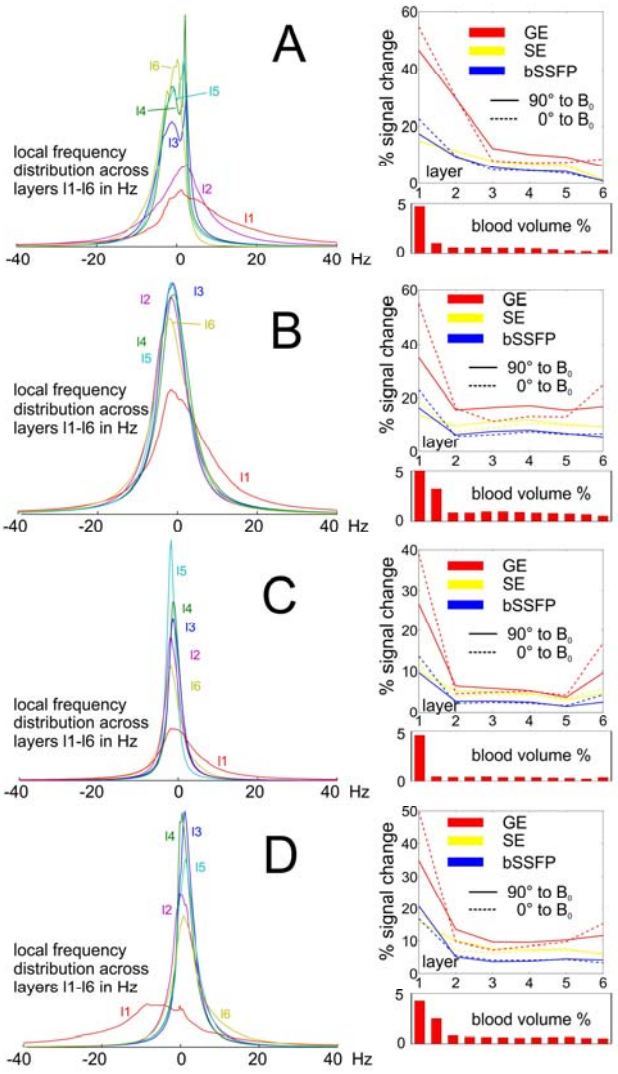

Fig. 6: The left column shows the frequency distribution (assuming $\Delta\chi = 0.22 \times 10^{-7}$ at 9.4T and with the top surface of the vessel network oriented perpendicular to B_0) around the vessel network for layers I1 to I6 for the four different data sets A to D shown in Fig. 6. The right column shows BOLD signal changes for GE (TE=20ms), SE (TE=30ms) and bSSFP (TR/α=5ms/20°) across layers I1 to I6 oriented perpendicular (0°, dotted line) and parallel (90°, solid line) to B_0. The corresponding fractional BV across layers extracted from the data set is shown below each plot.

The signal change dependence on the orientation of the cortex to B_0 is summarized in figure 7. The left column shows renderings of the four vectorized vessel data sets of the mice parietal cortex. The three columns on the right show signal changes for GE (TE=20ms), SE (TE=30ms) and bSSFP (TR/α=5ms/20°) as a function of the orientation to B_0, where for 0° and 180° the penetrating vessels are parallel, and surface vessels are perpendicular to B_0. The calculated signal changes are relative to the change observed at 90° and were calculated in percent by 100 x ($\Delta S_{\theta z}$-$\Delta S_{90°}$)/$\Delta S_{90°}$ for each of the six layers and for the mean signal across layers shown in red.

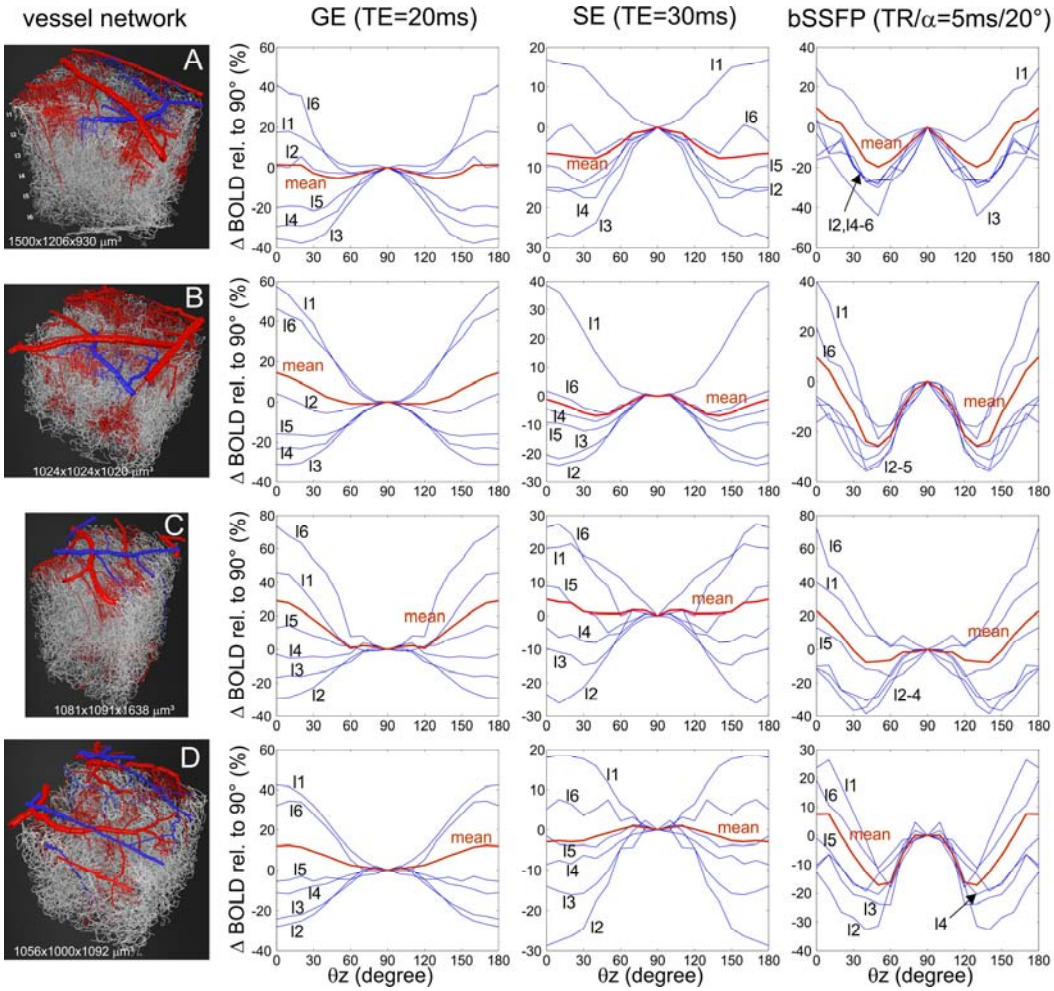

Fig. 7: The left column depicts the rendered vessel data sets used for Monte Carlo simulations. The three right columns show the orientational and layer-specific

dependence of GE, SE and bSSFP as relative percentage change to the reference at 90° (layer surface parallel to B_0 or penetrating vessels perpendicular to B_0). The red curves are the mean through all layers, i.e. represent the BOLD response of the entire cortical structure. For simplicity, orientations for $\theta > 90°$ were set equal to those of $\theta_{>90°} = 180° - \theta_{<90°}$.

Discussion

The presented results are all based on Monte Carlo simulations assuming a certain global oxygenation change between Y = 77% and Y = 85%, and for a field strength of 9.4T. In general, the frequency pattern around cylinders or vessels scales linearly with oxygenation and field strength, and thus the resulting signal change strongly depends on these parameters. However, the basic characteristics of the presented plots, such as the selectivity to a certain vessel radius, the dependence on the fractional BV and the orientational dependence, do not depend on the particular choice of the selected parameters. Similar shapes of signal changes as a function of the vessel size and fractional BV have been reported for GE, SE and bSSFP (Boxermann et al., (1995); Weisskoff et al., (1994); Bieri and Scheffler, 2007; Kim et al., 2012; Khajehim and Nasiraei Moghaddam, 2017). Similarly, the choice of relaxation times of the extra- and intravascular space has an impact on the overall signal changes, and more significantly also on the relation of intra- and extravascular contributions. As far as possible, the selected relaxation times were taken from literature values, or they were extrapolated to 9.4T.

Specificity to the capillary and non-capillary network

The well-known behavior of GE, SE and pass-band bSSFP as a function of vessel (cylinder) size could be confirmed in Fig. 1. Experimental comparisons between GE and bSSFP in functional checker board experiments at 9.4T, however, show a lower signal change for bSSFP compared to GE (Scheffler and Ehses, 2015), in contrast to signal changes presented in Fig. 1. This might be related to the vessel size

selectivity of bSSFP, as larger vessels contribute to GE but less to bSSFP. Compared to SE, bSSFP shows a slightly larger contribution for vessels larger than 50 µm, which can be attributed to the stronger intravascular effect compared to SE, see below.

The shape as well as the peak of the curve that describes the bSSFP signal change as a function of vessel radius depend on TR and flip angle. The curves shown in Fig. 2 are similar to those shown in other publications that used largely different parameters for their simulations (Bieri and Scheffler, 2007; Kim et al., 2012; Khajehim and Nasiraei Moghaddam, 2017). An increase in TR gives a much higher signal change, and in parallel, an increasingly contribution from larger vessels (> 50 µm). An increase of the flip angle to about 20° to 25° also boosts the signal change as shown in the bottom row of Fig. 2, similar to the results shown in Kim et al. (2012), Miller and Jezzard, (2008) and Khajehim and Nasiraei Moghaddam, (2017). The contribution of vessels larger than 50 µm is less pronounced for increasing flip angles (bottom row in Fig. 2) than for increasing TRs (top row). For experimental applications a longer TR of 10 to 15 ms thus seems to be beneficial. In addition, higher flip angles can be used due to the lower power deposition. A drawback of longer TRs at very high fields is increased banding artifacts.

According to the plots in Fig. 1 and 2, the BOLD signal ratio, which can be defined as the ratio of the contributions from the laminar vasculature and from intracortical veins (Markuerkiaga, I. et al., 2016), is significantly different for GE, SE and bSSFP. Assuming a laminar network that consists of vessels of up to 10 □m and that occupy 2.3% BV (Weber et al., 2008; Boas et al., 2008), and intracortical veins between 10 □m to 70 µm and an averaged BV across layers of 0.6% (from 0.2% at layer 6 linearly increasing to 1.2% at the top layer 1, Cassot et al., 2006; Duvernoy et al, 1981), the BOLD signal ratio (laminar vasculature: intracortical veins) of GE (TE=20ms) amounts to 10:1 (layer 6) to 1.7:1 (top layer 1), that of SE (TE=30ms) to 34:1 to 6:1, and 22:1 to 4:1 for bSSFP (TR/α=10ms/20°). Averaged over the cortex thickness and using a mean intracortical vein BV of 0.6%, the BOLD signal ratio amounts to

3.2:1 for GE, 12:1 for SE, and 7.5:1 for bSSFP. Thus, the BOLD signal ratio, i.e. the selectivity to oxygenation changes in capillaries and venules is highest for SE, followed by bSSFP (depending on TR of bSSFP) and is much lower for GE. However, it should be noted that most functional studies using SE are based on SE-EPI readouts that show a T2* decay around the spin echo that is usually placed in the center of k-space. The resulting T2*-related blurring will thus introduce a certain GE-type weighting, depending on the resolution and acceleration factor. Thus, as bSSFP only acquires one single k-space line per TR, the GE contribution in bSSFP might be comparable or even less compared to SE-EPI.

Furthermore, all sequences show an increased BOLD signal change towards the cortical surface, as shown in Fig. 6. The frequency distribution around the vessels based on the measured optical data set depends on the layer level. The observed signal change thus depends on the chosen resolution of the functional imaging sequence: if a single voxel covers the entire thickness of the cortex, about 50% of the signal change is produced by surface vessels for GE, but only about 10 to 20% for SE and bSSFP (assuming an isotropic resolution of 2-3 mm as commonly used in functional studies). Thus, SE and bSSFP capture significantly more responses from deeper layers compared to GE. At higher resolution, however, the BOLD signal ratio becomes more similar across sequences, except for the surface layer 1.

Intra- versus and extravascular signals

The contribution of intra- and extravascular signals for different fractional BV is shown in Fig. 3 for GE, SE and bSSFP, as well as an experimental example depicting a larger draining vein. As mentioned above, diffusion of water between intra- and extravascular space was prohibited in the simulations. However, allowing water to cross vessel boundaries with a probability of 10% (Eichling et al., 1974; Paulson et al., 1977) does increase the intravascular contribution for all acquisition modalities, and especially for very small vessels. We did not include these data here, but it might offer a method to probe vessel permeability. The results shown in Fig. 3 strongly depend on the chosen intravascular T2 and T2* relaxation times, which were set to

4 ms and 8 ms for GE, and 12 ms and 20 ms for SE and bSSFP, for the resting and activated state, respectively. Intravascular T2* at 9.4T is very small and thus does not produce a significant intravascular signal for GE, but it increases with lower field strength (Gomori et al., 1987; Silvennoinen et al., 2003; Blockley et al., 2008). GE shows a strong and similar extravascular signal for all vessels larger than 5 µm. For SE only vessels between 2 to 10 µm produce a much stronger extravascular signal compared to vessels larger than 20 µm and to the intravascular signal. BSSFP is somewhat less selective compared to SE: vessels larger than 50 µm produce similar intra- and extravascular signals, smaller vessels are more extravascular-weighted. Thus, the signal characteristic of bSSFP is comparable to that of SE providing a strong signal change only for small vessels. The image on the right in Fig. 3 shows an example of high-resolution functional bSSFP with a huge activation in a vein of about 1 mm diameter. In this case, the fractional BV is almost 100% and the signal is thus solely given by the T2 change of blood. Therefore, in case of very high BV within the voxel, bSSFP gives a strong functional response in contrast to GE for which the strong T2* decay almost completely destroys the signal. However, for BVs below about 5 % (which is typical or even smaller for gray matter, except for the surface vessels, see Fig. 6), bSSFP (as SE) is mostly responsive to capillaries and less sensitive to the larger diving vessels. Significantly different results for the relation of intra- and extravascular contribution have been reported in a Monte Carlo simulation by Kim et al. (2012). Fig. 4 in the Kim paper shows a more than 60% intravascular contribution to the overall signal at 3T, however, the used T2 relaxation times for blood are not explicitly given. The intravascular contribution increases linearly with BV and, for example, contributes to about 1.5% for GE, 7% for SE and 11 % for bSSFP to the overall signal change at 9.4T and a BV of 30%, often found in pathological tissue such as brain tumors. In general, the intravascular contribution is larger at lower fields and reduced at larger fields due to the dependency of T2/T2* on field strength.

Orientational bias

The dependence of the signal change on the orientation of the cortex to B_0 clearly demonstrates, that the vessel structure is highly oriented and far from being a randomly oriented set of cylinders. A periodic dependence can be observed in all plots shown on the right-hand side in Fig. 7 across all layers, and also a phase or angle shift of 90° between layers 1, 6 and layers 2-5. This indicates that vessel orientations between these layers are perpendicular to each other. Furthermore, there seems to be a striking difference of the orientational signal dependence in bSSFP compared to GE and SE: while the angular signal dependence in GE and SE mostly shows one period of signal changes within 0° to 180°, the bSSFP response for single layers as well as for the mean across layers seems to be slightly bi-periodic. This is also partially the case for SE but only for the mean response. Based on Fig. 4 this might be explained by the fact that even for small vessels in the range of 1 to 20 µm the vessel network is not randomly oriented but has a vessel structure that is partially oriented perpendicular to each other, such as capillaries that branch perpendicular to the diving or ascending vessels. Such structures have been presented for example in Gagnon et al., (2015), Weber et al., (2008) and Blinder et al., (2013). However, it remains open if this bi-periodic behavior can be generalized to different cortical areas or even to humans, or subcortical vessel networks. A similar, mono-periodic dependence has been reported by Gagnon et al. (2015) and Fracasso et al. (2017) and Kurz et al. (2017) based both on experiments and Monte Carlo simulations. However, these data show a much stronger angular dependence for GE compared to SE (bSSFP was not analyzed there). In our simulations all sequences show an angular dependence for both single layers and mean signals, however, to a lesser extend for SE compared to GE, and largest and bi-periodic for bSSFP. The dependence of the signal change on the orientation of the cortex to B_0 has implications for any quantitative or calibrated measurement of oxygenation changes or contrast agent-induced susceptibility changes as used, for example, in first-pass contrast-enhanced perfusion measurements. The derived results of such studies might be strongly biased by the local orientation of the cortex to B_0, and we

are thus currently starting experiments with blood pool SPIO contrast agents to precisely describe and quantify these effects for different field strengths, resolution, and sequence types.

Limitations of this study

In general, a limitation of this study is the simplified assumption of a certain susceptibility difference between all vessels types and surrounding tissues without any dynamic and spatially varying patterns of oxygenation and blood volume changes. Therefore, our results do not contribute to the question, whether layer-specific neuronal activation can be detected with GE, SE or bSSFP. As shown in Fig. 6, a prerequisite for layer-specific activation is a sufficiently high spatial resolution, as otherwise the major response is induced by surface vessels, especially for GE. However, disentangling responses from different layers probably requires a detailed knowledge of the spatially resolved oxygenation and blood volume dynamics. Some excellent examples of these dynamic changes of oxygenation and flow based on optical methods are shown in Boas et al. (2008), Gagnon et al. (2015) and Schmid et al. (2017). As these oxygenation patterns rapidly propagate through the cortex within fractions of seconds, only a very rapid fMRI method with very high resolution might be able to capture these layer-specific changes.

Furthermore, the BOLD signal characteristics of GE, SE and bSSFP shown in Figs. 6 and 7 are related to the vessel architecture of the mouse parietal cortex. An analysis of other cortical or subcortical regions in animals or humans would be of high interest, however, to our knowledge currently no such high-resolution data is available. Another critical parameter is diffusion of water across the vessel boundary at high fields. The very short T2 or T2* of blood together with diffusion into and out of the vessels act as a relaxation mechanism. In our simulation we assumed non-permeable vessels, but according to literature there is a small diffusion permeability coefficient for water passage across the blood brain barrier of about $2x10^{-6}$m/s (Eichling et al., 1974; Paulson et al., 1977). This increases the BOLD signal change

especially for larger vessels (20 to 200 mm) in SE and bSSFP and thus reduces the selectivity to smaller vessels.

Conclusion

The main reason to choose ultra-high field is the relatively low sensitivity of bSSFP to BOLD changes at much lower fields, and pass-band bSSFP is thus probably not a good candidate for fMRI at 1.5T and 3T compared to GE. At higher fields of 7T or more, bSSFP provides a sensitivity that is almost comparable to SE (Scheffler and Ehses, 2015) and thus represents an alternative method to fMRI compared to GE with the advantage of being more selective to the microvasculature. Furthermore, application of SE-EPI at ultra-high fields is limited by SAR constrains, whereas full brain coverage with bSSFP is feasible even at 9.4T. At 9.4T, the intravascular contribution is negligible for GE, and depending on the BV, increases to about 5% - 10% of the overall BOLD signal change for SE and bSSFP. Except for larger veins that occupy a huge volume fraction of the imaging voxel, bSSFP is mostly sensitive to extravascular contributions from small vessels. The BOLD signal ratio between microvessels and intracortical veins is highest for deep layers (about 20:1) and decreases to about 4:1 for the surface layer for bSSFP. Thus, the contribution of larger cortical veins is in the range of 5% to 20%, indicating a strong sensitivity of bSSFP to the microvasculature. All sequences show a strong dependence on the orientation of the cortical layers to B_0 due to perpendicularly arranged feeding and draining vessels. Especially for SE and bSSFP, this observation needs to be confirmed in further, experimental studies, but it might have a significant impact on any quantitative or calibrated BOLD or perfusion measurements.

Acknowledgement

Mario Gilberto Báez-Yánez is thankful for the support by CONACYT (Consejo Nacional de Ciencia y Tecnología, México), and we also thank the NIH-NINDS (grant R35NS097265) and the NIH-NIMH (1R01MH111438) for funding.

References

Bieri, O., Scheffler, K., 2007. Effect of diffusion in inhomogeneous magnetic fields on balanced steady-state free precession. NMR Biomed. 20, 1–10.

Blinder, P., et al., 2013. The cortical angiome: an interconnected vascular network with noncolumnar patterns of blood flow. Nature Neuroscience 15 (7), 889-97.

Blockley,N.P., et al., 2008. Field Strength Dependence of R1 and R*2 Relaxivities of Human Whole Blood to ProHance, Vasovist, and Deoxyhemoglobin. Magn. Reson. Med. 60,1313–1320.

Boas, D.A., et al., 2008. A vascular anatomical network model of the spatio-temporal response to brain activation. NeuroImage 40 (3), 1116–1129.

Bowen, C.V., et al., 2005. High field balanced-SSFP FMRI: a BOLD technique with excellent tissue sensitivity and superior large vessel suppression. Proc 13th ISMRM, Miami, p. 119.

Boxerman, J.L., et al., 1995. MR contrast due to intravascular magnetic-susceptibility perturbations. Magn. Reson. Med. 34, 555–566.

Budde, .J, et al., 2014. Functional MRI in human subjects with gradient-echo and spin-echo EPI at 9.4 T. Magn Reson Med. 71(1), 209-18.

Budde, J., et al., 2014. Ultra-high resolution imaging of the human brain using acquisition-weighted imaging at 9.4T. Neuroimage. 1 (86), 592-8.

Cassot, F., et al., 2006. A novel three-dimensional computer-assisted method for a quantitative study of microvascular networks of the human cerebral cortex. Microcirculation (New York, N.Y.: 1994) 13 (1), 1–18.

Chu, S., et al., 1990. Bulk magnetic susceptibility shifts in NMR studies of compartmentalized samples: use of paramagnetic reagents. Magn. Reson. Med. 13, 239-262.

Cox, R.W., 1996. AFNI: software for analysis and visualization of functional magnetic resonance neuroimages. Comput Biomed Res. 29(3), 162–73.

Deistung, A., et al., 2013. High-Resolution MR Imaging of the Human Brainstem In vivo at 7 Tesla. Front. Hum. Neurosci. 7, 710.

Dharmakumar, R., et al., 2005. Oxygen-Sensitive Contrast in Blood for Steady-State Free Precession Imaging Magn. Reson. Med. 53, 574–583.

Duvernoy, H.M., et al., 1981. Cortical blood vessels of the human brain. Brain Res. Bull. 7 (5), 519–579.

Eichling, J.O., et al., 1974. Evidence of the limitations of water as a freely diffusible tracer in brain of the rhesus monkey. Circ Res. 35(3), 358-64.

Federau, C., Gallichan, D., 2016. Motion-Correction Enabled Ultra-High Resolution In-Vivo 7T-MRI of the Brain. PLoS ONE. 11(5):e0154974.

Fracasso, A., et al., 2017. Laminar imaging of positive and negative BOLD in human visual cortex at 7T. Neuroimage. pii: S1053-8119(17)30149-0. doi: 10.1016.

Gagnon, L., et al., 2015. Quantifying the microvascular origin of BOLD-fMRI fromfirst principles with two-photon microscopy and an oxygen-sensitive nanoprobe. J. Neurosci. 35 (8), 3663–3675.

Gardener, A.G., et al., 2010. Dependence of Blood R2 Relaxivity on CPMG Echo-Spacing at 2.35 and 7 T. Magn. Reson. Med. 64, 967–974.

Gomori , J.M., et al., 1987. NMR relaxation times of blood: dependence on field strength, oxidation state, and cell integrity. J Comput Assist Tomogr. 11, 684–690.

Grgac, K., et al., 2017. Li W, Huang A, Qin Q, van Zijl PC. Transverse water relaxation in whole blood and erythrocytes at 3T, 7T, 9.4T, 11.7T and 16.4T; determination of intracellular hemoglobin and extracellular albumin relaxivities. Magn Reson Imaging. 38, 234-24.

Jain, V., et al., 2012. Investigating the magnetic susceptibility properties of fresh human blood for noninvasive oxygen saturation quantification. Magn. Reson. Med. 68 (3), 863-7.

Jenkinson, M., et al., 2004. Perturbation method for magnetic field calculations of nonconductive objects. Magn. Reson. Med. 52, 471–477.

Kaufhold, J.P., et al., 2012. Vectorization of optically sectioned brain microvasculature: learning aids completion of vascular graphs by connecting gaps and deleting open-ended segments. Med Image Anal. 16 (6), 1241-58.

Keuken, M.C., et al., 2013. Ultra-high 7T MRI of structural age-related changes of the subthalamic nucleus. J Neurosci. 33 (11), 4896–4900.

Khajehim, M., Nasiraei Moghaddam, A., 2017. Investigating the spatial specificity of S2-SSFP fMRI: A Monte Carlo simulation approach. Magn Reson Imaging. 37, 282-289.

Kim, T.S., et al., 2012. Analysis of the BOLD Characteristics in Pass-Band bSSFP fMRI. Int J Imaging Syst Technol. 22 (1), 23–32.

Kurz , F.T., et al., 2016. CPMG relaxation rate dispersion in dipole fields around capillaries. Magnetic Resonance Imaging. 34, 875–888.

Kurz, F.T., et al., 2017. The influence of spatial patterns of capillary networks on transverse relaxation. Magnetic Resonance Imaging 40, 31–47

Lüsebrink, F., et al., 2017. T1-weighted in vivo human whole brain MRI dataset with an ultrahigh isotropic resolution of 250 μm. Sci Data. 14 (4), 170032.

Markuerkiaga, I., et al., 2016. A cortical vascular model for examining the specificity of the laminar BOLD signal. NeuroImage. 132, 491–498.

Miller, K.L., Jezzard, P., 2008. Modeling SSFP functional MRI contrast in the brain. Magn. Reson. Med. 60, 661–673.

Miller, K.L., 2012. FMRI using balanced steady-state free precession (SSFP). NeuroImage 62, 713–719.

Murphy, K., et al., 2013. Resting-state fMRI confounds and cleanup. Neuroimage. 80, 349-59.

Pathak, A.P., et. al., 2008. A novel technique for modeling susceptibility-based contrast mechanisms for arbitrary microvascular geometries: The finite perturber method. NeuroImage. 40, 1130–1143.

Ocali, O., Atalar, E., 1998. Ultimate intrinsic signal-to-noise ratio in MRI. Magn Reson Med. 39, 462-73.

Paulson, O.B., et al., 1977. Filtration and diffusion of water across the blood-brain barrier in man. Microvasc Res. 13(1), 113-24.

Pohmann, R., et al., 2016. Signal-to-noise ratio and MR tissue parameters in human brain imaging at 3, 7, and 9.4 tesla using current receive coil arrays. Magn Reson Med. 75 (2), 801-9.

Scheffler, K., et al., 2001. Detection of BOLD changes by means of frequency-sensitive TrueFISP technique: preliminary results. NMR Biomed. 14, 1-7.

Scheffler, K., Ehses, P., 2015. High-resolution mapping of neuronal activation with balanced SSFP at 9.4 tesla, Magn. Reson. Med. 76, 163-171.

Scheffler, K., Ehses, P., 2015. High-resolution functional imaging in the human brain using passband bSSFP at 9.4T. Proc 23th ISMRM, Toronto, 2076.

Schmid, F., et al., 2017. Depth-dependent flow and pressure characteristics in cortical microvascular networks. PLoS Comput Biol. 13(2): e1005392.

Sekihara K., 1987. Steady-state magnetizations in rapid NMR imaging using small flip angles and short repetition intervals. IEEE Trans Med Imaging 6, 157–164.

Silvennoinen, M.J., et al., 2003. Comparison of the dependence of blood R2 and R2* on oxygen saturation at 1.5 and 4.7 Tesla. Magn Reson Med 49, 47–60.

Smith, S.M., et al., 2004. Advances in functional and structural MR image analysis and implementation as FSL. NeuroImage. 23 (1), S208–19.

Spees, W.M., et al., 2001. MR properties of human blood at 1.5 Tesla. T1, T2, T2* and Gaussian relaxation behavior. Magn. Reson. Med. 45, 533–542.

Uludağ, K., et al., 2009. An integrative model for neuronal activityinduced signal changes for gradient and spin echo functional imaging. NeuroImage 48 (1), 150–165.

Vovenko, E., 1999. Distribution of oxygen tension on the surface of arterioles, capillaries and venules of brain cortex and in tissue in normoxia: an experimental study on rats. Pflugers Arch. 437 (4), 617-23.

Weber, B., et al., 2008. The microvascular system of the striate and extrastriate visual cortex of the macaque. Cereb Cortex. 18 (10), 2318-30

Weisskoff, R., et al., 1994. Microscopic susceptibility variation and transverse relaxation: Theory and experiment. Magn. Reson. Med. 31, 601–610.

Wiesinger, F., et. al., 2004. Electrodynamics and Ultimate SNR in Parallel MR Imaging Magn Reson Med. 52, 376 –390.

Appendix 2

Disentangling the layer-specific BOLD signal change: a hemodynamic PSF simulation in a realistic neurovascular network

Mario Gilberto Báez-Yáñez [1, 2*], Philbert S. Tsai[3], David Kleinfeld[3, 4] and Klaus Scheffler[1, 5]

[1]Department of High-Field Magnetic Resonance, Max Planck Institute for Biological Cybernetics, Tübingen, Germany.

[2]Graduate Training Centre of Neuroscience, University of Tübingen, Tübingen, Germany.

[3]Department of Physics, University of California at San Diego, La Jolla, CA, USA.

[4]Section of Neurobiology, University of California, La Jolla, CA, USA.

[5]Department of Biomedical Magnetic Resonance, University of Tübingen, Tübingen, Germany.

[*]Correspondence to:

Mario G. Báez-Yáñez

MPI for biological Cybernetics

Max Plank Ring 11

72076 Tübingen, Germany

mario.baez@tuebingen.mpg.de

Keywords:
Vascular cortical network
Arteries/veins and capillaries
Layer-specific BOLD fMRI
Orientation-dependent BOLD fMRI
Extravascular contribution
Balanced SSFP
Monte-Carlo simulation
Gradient Echo
Spin Echo
Hemodynamic point spread function

INTRODUCTION

High-resolution functional neuroimaging at ultra-high magnetic fields (≥7 Tesla) is a prominent imaging technique due to the increased spatial resolution to map the brain activity [Siero et al 2013, Fracasso et al 2018, Scheffler et al 2015, Yu et al 2014]. Besides, the implementation of high-resolution fMRI at ultra-high magnetic fields presents the advantage of an increased signal-to-noise (SNR) ratio in contrast to low magnetic fields, moreover, an enlarged contribution from different tissues to signal formation as well as a diminished intravascular contribution (given by the short T2 transverse relaxation time of the deoxygenated blood) [Pohmann et al 2014, Uludag et al 2009, Goa et al 2014].

In particular, in order to investigate the neural computations through the BOLD signal, it is necessary to resolve the laminar-specific vascular contribution within the cortical depth. The laminar-specific activation pattern relies on the features of the neurovascular network and the intrinsic hemodynamic changes [Petridou et al 2017]. Further, the impact of the magnetic field strength and the specificity of the pulse sequence needs to be properly characterized in order to maximize the BOLD contrast [Kim et al 2012].

Recently, experimental results have reported that laminar-specific BOLD signal shows an intensity dependence on the distance with respect to the cortical surface across the neocortex depth. These results indicate that large BOLD signal change is expected from neural activations near to the cortical surface [Siero et al 2011]. This BOLD signal dependency might be explained by the nature of the vessel network as well as the hemodynamic point spread function, although it is still under investigation by the use of different approaches [Heinzle et al 2016, Puckett et al 2016].

In this sense, the functional MR signal formation has been studied by non-realistic neurovascular approximations. Based on randomly distributed and oriented cylinders, signal attenuation has been well characterized by specific biophysical variables and pulse sequence parameters such as: vessel size, diffusion of molecules, volume fraction, susceptibility differences induced by oxygenation

changes in blood, echo time, repetition time, etcetera [Weisskoff et al 1994, Kiselev et al 1999, Boxerman et al 1995].

However, in order to interpret the laminar-specific BOLD signal acquired with high-resolution fMRI at ultra-high magnetic fields, it is essential to disentangle the specific vascular contribution to the BOLD contrast in realistic neurovascular geometries. [Gagnon et al 2015, Baez et al 2017, Markuerkiaga et al 2016].

The purpose of this work is to resolve the laminar-specific tissue contribution assuming a hemodynamic point spread function (PSF) in a realistic neurovascular network [Blinder et al 2013]. To achieve this goal, we investigated by means of Monte Carlo simulations, the independent functional MR signal contribution of macrovessels (vessels larger than 5 μm in diameter) and microvessels (vessels smaller than 5 μm in diameter) assuming a hemodynamic response. Likewise, we analyzed the impact of pulse sequence parameters and the magnetic field strength.

First, we calculated the impact on the BOLD contrast for a homogeneous oxygenated (active) and deoxygenated (resting) state condition across the cortical depth, for optimized BOLD parameters of a gradient echo (GE), spin echo (SE) and passband balanced steady-state free precession (bSSFP) pulse sequences, at different magnetic field strengths (from 1.5 to 16.4 Tesla).

Second, in order to characterize the specificity of the neural activation, and thus the neurovascular blurring to the BOLD signal change towards to the cortical surface, we examined the hemodynamic PSF tissue response (macrovesels and microvessels independently) for optimized BOLD parameters of GE, SE and passband bSSFP sequences at 9.4 Tesla.

Overall, our results demonstrate that the BOLD signal is dependent on pulse sequence, acquisition parameters and magnetic field strength. In addition, the laminar-specific activation is blurred by tissue contribution originated by macrovessels, although their effect can possibly be reduced by pulse sequences that are selective to microvascular contributions such as SE and bSSFP.

METHODS

We used four vascular networks from the parietal cortex of mice obtained by two-photon laser imaging techniques [Blinder et al 2013, Gould 2017]. All datasets contained vectorized information, i.e. the spatial distribution of the vasculature and the characteristic vessel radius at each specific coordinate, from the cortical surface to the white matter.

In order to analyze the laminar-specific contribution to BOLD signal changes, all four datasets were divided into six equidistant layers from the cortical surface to the white matter. Subsequently, we separated the vascular tissue into macrovessels and microvessels based on a threshold of the vessel radius.

According to [Weber 2008], macrovessels were defined as vessels larger than 5 μm in diameter and microvessels smaller than 5 μm in diameter. In several publications [Gagnon et al 2015, Markuerkiaga et al 2016], the pial vessels are not included in the vascular model. However, their influence on the BOLD signal is accounted in this work. Pial vessels were considered as vascular tissue with a vessel radius larger than 22 μm. Figure 1 shows a rendered model of two representative vascular networks. Each model has approximately a total volume of 1056x1000x1092 μm^3 and the resolution of the acquisition was 1 μm^3.

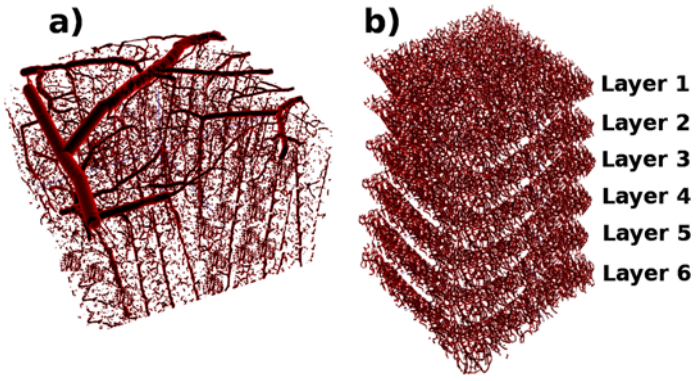

Figure 1. a) Macrovessels and b) microvessels simulation models obtained from the parietal cortex of mice by two-photon imaging techniques. The size of each layer is

1056x1000x182 μm^3 with a spatial resolution of 1 μm^3. The vessel walls were considered to be impermeable to diffusion of spins and Neumann boundary conditions were assumed. The layer division was calculated by an equidistant division from the cortical surface to the white matter and it did not represent any histological features. In the macrovascular model is possible to observed the penetrating arteries and ascending veins with the pial vessels in the surface of the neocortex.

Due to the sensibility of the MR signal to mesoscopic structure, we analyzed basic features of the vascular network such as 1) the volume fraction occupied by macrovessels and microvessels, 2) the vessel radius distribution and 3) the angular orientation of segments of vessels with respect to a vector normal to the cortical surface.

To estimate the volume fraction, we tracked every segment of the vessels by the use of simple vector analysis. An in-house developed algorithm identified for each spatial coordinate, the nearest neighbor segment of vessel (defined by the minimum length vector) between a given coordinate A and coordinate B. For each spatial coordinate, the vessel radius was known and thus an approximation of the volume occupied by a cylindrical shape with length of the nearest calculated vector was straightforward (volume = $\pi \cdot \mathrm{radius}^2 \cdot |\overrightarrow{\mathrm{AB}}|$).

In this sense, the angular orientation was calculated for every segment of vessel $\overrightarrow{\mathrm{AB}}$ with respect to an orthogonal vector placed on the cortical surface. The orientation was obtained by the dot product of these two vectors, i.e. normal vector to the cortical surface and the vessel segment vector $\overrightarrow{\mathrm{AB}}$.

In order to calculated the BOLD signal change assuming biophysical variables, such as susceptibility differences and thermal motion, Monte Carlo method is a powerful numerical tool to approximate MR signal evolution. For this purpose, the BOLD signal change, defined as the difference produced by the active and the resting state

$(\mathrm{BOLD} = (\mathrm{Act} - \mathrm{Rest}) * 100)$, was simulated for gradient echo (GE), spin echo (SE) and passband balanced steady-state free precession (bSSFP) pulse sequences. The simulation was implemented in Matlab (MathWorks, Natick, MA) and C/C++ using 128 cores in parallel computation to accelerate the calculation time.

For GE and SE, we followed the same procedure as Weisskoff and Boxerman to obtain the signal decay [Weisskoff et al 1994; Boxerman et al 1995]. Briefly, this method averages the phase accumulated for an ensemble of spins in thermal motion for a certain echo time (TE).

To compute the signal behavior of the bSSFP spin magnetization, the matrix representation of the Bloch equation was solved in accordance to the methods described by [Bieri et al 2007]. In sum, the bSSFP sequence was schemed as an excitation pulse (rotation in x- or y- plane), dephasing due to the spatial inhomogeneity contribution (rotation in z-plane) and thermodynamic intrinsic relaxation (T1 and T2 relaxation). The magnetization was prepared by a flip angle excitation (alpha) with an increment of 1 degree until the desired flip angle was reached. In addition, we used 180° phase cycling for each RF pulse ($\alpha_n = -\alpha_{n+1}$). The magnitude of the magnetization was acquired for an echo time equal to the half of the repetition time (TE = TR/2). All simulations were performed under on-resonance condition (passband region) and the simulation were run for several RF pulses until steady state of the signal was achieved.

To simulate the thermal motion, i.e. diffusion, an ensemble of spins were modeled as random walkers depicting motion across the voxel with a diffusion coefficient of $1\,{}^{\mu m^2}/_{ms}$. Isotropic diffusion was assumed. The vasculature network was considered to be impermeable (with Neumann boundary conditions) and only external diffusion in the medium was simulated. For all sequences, the magnetization of $3x10^6$ spins were averaged. The time resolution was set to 100 µs.

The susceptibility difference between vascular tissue and the surrounding medium was calculated according to $\Delta\chi = (0.273\ \mathrm{ppm} * \mathrm{Htc} * (1 - \mathrm{oxygenation\ level}))$,

where Htc is the hematocrit level. The Htc was set to 40 % [Yablonskiy et al 1994]. Furthermore, it was assumed that the volume fraction of the neurovascular tissue did not change for different functional states.

The relaxation times used for T1 and T2 of the extravascular compartment for different magnetic field strengths were obtained by the function $R1 = 0.003*B_0*B_0 - 0.0791*B_0 + 0.9247$ and $R2 = 1.74*B_0 + 7.77$ according to [Khajehim et al 2017].

Owing to the fact that intravascular influence at ultra-high magnetic field is diminished, the calculated BOLD signal change did not assume this contribution [Uludag et al 2009, Goa et al 2014].

Optimization of BOLD sequence parameters in a random cylinder model

The selection of sequence parameters is important to maximize the BOLD signal change. In accordance to this statement, we calculated for GE, SE and bSSFP, the optimal echo time dependent on the applied magnetic field strength for a randomly oriented cylinder model. The model was constructed by cylinders, randomly oriented with respect to B_0 and radius sizes ranging from 0.5 µm to 100 µm. The volume fraction was fixed to 2 %. The oxygenation level was set to 100 % and 80 % for active and resting state, respectively. The BOLD signal change was calculated as the averaged contribution of all cylinder calibers.

MR signal formation in a realistic neurovascular network

With regard to disentangle the contribution of neurovascular tissue, the BOLD signal changes were simulated for macrovessels and microvessels, independently. Optimized sequence parameters were assumed in order to analyze the tissue contribution across the cortical depth. The simulations were performed at 1.5, 3, 5, 7, 9.4, 10.1, 11.4, 14.1 and 16.4 Tesla for GE, SE and bSSFP. Furthermore, an orientational dependence vascular contribution was estimated at four different

orientation angles of the vascular model with respect to the B_0 (from 0° to 90° at intervals of 30°).

The simulated oxygenation value for active state was set to 100 % and for resting state to 80 %. The oxygenation level was homogeneously distributed across the cortical depth for both macrovascular and microvascular tissue.

Hemodynamic point spread function

Finally, a hemodynamic PSF was simulated as response to a specific cortical layer activation. For macrovessels, the oxygenation level was assumed as a half-Gaussian oxygen decay, with the maximum at the activated layer and a decreasing oxygenation towards to the cortical surface (see Figure 2). The FWHM was approximately 200 µm and the oxygenation level was decreasing from 70 % (activated layer) to 60 % (cortical surface) [Vasquez et al 2014].

In the case of microvascular tissue, only the active layer exhibited an oxygenation difference between states (active 85 %, resting 77 %); whereas the rest of the microvascular layers kept the same oxygenation level (77 %). For simplicity, the hemodynamic PSF was only simulated at 9.4 T for optimized parameters of GE, SE and bSSFP pulse sequences. In addition, the orientational dependence vascular contribution was estimated at four different orientation angles of the vascular model with respect to the B_0 (from 0° to 90° at intervals of 30°).

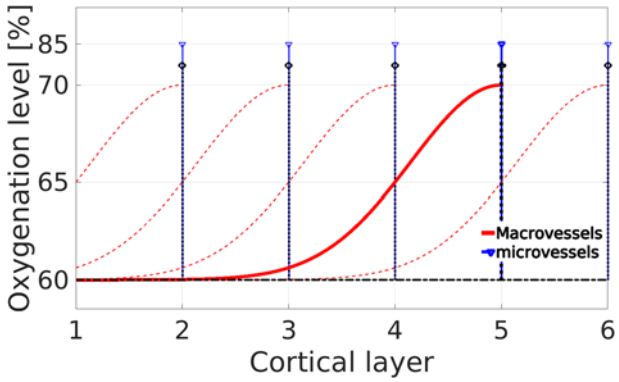

Figure 2. Oxygenation level distribution assumed by an activation in layer 5 (highlighted lines) for macrovessels and microvessels. Black dashed lines represent oxygenation level at resting state (macrovessels 60 %, microvessels 77 %). Dependent on the active cortical layer, the oxygenation curve is shifted across the cortical depth and maintains the same behavior (colored dashed lines).

RESULTS

Volume Fraction

Figure 3 shows the estimated volume fraction of the neurovascular models. The labels of the models (AU, CO, DB, AV) are arbitrary. The volume fraction indicates that tissue occupancy in our simulation models range from ~1 % to ~4 %. The resultant volume fraction is in agreement with previous studies [Tsai et al 2009] but reduced by a factor of approximately two.

It can be observed that the first layer presents an overweight of macrovessels. Pial vessels represent an important volume fraction contribution (~1.2 %). In contrast, the volume fraction given by macrovessels reduces from layer 2 to 6. Microvessels, on the other hand, are equally distributed across the cortical depth. However, the volume fraction rises slightly up in the granular layer (layer 3 and 4) and decreases slightly again in the supra (layer 1 and 2) and inferior layer (layer 5 and 6).

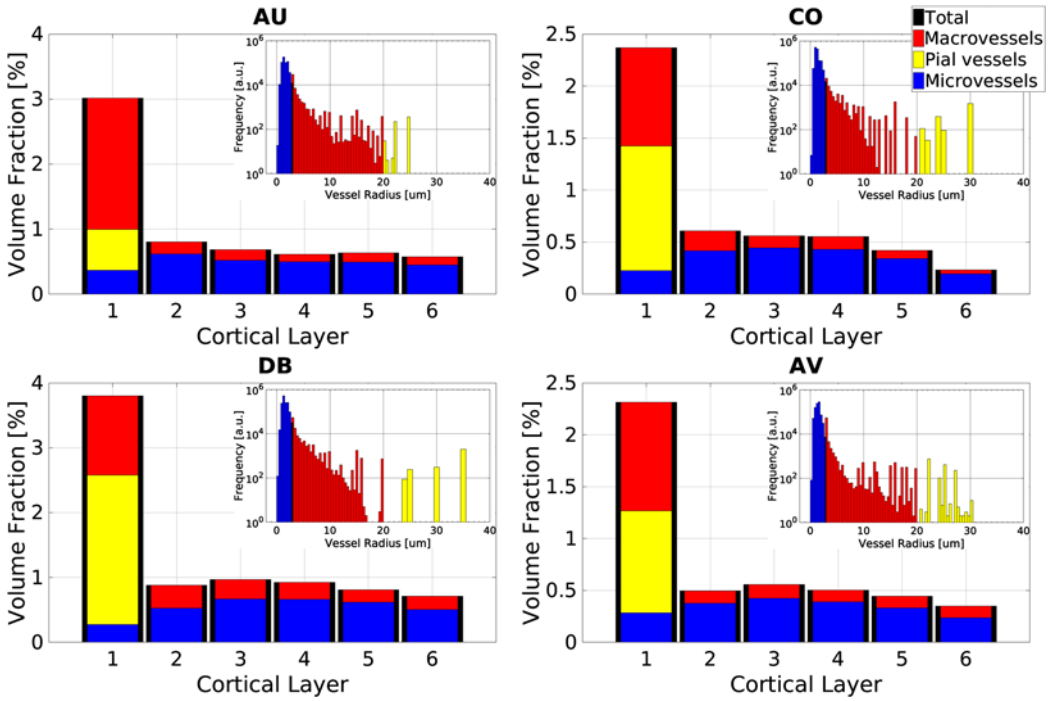

Figure 3. Volume fraction of macrovessels (red box) and microvessels (blue box). The yellow box represents the volume fraction given by the pial vessels. The distinction between vascular layer is calculated by an equidistant division of the cortical depth, and does not represent any histological features. All models reveal similar volume fraction, between ~1% to ~4% of the voxel is occupied by neurovascular tissue. The vessel radius distribution is shown on the upper right corner of each dataset. The vessel radius distribution of the models, in general, exhibits similar behavior although some slightly differences can be noticed.

Frequency distribution of vessel radius

Each dataset contains the particular vessel radius at every single spatial coordinate. The distribution of the vessel radius is shown in the upper right corner of each dataset in Figure 3. The vessel radius range is from about 0.5 μm to ~30 μm. Excluding a few variations, all models show a similar radius distribution. The most frequent vessel radius is found in the microvascular range (~2 μm). In the case of the radius from macrovascular tissue, a decreased frequency is observed for the biggest vessels.

Vascular Orientation Frequency

The orientation distribution was calculated as an average of all the neurovascular models. The distribution shown in Figure 4.a) represents the probability of appearance of vessel orientation. Figure 4.b) shows a polar distribution, where the polar radius represents the radius of the vessel and, the polar angle mimics the angular orientation of the vessel. In contrast to [Baez et al 2017], in this work the angular orientation is calculated for each laminar cortex independently.

Our results suggest a random orientation exhibited by the microvascular tissue, whereas the macrovascular orientation tends to display some preferences. For instance, layer 1 shows an expected increment in the orientation orthogonal to the B_0 (values between 70 and 90 degrees) because of the orientation of large pial vessels. Moreover, the increment near to a parallel orientation with respect to B_0 for layer 2 to 6 can be explained by the anatomy of the penetrating arteries and ascending veins.

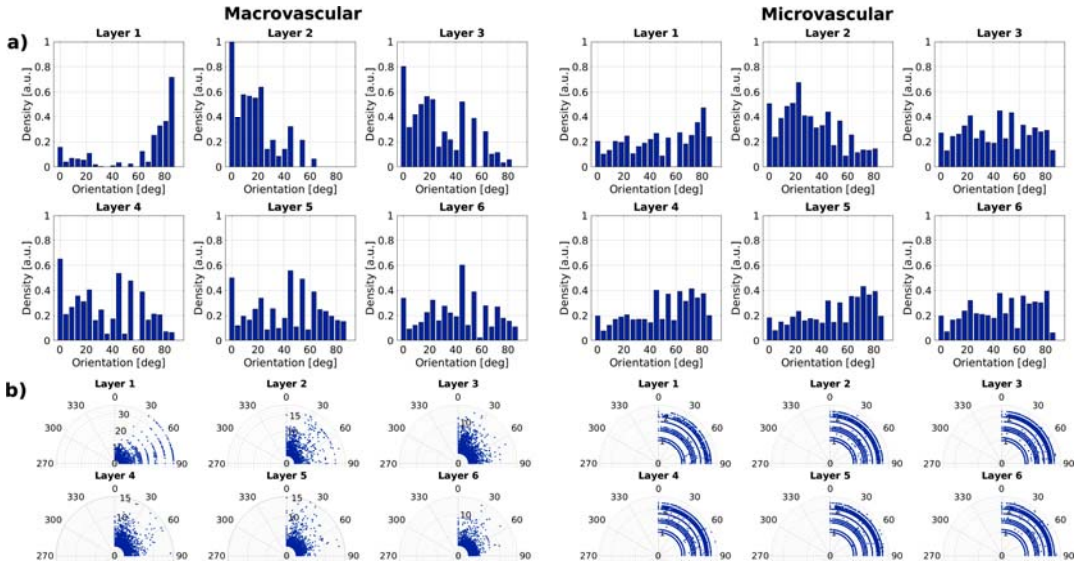

Figure 4. Average orientation distribution of macrovasculature and microvasculature from the simulation models. a) Orientational probability density. b) Polar density: the radius of the polar sample resembles the vessel radius, whereas the angle in the

polar plane is analogous to the displayed angle of the vascular tissue with respect to a vector normal to the surface of the cortex.

Optimization of BOLD sequence parameters in a random cylinder model

Based on a randomly distributed cylinder model, for different echo times and magnetic field strengths, Figure 5 shows the BOLD signal change calculated for GE, SE and bSSFP pulse sequences. Biophysical and pulse sequence parameters are described in Figure 5.

All sequences demonstrate that, the higher the magnetic field strength, the larger the BOLD signal change. However, the maximum BOLD signal change depends on the selected parameters of the pulse sequence. For GE, the optimal echo time is approximately at the same value of the T2 of tissue. Contrary, the optimal echo time for SE shows a factor of ~1.3 of the T2 relaxation time of tissue. bSSFP tends to exhibit a maximum BOLD signal change at higher magnetic fields and for larger repetition times.

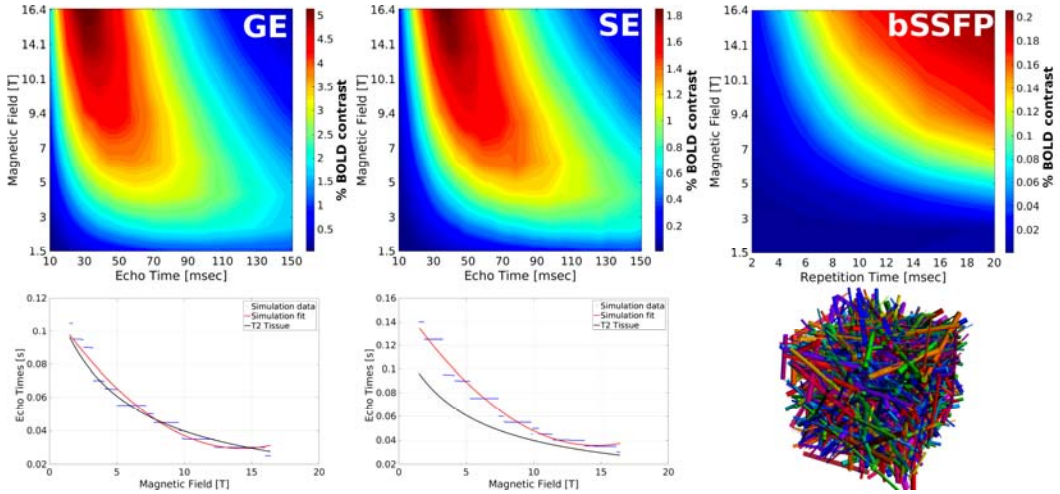

Figure 5. BOLD signal change obtained by a randomly distributed cylinder model (as depicted in the lower right corner) for different echo times and magnetic field strengths for GE, SE and bSSFP. The simulated echo time ranges from 10 ms to 150 ms for GE and SE. The simulated repetition time (TE = TR/2) for bSSFP ranges from 2 ms to 20 ms and a flip angle of 20 deg. The field strength ranges from 1.5 T

to 16.4 T. In order to calculate the BOLD signal change, an average of all cylinder caliber contributions was computed.

MR signal formation in a realistic neurovascular network

The BOLD signal change induced by the contribution of macrovascular and microvascular tissue for one representative vascular model assuming a homogeneous oxygenation level across the cortical depth is shown in Figure 6 for GE, SE and bSSFP at different magnetic field strengths, whereas Figure 7 displays the average contribution. In addition, the corresponding micro/macro ratio is calculated for all sequences and magnetic field strengths (Figure 7).

The macrovascular contribution is shown in red bars and the pial vessel contribution is shown in yellow bars, whereas the microvascular contribution is displayed in blue bars.

The impact of the magnetic field into the BOLD signal change is clearly visible for all sequences.

In general, GE demonstrates the largest BOLD signal change across all magnetic fields. This result is produced by the non-selectivity of GE to vessel calibers. GE BOLD signal change is observed to be higher by a factor of ~3 in comparison to SE. On the other hand, SE is less sensitive to BOLD signal changes, however, this sequence exhibits a selectivity to small vessel diameters as can be observed in the Figure 6 as an enlarged microvascular contribution and in Figure 7, where the ratio is better than GE and bSSFP.

Furthermore, bSSFP shows the lowest sensitivity to BOLD signal changes, dependent on the used pulse parameters ~20 times smaller than GE and ~4 smaller than SE, however, the exhibited micro/macro ratio is slightly better than GE for the bSSFP pulse sequence with a repetition time of 10 ms.

It is worth to note the enhanced contribution from the microvascular tissues at higher magnetic fields. The micro/macro ratio demonstrates a linear increment at higher magnetic field strengths for GE and SE. According to our results, bSSFP reveals a different behavior. At low magnetic field, the micro/macro ratio is dominant, whereas values above 5 Tesla present a linear increment toward higher magnetic fields.

In particular, GE and SE BOLD signal exhibit a dependence on the distance across the cortical depth. The BOLD signal change decreases towards to deeper layers due to the neurovascular features and signal contribution of macrovessels. In contrast, bSSFP does not show any dependence on the distance across the neocortex.

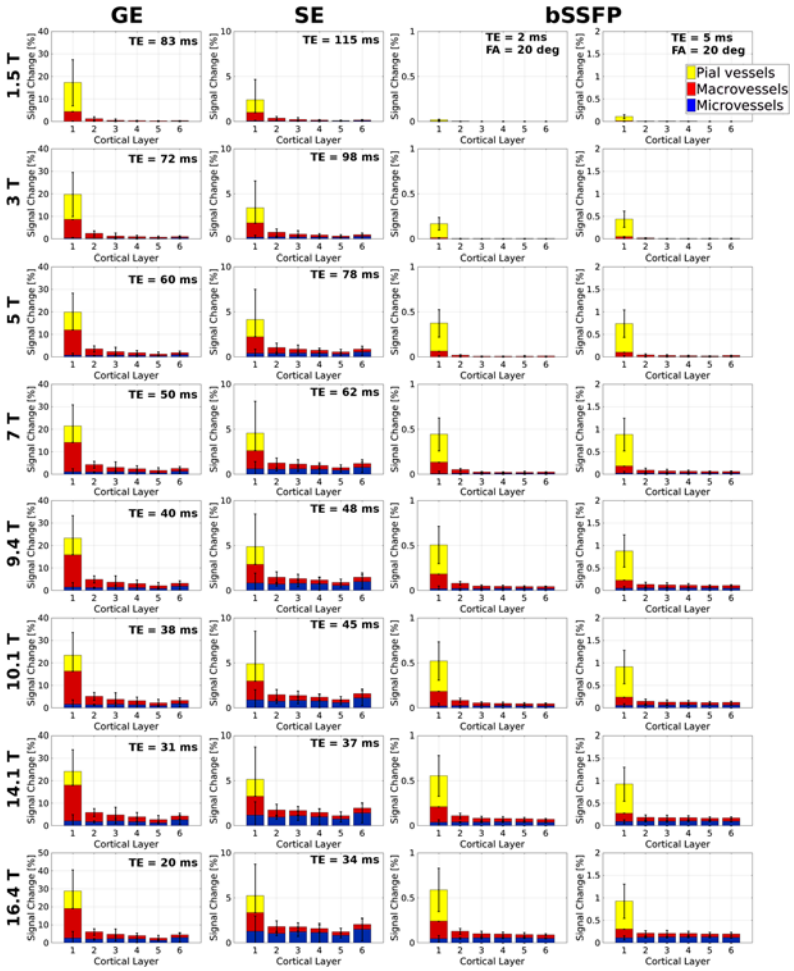

Figure 6. Average BOLD signal change calculated by the orientational contribution from macrovascular and microvascular tissue across the cortical depth. Simulations

were performed by GE, SE and bSSFP and for different magnetic field strengths. The used echo times were optimized for GE and SE. The repetition time used for bSSFP was 10 ms and the echo time 5 ms. The flip angle was optimized in order to maximize the intensity of the signal (flip angle of 20 deg). The oxygenation levels were homogeneously distributed across cortical depth, with 100 % in active and 80 % at resting state.

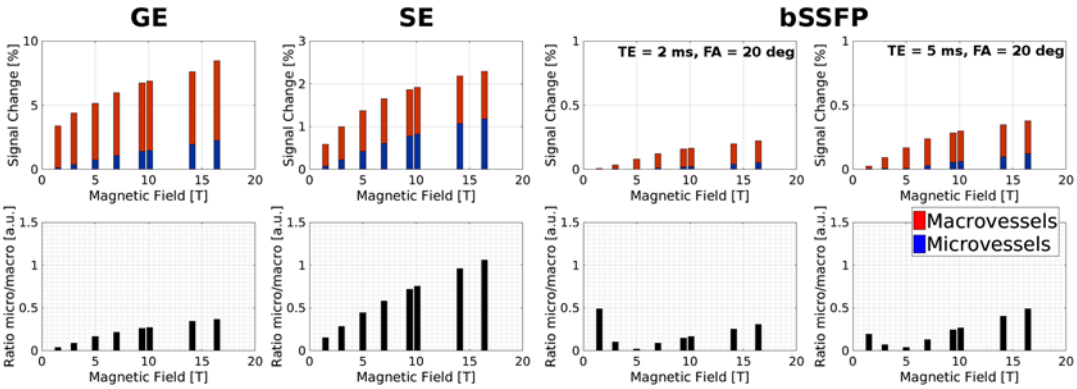

Figure 7. Average contribution from microvascular and macrovascular tissues across the cortical depth for different magnetic field strengths and different pulse sequences (GE, SE and bSSFP). The used echo times were optimized based on the cylinder model described above. Moreover, the micro/macro ratio is depicted for all sequences and magnetic field strengths. The micro/macro ratio gives a parameter to evaluate the contribution of microvascular tissues and the selectivity to vessel caliber performed by the pulse sequence.

Hemodynamic point spread function

In Figure 8, the average orientational contribution of macrovessels and microvessels is depicted for different layer-specific activations (from layer 2 to 6) at 9.4 Tesla. The error bar shows the standard deviation of the angular dependence with respect to the magnetic field. To determine the oxygenation level in each layer, we assumed the oxygenation distribution shown in Figure 2. Owing to the diverse level of oxygenation used across the cortical depth, the relative BOLD signal change is better

suited to represent the differences calculated by the two functional states: $relative\ \mathrm{BOLD} = \frac{(\mathrm{Act}-\mathrm{Rest})}{Rest} * 100.$

The relative BOLD signal change calculated by GE shows the largest sensitivity. It is larger by a factor of ~5 compared with SE and a factor of ~10 in contrast to bSSFP. On the other hand, SE shows larger sensitivity to oxygen changes by a factor of ~4 than bSSFP. In addition, GE shows a stronger dependence on the angular orientation than SE and bSSFP. Moreover, the micro/macro ratio demonstrates that SE exhibits the larger sensitivity, followed by bSSFP. As expected, due to the non-selectivity features of the pulse sequence, GE shows the lowest micro/macro ratio.

Our results suggest that, the relative BOLD signal change for GE decreases slightly towards to deeper layers. In contrast, SE and bSSFP present the same amplitude for the activated layer across the cortical depth. Surprisingly for all sequences, the layer 1 still contributes significantly to the relative BOLD signal change.

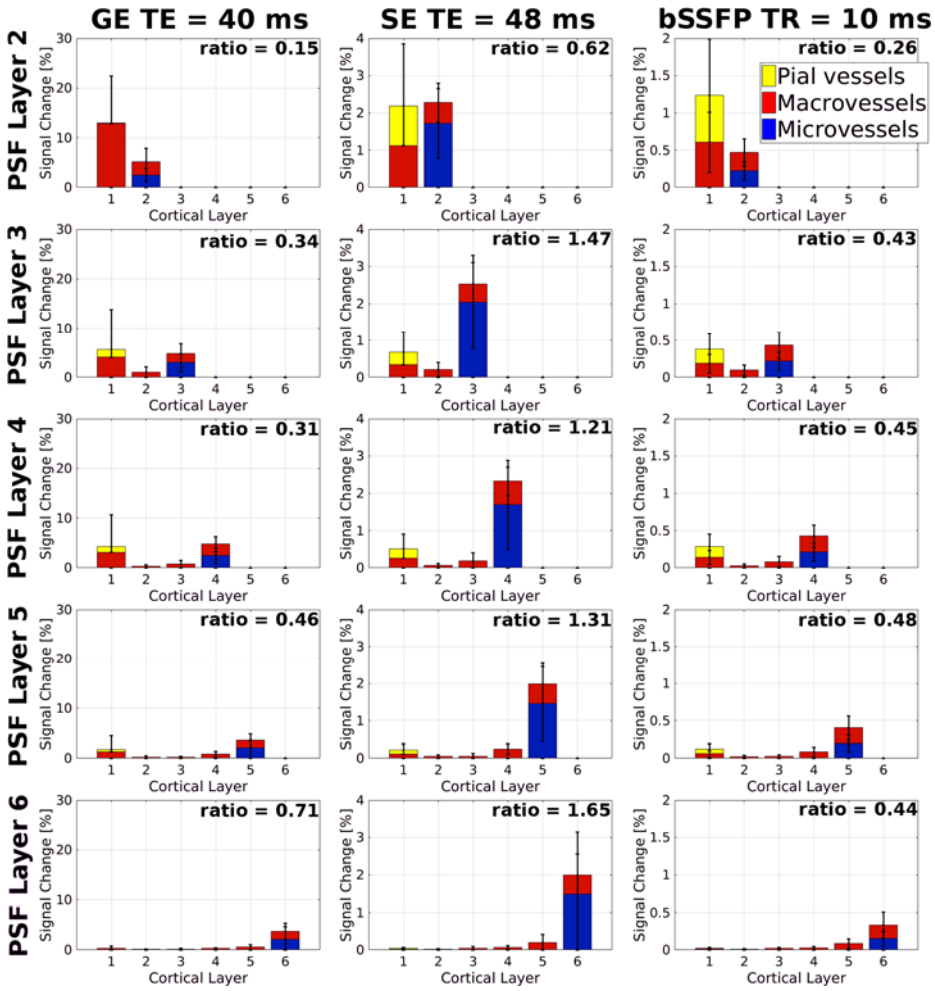

Figure 8. Tissue contribution of the BOLD response across layers produced by a neural activation of a specific layer based on the oxygenation distribution showed in Figure 2 for GE, SE and bSSFP at 9.4T. Each bar represents the averaged angular contribution –with its respective standard deviation- from the relative BOLD signal calculated at different orientations with respect to the magnetic field. For GE, we used a TE = 40 ms, for SE a TE = 48 ms and for bSSFP a flip angle = 20 deg, TR = 10 ms and TE = 5 ms.

DISCUSSION

In accordance to the presented results, the BOLD signal formation is the result of complex interactions of different tissues and particular biophysical characteristics, as

well as hemodynamic responses that influence the magnetization of spins. Additionally, the overall pulse sequence parameters and magnetic field strength have a high impact on the MR signal behavior.

Volume Fraction

As reported in many studies before, the volume fraction occupied by the neurovascular tissue is around 3% to 5% across the cortical depth. Our results show a similar behavior across the cortical depth as reported in other investigations, but a volume fraction that is reduced by a factor of approximately 2 - 2.5 [Weber et al 2008, Tsai et al 2009]. In accordance to the linearity of the BOLD signal with respect to the volume fraction, the calculated BOLD signal changes will be enlarged by this factor.

The volume fraction of macrovessels is dramatically reduced as function of cortical depth. The highest volume fraction for macrovessels is observed in the supracortical layer (layer 1) and a minimal volume fraction in the granular and inferior regions (from layer 2 to 6). One of the reasons of the high volume fraction exhibited by the first layer is due to the pial arteries and veins that supply and drain blood from the brain [Schmid et al 2017].

Moreover, our results indicate that the volume fraction of the microvessels tends to be uniform across the cortical depth. In contrast to the supra (1 and 2) and infra (5 and 6) layers, a slightly larger volume is shown in the granular layer 3 and 4 from the model DB, CO and AV. This result demonstrates the heterogeneity of the microvascular tissue across the cortical depth. However, this behavior is not presented in the AU model. Some details about the difference in the model AU are mention in [Gould 2017].

Frequency distribution of vessel radius

All the models present a similar distribution of the radius size. The most frequent vessel radius in the model is found in the microvascular range (~2 μm) related by the large volume fraction of microvasculature across the neocortex. Furthermore, a decreased frequency behavior is schemed for larger vessel radius.

The MR signal is sensible to the vessel caliber. In this sense, the BOLD signal shows an enlarged or reduced contribution from different vessels dependent on the pulse sequence. In general, GE is known for its non-selectivity and its high sensitivity to all calibers of vessels. In contrast, SE shows a more selective contribution for small vessels [Boxerman et al 1995]. Balanced SSFP acts as a SE-like behavior, dependent on the parameters of the pulse sequence, and thus shows a similar selectivity for microvascular tissues [Scheffler 2003, Bieri 2007, Baez et al 2017, Khajehim et al 2017]. Nevertheless, the selectivity of SE and bSSFP depends on biophysical characterisitcs, i.e. susceptibility created by the de-oxyhemoglobin state, thermal motion and the magnetic field strength.

Vascular Orientation Frequency

Our results suggest a pseudo-random orientation behavior for the microvascular tissue, whereas the macrovascular orientation tends to display some angular preferences. For instance, the layer 1 shows an expected increment in the orientation orthogonal to the B_0 (values between 70 and 90 degrees) because of the large pial vessels. In addition, the increment on the angular density close to the parallel orientation with respect to B_0 for layer 2 to 6 can be explained by the anatomy of the penetrating arteries and ascending veins.

Optimization of echo time in a random cylinder model

Most of the fMRI acquisitions are obtained with GE and SE. In order to maximize the BOLD contrast, it is well accepted to choose an echo time that approximates the value of T2 of tissue. Nevertheless, our results suggest that this statement is only valid for GE. On the other hand, the optimal echo time for SE deviate from the T2 of the tissue and is increased by a factor of ~1.3.

This might be explained by the inherent selectivity to certain vessel calibers of the sequence, i.e. smaller vessel radius need larger echo times compared to the T2 of tissue, in order to increase their impact on the BOLD signal. This result also demonstrates the high sensibility of the BOLD signal to biophysical properties. It is

worth to note, that this factor is also dependent on the specific levels of oxygenation and volume fraction.

MR signal formation in a microvascular and macrovascular simulation model

In general, GE shows the largest BOLD signal change for all field strengths. The GE BOLD signal change is approximately ~3 times larger than SE and ~20 times more than bSSFP. Likewise, SE shows a ~4 times larger sensitivity than bSSFP according to the averaged results.

The micro/macro ratio is a good parameter to compare the selectivity of the sequences and the enhancement of microvascular contribution. In this sense, GE shows the smallest sensitivity of contribution from microvessels. Besides, SE shows the largest ratio as consequence of the influence of the refocusing pulse that attenuate or completely eliminate the contribution from macrovessels.

On the other hand, bSSFP presents a tendency to be selective due to its T2-like behavior but this selectivity has a strong dependence on the parameters of the pulse sequence as previously demonstrated by [Baez et al 2017] and [Khajehim et al 2017].

In particular, the BOLD signal change from different layers demonstrates that the largest BOLD signal, independent of the field strength, is produced by the layer 1, as consequence of the large volume fraction exhibited in this cortical region from macrovascular tissue, especially the pial vessel contribution. From layer 2 to 6, the contribution of the microvascular and macrovascular tissue is more evenly distributed for GE and bSSFP, whereas SE shows an increased contribution of microvascular tissue.

It can be noted, that the BOLD signal for GE and SE increases slightly towards to the cortical surface. On the other hand, with exception of the layer 1, bSSFP displays a more constant behavior across layers. This behavior might be resulting from the steady-state signal behavior *per se,* or the high SNR offered by the pulse sequence [Bieri et al 2013].

The BOLD signal change pattern as a function of cortical depth shown in Figure 6 reveals the same behavior of experimental data acquired by [Chen et al 2013, Fig.4.c] in the visual cortex of awake monkey. In that study, only GE was performed. Furthermore, our results are also comparable with experimental data acquired with SE approaches in humans [Goense et al 2016].

Hemodynamic point spread function in a real vasculature

The tissue contribution of each layer is directly correlated with its inherent volume fraction (Figure 3) and the oxygenation level (Figure 2). Relative BOLD signal changes in GE sequence are, in general, about five times larger compared to SE and ten times bigger compared to bSSFP. The BOLD signal change decreases as function of cortical depth for GE and SE. Towards to deeper layers, the contribution of macrovessels is reduced.

On the other hand, close to the cortical surface, the specificity of the BOLD signal is blurred by contribution from macrovessels for all acquisition sequences. This behavior is more dominant in the GE scheme. In contrast, the contribution from macrovessels in bSSFP and SE is reduced but not completely eliminated, owing to the refocusing pulse effect. Experimental data acquired with GE and SE demonstrate the same behavior of decreased BOLD signal as function of the cortical depth, but SE shows a larger selectivity to smaller vessel radius [Puckett et al 2016, Goense et al 2016].

Overall our results are comparable with those published by [Markuerkiaga et al 2016], due to the similarities in the vascular and hemodynamic PSF assumptions. In contrast with the results obtained by [Markuerkiaga et al 2016], we show that towards to the cortical surface, the contribution of large vessels is not eliminated in the SE acquisition and thus gives an influence on the specificity of the activation. In addition, the obtained results in that publication show a small difference between GE and SE in the BOLD signal change (a factor less than one). Contrary to our results that suggest a factor of two in the activated layer for GE in comparison to SE.

As it is already known, the orientation with respect to the main magnetic field modifies the signal intensity and thus produces an angular BOLD signal dependence [Gagnon et al 2015, Baez et al 2017, Fracasso et al 2018]. The maximal contribution arises from vascular tissues that are orthogonal to the magnetic field. Moreover, because of the uniform distribution of the microvascular, the angular BOLD signal dependence might only be explained by the contribution from macrovessels.

For SE and bSSFP pulse sequences, that exhibit a selectivity behavior for small vessel calibers, this angular dependence is attenuated but not completely eliminated. In contrast, GE is highly dependent on the orientation of the vascular tissue.

CONCLUSION

Characterizing the dynamical process of mesoscopic structures, such as vascular dilatation and temporal oxygenation levels, into measurable BOLD signal is an important step towards to a physiological interpretation of neural activation maps and a general understanding of the neurovascular response in an fMRI experiment. Modelling the BOLD signal over real vasculature data represents a significant improvement over the classical models based on infinitely cylindrical shapes. Moreover, modelling the MR signal opens the possibility to go beyond the actual laminar-specific contributors and decompose the fingerprint of the mesoscopic structure contained in an image voxel.

ACKNOWLEDGEMENT

Mario Gilberto Báez-Yáñez is thankful for the support given by CONACYT (Consejo Nacional de Ciencia y Tecnología, México) and the fruitful discussion and comments from Silke Pitschak, Daniel Zaldivar, Rahel Heule and Anagha Deshmane. We also thank the NIH-NINDS (grant R35NS097265) and the NIH-NIMH (1R01MH111438) for funding.

REFERENCES

Báez-Yáñez MG et al, The impact of vessel size, orientation and intravascular contribution on the neurovascular fingerprint of BOLD bSSFP fMRI, NeuroImage (2017) 163:13-23

Bieri O Scheffler K. Effect of diffusion in inhomogeneous magnetic fields on balanced steady state free precession. NMR Biomed (2007) 20:1-10

Bieri O, Scheffler K. Fundamentals of balanced steady state free precession MRI. J Magn Reson Imaging (2013) 38:2-11

Blinder P et al, The cortical angiome: an interconnected vascular network with noncolumnar patterns of blood flow. Nature Neurosci (2013) 16:889-897

Boxerman J et al. MR contrast due to intravascular magnetic susceptibility perturbations. Magn Reson Med (1995) 34:555-566

Chen et al. Layer-specific BOLD activation in awake monkey V1 revealed by ultra-high spatial resolution functional magnetic resonance imaging. Neuroimage (2013) 64:147-155

Fracasso A et al, Laminar imaging of positive and negative BOLD in human visual cortex at 7T, Neuroimage (2018) 164: 100-111

Gagnon L. et al, Quantifying the microvascular origin of BOLD fMRI from first principles with two-photon microscopy and an oxygen-sensitive nanoprobe, J Neurosci (2015) 35:3663-3675

Goa P et al. BOLD fMRI signal characteristics of S1- and S2- SSFP at 7 Tesla. Front in Neurosc (2014) 49:1-6

Goense J et al. fMRI at high spatial resolution: implications for BOLD models. Front Comput Neurosci (2016) 10:66

Gould IG et al. The capillary bed offers the largest hemodynamic resistane to the cortical blood supply. J Cereb Blood F&Met (2017) 37:52-68

Heinzle J et al. A hemodynamic model for layered BOLD signals. NeuroImage (2016) 125: 556-570

Khajehim et al. Investigating the spatial specificity of S2-SSFP fMRI: A Monte Carlo simulation approach. Magn Reson Im (2017) 37:282-289

Kim SG, Ogawa S. Biophysical and physiological origins of blood oxygenation level-dependent fMRI signal. J Cer Blo Flo Met (2012) 32;1188-1206

Kiselev V. Posse S. Analytical model of susceptibility induced MR signal dephasing: effect of diffusion in a microvascular network. Magn Reson Med (1999) 41:499-509

Markuerkiaga I et al. A cortical vascular model for examining the specificity of the laminar BOLD signal. NeuroImage (2016) 132:491-498

Petridou N, Siero J. Laminar fMRI: what can the time domain tell us?. NeuroImage (2017) 164:100-111

Puckett AM et al. The spatiotemporal hemodynamic response function for depth-dependent functional imaging of human cortex. NeuroImage (2016) 139:240-248

Scheffler K, Ehses P. High-resolution mapping of neuronal activation with balanced SSFP at 9.4 Tesla. Magn Reson Med (2015) 76:1522-2594

Scheffler K, Henning J. Is TrueFISP a Gradient-Echo or a Spin-Echo Sequence?, Magn Reson Med (2003) 49:395-397

Scheffler K, Lehnhardt S. Principles and applications of balanced SSFP techniques. Eur Radiol (2003) 13:2409-2418

Schmid F et al. Depth-dependent flow and pressure characteristics in cortical microvascular networks. PLOS Comp Biol (2017) 1-22

Siero J et al. Cortical depth-dependent temporal dynamics of the BOLD response in the human brain. J Cer Blo Flo Met (2011) 31:1999-2008

Tsai PS et al. Correlations of neuronal and microvascular densities in murine cortex revealed by direct counting and colocalization of nuclei and vessels. J Neuroscie (2009) 29:14553-14570

Uludag K et al. An integrative model for neuronal activity induced signal changes for gradient and spin echo functional imaging. NeuroImage (2009) 48:150-165

Vazquez AL et al. Neuronal and hemodynamic response elicited by forelimb and photostimulation in channelrhodopsin-2 mice: insights into the hemodynamic point spread function. Cer Cor (2014) 24:2908-2919

Weber B et al. The microvascular system of the striate and extricate visual cortex of the macaque. Cereb Cortex (2008) 10:1093

Weisskoff RM et al. Microscopic susceptibility variation and transverse relaxation: theory and experiment. Magn Reson Med (1994) 31:601-610

Yablonskiy D, Haacke M. Theory of NMR signal behavior in magnetically inhomogeneous tissues: the static dephasing regime. Magn Reson Med (1994) 32:1522-2594

Yu X et al. Deciphering laminar-specific neural inputs with line-scanning fMRI. Nature Methods (2014) 11, 55–58

Appendix 3

The BOLD sensitivity of rapid steady state sequences

Klaus Scheffler[1,2], Rahel Heule[1], Mario Gilberto Báez-Yánez [1,3], Bernd Kardatzki[2], Gabriele Lohmann[1,2]

[1]High-Field MR Center, Max Planck Institute for Biological Cybernetics, Tübingen, Germany

[2]Department for Biomedical Magnetic Resonance, University of Tübingen, Tübingen, Germany

[3]Graduate Training Centre of Neuroscience, University of Tuebingen, Tuebingen, Germany

Introduction

Most functional BOLD imaging experiments are acquired with gradient echo (GE) sequences in combination with an echo planar imaging (EPI) readout. In some studies, also spin echo (SE) based EPI sequences have been used (Constable, Poser, Chamberlain, Bandettini, Feinberg, Yacoub) as these techniques are less sensitive to BOLD contributions from larger vessels (Ogawa, Weisskoff, Boxerman). As an alternative to GE and SE, balanced steady state free precession (SSFP) and S2-SSFP (the non-balanced SSFP echo before the RF pulse) have been proposed and analyzed for BOLD imaging (Barth, Goa, Khajehim, Scheffler, Miller, Ehses, Scheffler). In a recent paper iSSFP has been introduced for BOLD imaging at 7T, but these sequences are identical to S1-SSFP and S2-SSFP (Sun). One major advantage of rapid SSFP sequences over EPI-based sequences is their lack of any spatial distortions along phase encode direction, which makes registration to anatomical images straightforward. This is especially important for sub millimeter resolution acquisitions that aim to disentangle signals from different cortical layers or columns.

The BOLD sensitivity of different sequences to the underlying neurovascular vessel size is a further key feature to characterize the measured BOLD signal changes. The vessel size dependence of the BOLD effect is often divided into two regimes: the diffusion narrowing regime for small vessel sizes of up to about 5-10 µm radius, and the static dephasing regime for larger vessels (Weisskoff, Boxerman, Yablonskiy, Kiselev). In the static dephasing regime, dephasing effects around vessels are almost completely refocused for SE, but remain for GE and thus making them sensitive to larger vessels. Therefore, it is generally accepted that SE is more sensitive to oxygenation changes located within microvessels and thus might be closer to the neuronal event compared to GE (Norris). Steady state sequences such as balanced SSFP (bSSFP) and non-balanced (gradient-spoiled) SSFP such as S2-SSFP generate echoes that are composed of contributions from different coherent pathways or gradient and spin echo configurations (Kaiser, Scheffler). Each configuration exhibits a different sensitivity to oxygenation changes and additionally might show different sensitivity to the vessel size.

In this contribution we present an analysis of the BOLD sensitivity of non-balanced and balanced SSFP across field strength as a function of vessel size for several different coherence pathways, including the F^{+}_{0} “gradient echo”, the F^{-}_{0} “S2-echo”, the balanced echo, and higher order coherences. All calculations are based on Monte Carlo simulations of randomly oriented cylinders across different vessels diameters, repetition times, flip angles, and field strength. In addition, experimental measurements on dispersed micro spheres of the F^{+}_{0} and F^{-}_{0} echo were performed to confirm the predicted dependence of these echo pathways on the radius of the measured spheres.

Methods

Monte Carlo simulations

The MR signal formation of the extravascular water proton magnetization exposed to an extended train of RF pulses during their random walk through the neurovascular network was modeled for artificial cylinders with different diameter and random orientation to B_0 according to Weisskoff, Bieri, Baez. The potential contribution of intravascular signals is discussed below. In all simulations, the steady state bSSFP signal profile was calculated at 32 different phase increments between –π and π, for different flip angles between 10° and 50°, different repetition times TR between 5ms and 45ms, and field strengths from 1T to 15T. Extravascular relaxation rates as a function of B_0 were calculated as $R1= 0.003*B_0*B_0 - 0.0791*B_0 + 0.9247$ and $R2= 1.74*B_0 + 7.77$, according to Uludag, Khajehim. As illustrated in Fig. 1, the resulting bSSFP signal profile after and before the RF pulse was then Fourier transformed to derive 32 different non-balanced SSFP coherence pathways ranging from F^{+}_{-15} to F^{+}_{16} (after RF pulse) and F^{-}_{-15} to F^{-}_{16} (before RF pulse). The signal profile for bSSFP at a phase increment of zero corresponds to the conventional pass-band bSSFP sequence (centered between RF pulses and with alternating excitation pulses), and converts to a stop-band experiment for phase of –π to π. The left panel in Fig. 1 shows echo amplitudes as a function of vessel radius for configurations F^{+}_{-15} to F^{+}_{16} generated immediately after RF pulse, where F^{+}_{0} corresponds to the conventional non RF-spoiled gradient echo signal (FISP, FAST, GRASS, FFE, S1-SSFP, which is not identical to the T_1-weighted RF-spoiled gradient echo). Refocused configurations that appear immediately before the next RF pulse are shown right in Fig. 1. They correspond to the F^{-}_{-15} to F^{-}_{16} pathways, where F^{-}_{0} is also called PSIF, CE-FAST, T2-FFE, or S2-SSFP signal. For simplicity, only the resting state using Y = 80% ($\Delta\chi$ of 0.022 ppm) was compared to the activated, fully oxygenated state with Y = 100% ($\Delta\chi$=0), and a constant fractional blood volume (BV) of 2% was assumed across all radii.

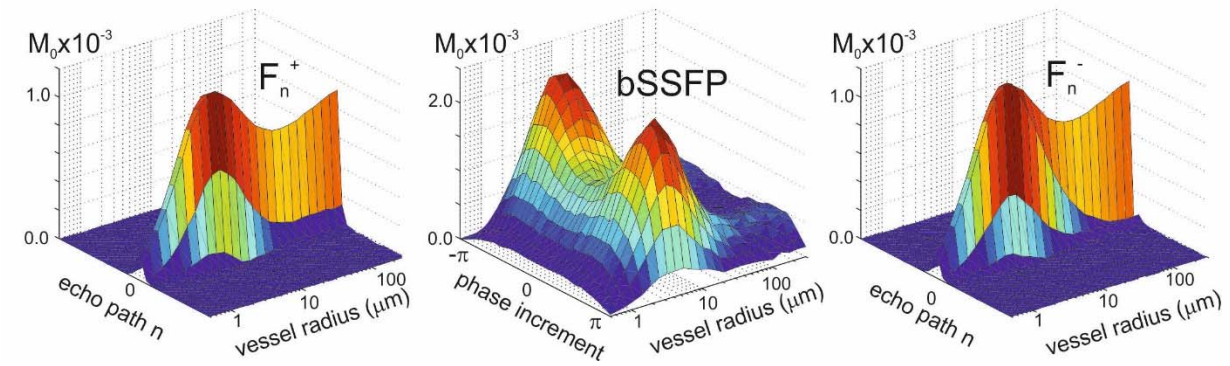

Fig. 1: Middle: simulated bSSFP profile centered between RF pulses (TE=TR/2) for 9T, 30° flip angle and TR=10ms (BV=2%, extravascular T_1=2190ms and T_2=43ms). Plotted signal intensities correspond to absolute signal differences between undisturbed bSSFP profile (100% oxygenation) and BOLD-reduced profile (80% oxygenation) in units of M_0x10^{-3}. Left and right are the configurations after (F^+_n) and before (F^-_n) the RF pulse, which correspond to the Fourier-transformed bSSFP profile shown in the middle.

The BOLD-related signal change, i.e. the signal difference between activated state S_A and resting state S_R were calculated as absolute signal differences (S_A-S_R) in units of M_0, rather than the widely used relative signal change (S_A-S_R)/S_R. The relative signal change cannot be used to compare the BOLD sensitivity across different sequences and field strengths. Statistical tests, for example a simple two-paired t-test that tests if mean values of two different time series $S_A(t)$ and $S_B(t)$ are statistically different, scale with (S_A-S_B) rather than with (S_A-S_R)/S_R. The noise or variance in S_A or S_B was assumed to be constant across all SSFP sequences independent of TR and field strength. This implies a constant signal acquisition time interval t_{ACQ} over TR (or constant ADC duty cycle TR/t_{ACQ}). This constant signal-to-noise (SNR) efficiency can be achieved, for example, by adapting the read out bandwidth to TR (decreased bandwidth for increased TR), or by acquiring multiple echoes for increased TR. The increase of SNR with field strength B_0 (or increase of M_0 with B_0) was not taken into account for a better comparison of field-dependent

effects. However, reported scaling of SNR with B_0 with the power of 1.5 to 1.7 (Pohmann, Pfrommer) can be multiplied to the calculated signal changes S_A-S_R to correct for field-dependent effects.

For Fig. 1 and 2, all signals were calculated as a function of the vessel radius, B_0, TR, flip angle, and constant BV of 2% and oxygenation changes between 100% and 80%. For Figs. 4 and 5, the sum and the ratio of the contributions from micro and macro vessels were calculated, respectively. Micro and macro vessels have been defined similar to the model used by Markuerkiaga et. al. and Khajehim et. al. (Markuerkiaga, Khajehim). Micro vessels or the laminar network were composed of arterioles having a radius between 5 and 15 µm, capillaries with a radius of 4 µm and venules or postcapillary vessels between 6 to 18 µm, according to the Vascular Anatomical Network (VAN) proposed by Boas et al. (Boas, Blinder). The fractional BV of micro vessels was 1% for venules, 0.8% for capillaries and 0.5% for arterioles (Weber). Oxygenation levels for the resting and activated state were set to 60% and 70% for venules, 77.5% and 85% for capillaries, and 95% and 100% for arterioles, respectively (Vovenko). Macro vessels were defined as intracortical veins diving perpendicular to the surface into the cortical layers and that flow into much larger pial veins located at the cortex surface. These larger pial vessels were not included in the macro vessel model. The radius of intracortical veins was equally distributed between 10 and 60 µm. The BV of intracortical veins gradually increases from 0.2% at the deepest layer up to 1% at the top layer, and may easily reach up to 5 to 10% at the pial surface (Duvernoy). For the simulations shown in Fig. 5 and 6 an average BV of 0.6% was assumed for intracortical veins that corresponds to an imaging voxel that covers the entire cortex, but excluding the pial surface vessels. Oxygenation levels of intracortical veins for the resting and activated state were set to 60% and 70%, respectively (Vovenko). The contribution of intracortical arteries was neglected, i.e. a constant oxygenation of 100% was assumed. Changes in BV between resting and activated states were not considered.

Measurements

Similar to (Bieri), measurements on 2% (v/v) precision polybead polystyrene microspheres (Polysciences Europe, with different diameters of 1, 2, 3, 4.5, 6, 15, 25, 45, and 90 µm, $\Delta\chi$ = 0.1 ppm, dispersed in 2% aqueous alginic acid solution to prevent sinking of larger micro spheres and 5 mM Dysprosium diethylene triaminepentaacetic acid [Dy-DTPA]) were performed at 3T (Siemens Prisma) with a non RF-spoiled GE or FISP (F^+_0 signal) and a PSIF (F^-_0 signal) sequence, both with a TR of 7.5ms and TE=2.2ms (after (F^+_0) and before (F^-_0) RF pulse), and nominal flip angles between 10 and 50°. T1 and T2 relaxation times from the tube without micro spheres were measured with inversion recovery and multi echo sequences. Flip angles across the tube phantom were measured with an actual flip-angle imaging (AFI) sequence (Yarnykh). The susceptibility difference between water and 5 mM Dy-DTPA was estimated via a B_0 field map. Corresponding Monte Carlo simulations were performed with spheres instead of cylinders, and adapted T1, T2 and susceptibility difference values as well as increased diffusion constant of free water ($2.3x10^{-9}m^2/s$) were used.

Results

Signal changes as a function of cylinder radius for different pathways are shown in Fig. 2 for flip angles between 10 and 50°, field strength of 7T and TR=10ms. The profiles have been calculated as coefficients of the Fourier transformed bSSFP profile and represent the BOLD signal change for different echoes or pathways after (+) and before (-) the RF pulse. All curves show signal changes in the order of 0.5 to 1.5 M_0x10^{-3}, which largely dependents on the chosen flip angle. Fig. 2 also demonstrates a strong dependence of signal changes on the underlying cylinder radius for all pathways with a peak signal change at the microvascular regime of about 5 to 10 µm radius. In the static dephasing regime for cylinders larger than about 10 µm in radius, both pathways F^+_0 and F^-_0 exhibit a typical spin echo behavior, i.e. signal dephasing is completely refocused for larger cylinder radii. Thus, not only

F^{-}_{0} (or S2-SSFP etc.) but also the conventional gradient echo path F^{+}_{0} are equally sensitive to the microvascular regime, and both suppress macrovascular contributions. The main difference of these two pathways to higher-order configurations is the increasing contribution from larger cylinders.

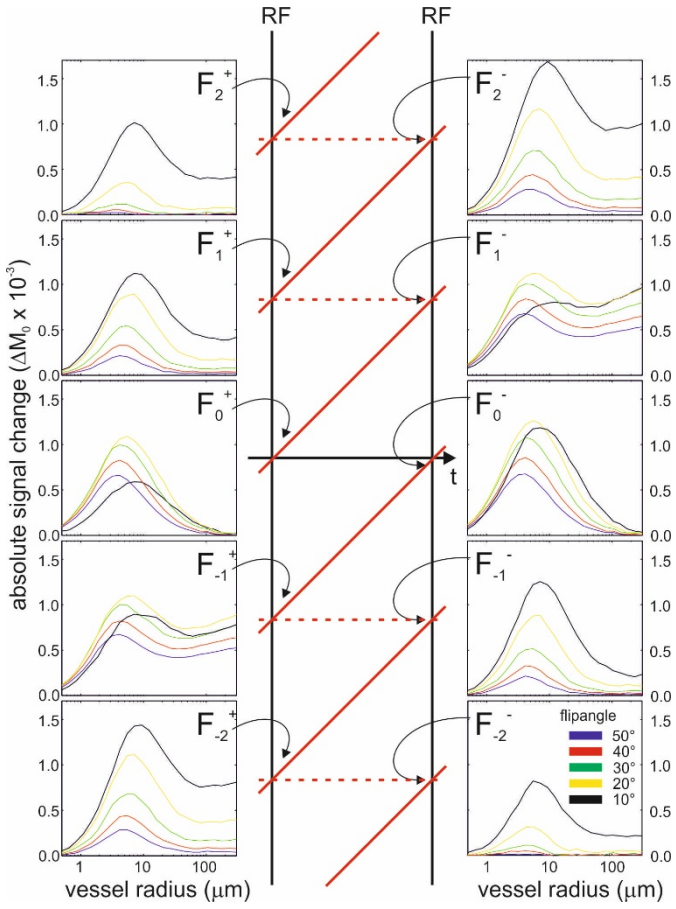

Fig. 2: BOLD signal change as a function of cylinder (vessel) radius for different post and pre RF pulse echo pathways of the non-balanced SSFP sequence at 7T and flip angles between 10 and 50°, and for TR=10ms and BV=2%. Red solid diagonal lines represent the transition between different echo paths.

The spin echo behavior of the F^{+}_{0} and F^{-}_{0} path was verified experimentally on micro spheres as shown in Fig. 3. Both sequences exhibit a signal recovery for spheres with radius larger than about 10 μm, as confirmed by Monte Carlo simulation shown

right. For these Monte Carlo simulations measured T1 and T2 values of 800 and 250ms were used, respectively. The measured flip angles across the 10 tubes shown in Fig. 3 varied by about 10% and shown experimental plots were corrected to exactly 10 to 50° by linear interpolation. The measured frequency difference between the signal from the tube without microspheres (filled with 2% alginic acid and 5 mM Dy-DTPA) and surrounding water was about 60 Hz, corresponding to a susceptibility difference of $\Delta\chi$ = 0.5 ppm. For the simulations, the resulting susceptibility difference between spheres and surrounding alginic acid/water/Dy-DTPA mixture was set to $\Delta\chi$ = 0.4 ppm. Only for Fig. 3 signal changes were calculated as relative signal changes to enable a comparison between experiments and simulations.

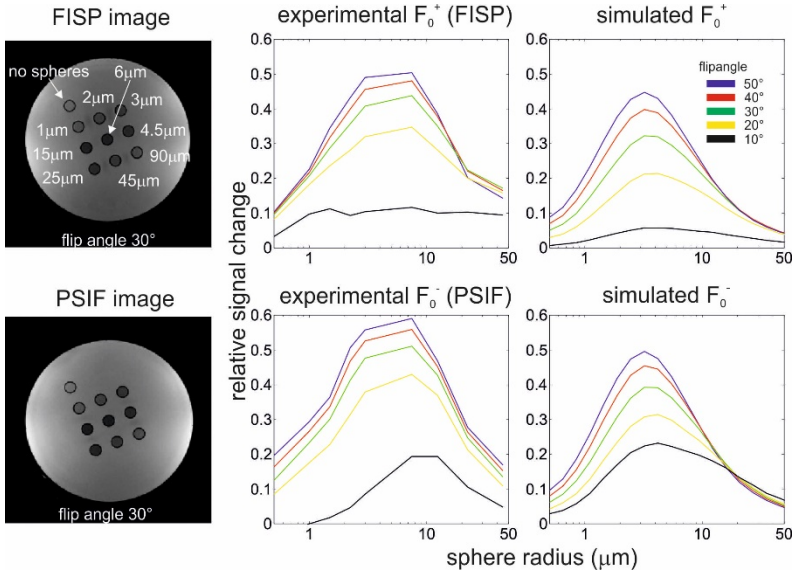

Fig. 3: Experimental verification of the spin echo behavior of the GRE (F^{+}_{0}) and PSIF (F^{-}_{0}) signal change in a phantom with microspheres of different diameter.

The colored surface plots shown in Fig. 4 show the weighted sum of micro and macro vascular signal changes between resting and activated state for field strengths between 1 and 15T, and TR between 5 and 45ms. Solid lines in the bottom row display peak signal changes (maximum signal changes for a given B_0 across the TR

range of 5 to 45 ms) for different flip angles and field strength. The dashed line shows the maximal signal change across TR and flip angle as a function of field strength. As described above, a total BV of 2.3% was assumed for micro vessels and 0.6% for macro vessels.

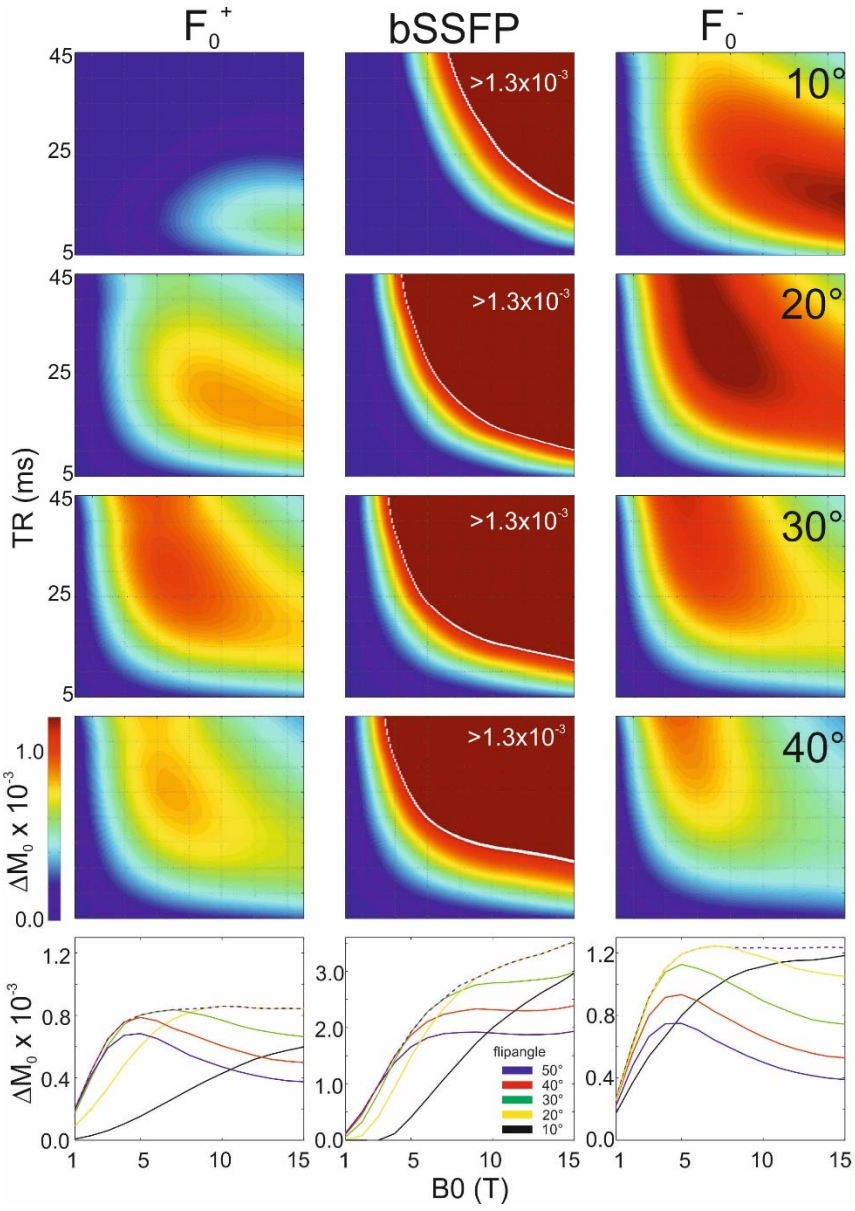

Fig. 4: BOLD signal changes produced by a weighted sum of micro (BV=2.3%) and macro (BV=0.6%) vascular contributions for F^{+}_{0}, bSSFP and F^{-}_{0} across a range of

TR from 5 to 45 ms and field strength B_0 between 1 and 15T. The solid lines in the bottom row show peak signal changes (maximum signal changes for a given B_0 along TR) for different flip angles and field strength. The dashed line shows the maximal signal change across TR and flip angle as a function of field strength.

Fig. 5 gives an overview on the microvascular weighting of the simulated BOLD signal change for F^+_0, bSSFP, F^-_0, GE and SE sequences as a function of TR (TE for GE and SE) and field strength. Microvascular weighting is defined as microvascular signal changes divided by signal changes from macro vessels, according to the chosen geometry, BV weighting and oxygenation changes described above. A high micro/macro vascular ration (up to 15 in F^+_0, bSSFP, F^-_0 and SE) represents a BOLD signal change that is mostly produced by micro vessels. All plots are scaled between zero and 15, except for GE that ranges between zero and 3. Similar to Fig. 4 these simulations do not include the contribution of pial vessels but assume an average BV of 2.3% for micro and 0.6% for macro vessels. The micro/macro vascular ratio is mainly controlled by the shape of the signal changes as a function of vessel radius, as shown in Figs. 1 to 3. Reduced signal changes for larger vessels (the static dephasing regime) will result in increased microvascular sensitivity or increased micro/macro vascular ratio.

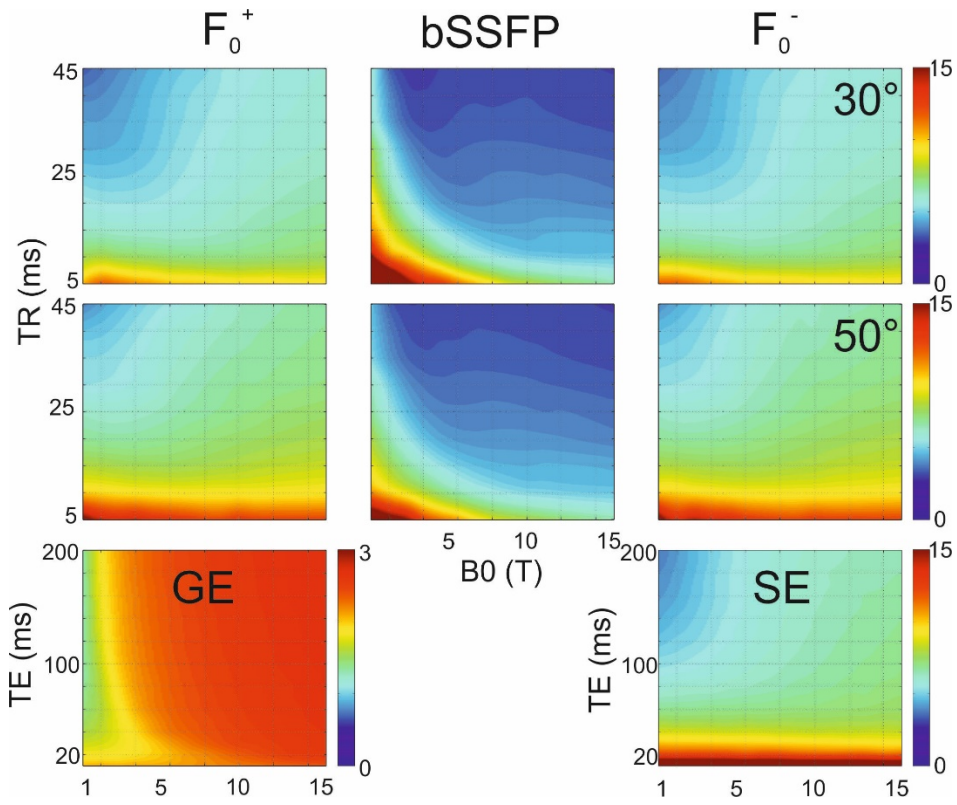

Fig. 5: Microvascular weighting (micro/macro signal changes) of the simulated BOLD signal change for F^{+}_{0}, bSSFP, F^{-}_{0}, GE and SE sequences as a function of field strength and TR (TE for GE and SE, and flip angle of 30 and 50 degrees for F^{+}_{0}, bSSFP and F^{-}_{0},). Both F^{+}_{0} and F_{-0} exhibit a similar behavior as SE. BSSFP has a strong microvascular component for short TR and lower field strengths. GE has a low microvascular weighting across all TE and field strengths.

Discussion

The well-known behavior of conventional GE and SE sequences to microscopic perturbers of different size has been described in the fundamental papers of Ogawa, Weisskopf, Boxerman and others (Ogawa, Weisskopf, Boxerman, Yablonskiy, Kiselev). Recently, rapid gradient echo sequences such as non-balanced and balanced SSFP have been proposed for functional BOLD imaging, and the signal properties of some selected types of SSFP variants have been analyzed experimentally, analytically and in Monte Carlo simulations (Miller, Bieri, Baez,

Khajehim, Barth). Based on Monte Carlo simulations, this paper gives a systematic overview on the signal properties of different echo pathways of SSFP (including balanced SSFP, GE and SE) in a microvascular environment across different sequence parameters and field strengths.

In several studies, the F^{-}_{0} or PSIF, CE-FAST, T2-FFE, or S2-SSFP signal has been proposed for functional BOLD imaging. This signal is largely composed of RF-refocused components (Zur) and therefore exhibits a largely reduced sensitivity for larger vessels, similar to the conventional SE sequence. This behavior is confirmed in Figs. 1 to 5. However, as shown in Fig. 2, a similar signal shape is generated for other coherence pathways of SSFP. Especially the F^{+}_{0} and F^{-}_{0} components are very similar to the SE signal properties, which is confirmed in the experimental results on microspheres shown in Fig. 3. However, higher order pathways tend to show an increased signal contribution from larger vessels. Therefore, both the F^{+}_{0} and F^{-}_{0} signals are equally well suited as “spin echo” BOLD sequence, although F^{-}_{0} exhibits about 20 to 30% higher signal changes compared to F^{+}_{0}. The spin echo behavior of the steady state echo F^{+}_{0} and F^{-}_{0} was already theoretically predicted for static dephasing within a Lorentzian frequency distribution by Ganter. This regime is similar to the quasi static dephasing regime for vessel radii larger then about 50 µm, as the diffusion length within TR is much smaller than the large vessel size. All echo paths show a strong dependence of signal changes as well as a slight shift of the peak sensitivity on the flip angle. Signal changes are highest for flip angles around 10 to 20°, which might be beneficial for high-field applications in terms of SAR constrains.

To calculate the field dependence of the signal change, a certain neurovascular structure composed of micro and macro vascular vessels was assumed. The results shown in Fig. 4 (and Fig. 5) strongly depend on the underlying vessel composition, their fractional volume occupancy as well as on the selected levels and changes in local blood oxygenation between resting and activated state within these specific vessel types. The parameters used to define micro and macro vessels are largely consistent with literature values and have also been used for other similar Monte

Carlo simulation studies (Markuerkiaga, Baez, Khajehim). Larger veins such as the surface pial veins were not included, which might bias the presented results compared to experimental studies that include these veins. Therefore, values shown in Fig. 4 represent intracortical signal changes only, inclusion of larger surface or draining veins might significantly boost signal changes due to their large BV and potential intravascular signal contribution.

The signal change of F^{+}_{0} and F^{-}_{0} depends on the selected TR and on field strength. Both sequences show a confined range of optimal TR and field strength that maximizes the corresponding signal change. BSSFP has about two times larger signal changes for long TR compared to F^{+}_{0} and F^{-}_{0}. This is mainly due to the effect that bSSFP becomes less refocused for larger vessels at long TR and low flip angles (Bieri, Baez), which increases the macrovascular signal contribution. The bottom plots in Fig. 4 show the maximal signal changes as a function of field strength for different flip angles (solid lines) and for optimal flip angles (dashed line). Interestingly, both F^{+}_{0} and F^{-}_{0} components show a very small signal change increase for fields larger than about 5T for optimized TR and flip angle. However, for small TR under 10ms (which results in a stronger microvascular signal contribution, see Fig. 4) the signal change always increases with field strength for all sequence types. Note that all calculations assume a constant M_0 and do not include the increase of SNR with B_0 with the power of 1.5 to 1.7 (Pohmann, Pfrommer).

A comparison between the BOLD efficiency, i.e. the absolute BOLD-related signal change over SNR per unit time, between SSFP and GE and SE sequences is challenging due to several unknown parameters. Assuming a constant SNR and signal stability across all sequences, i.e. identical RF receive coil performance, identical acquisition efficiency (ADC signal conversions per unit time) and identical temporal fluctuations caused by scanner instabilities and physiological noise, it is sufficient to compare absolute BOLD-related signal changes across sequences. F^{+}_{0} and F^{-}_{0} show a signal change of about 0.8 to 1.3 $M_0 x 10^{-3}$. In contrast, SE produces a weighted averaged signal change of micro and macrovascular vessels of about 10

to 15 M_0x10^{-3}, based on similar Monte Carlo simulations and assuming a fully unsaturated initial M_0 magnetization. This corresponds to an increased BOLD efficiency of SE of a factor of about 10 over F^+_0 and F^-_0. However, for short TRs in the range or below T1 will reduce the SE signal change by a factor of about 5 to 10 due to saturation by the excitation and refocusing pulse. Furthermore, there is a significant T2*-related signal decay along the SE-EPI readout that might account for a further signal reduction. Depending on the chosen parameters, resulting signal changes are finally similar between SE and SSFP. The averaged GE signal change is about 3 to 5 times higher than for SE (mainly due to the large vessel contribution), and thus also about 3 to 5 times more sensitive compared to SSFP. These simulated results are comparable to measured signal changes at different field strength for GE, SE, S2-SSFP and bSSFP (Budde, Duong, Yacoub, Schäfer, Boyacioğlu, Barth, Scheffler).

A possible benchmark to characterize the spatial proximity between neuronal events and measured BOLD response is the ratio between micro and macrovascular signal changes (Uludag, Pflugfelder). This ratio is plotted in Fig. 5 for the three SSFP types and for comparison also for GE and SE. In general, except for GE all sequences show strongly increasing microvascular sensitivity for shorter TR (and TE for SE). For very long TR the sensitive drops down to the range of the GE sensitivity. This is especially true for the centered bSSFP echo (at TE=TR/2 between RF pulses) that is sensitive to T2* dephasing effects. Therefore, the strong total signal changes for bSSFP at long TR shown in Fig. 4 is dominated by GE effects (i.e. contribution from larger vessels) which is reflected in the very low micro/macro ratio shown in Fig. 5. For F^+_0, F^-_0 and SE micro/macro ratio does not significantly depend on field strength except for very long TR. In addition, this ratio is very similar for F^+_0, F^-_0 and SE, supporting the almost pure SE behavior of F^+_0 and F^-_0. For bSSFP this ratio decreases with field strength which is again caused by an increased T2* contribution towards higher fields and which can be compensated by a reduction of TR.

The composition of micro and macro vessels used in our simulations significantly differs from those used in Uludag and Pflugfelder. In these papers, micro vessels were composed of two single radii of 2.5 and 8 µm (average BV of 2.5%), and macro vessels of a single radius of 100 µm (BV of 5%) oriented perpendicular to the main field. Therefore, this micro/macrovascular ratio represents the ratio between parenchymal and pial BOLD contributions. In this paper, macro vessels were defined as intracortical draining venules/veins with only 0.6% BV in average without larger pial veins, similar to the model used by Markuerkiaga. Therefore, BOLD signal ratios shown in Fig. 5 are not directly comparable to those shown in Uludag and Pflugfelder.

The results shown in Fig. 5 assume randomly oriented vessels, which is probably not appropriate for the intracortical draining veins. Thus, the micro/macro vascular ratio is biased by the local orientation of the cortex surface to B_0. These orientational effects have been described experimentally and in simulations (Gagnon, Baez, Fracasso). Orientations of the cortex surface perpendicular to B_0 (or veins parallel to B_0) will thus increase microvascular contributions and vice versa.

Simulations did not include contributions of intravascular signals as well as no changes in BV. To estimate the steady state blood signal for rapid SSFP, approximated R1 and R2 relaxivities of blood have to be used. Following Khajehim, R1 as a function of B_0 can be expressed as $R1 = 0.0014*B_0^2-0.0502B_0+0.7462$. This equation does not take into account the weak dependence of R1 on the oxygenation level Y, as demonstrated in (Blockley). For R2 an expression derived from single echo experiments can be applied, $R2(B_0,Y) = 2.74B_0 -0.6 + 12.67B_0^2(1-Y)^2$, which additionally depends on oxygenation Y (Uludag, Khajehim). However, R2 values derived from single echo experiments might not be fully apply for rapidly refocused SSFP sequences (Dharmakumar), as R2 tends to decrease with decreasing RF spacing. Assuming an approximated steady state signal of $0.5M_0*sqrt(R1/R2)$, an averaged intravascular oxygenation change from Y=75% at rest to 85% during activation, and an average cortical BV of 2.3% (excluding pial vessels), the resulting intravascular signal change is in the order of $3*M_0x10^{-4}$ at 1T and decreases to about

$1*M_0x10^{-4}$ at 15T. Therefore, at very high fields the intravascular-related signal change is about 10 to 20 times smaller compared to the extravascular contribution. At lower fields these contributions tend to become similar.

An increase of local BV during activation was not considered in this paper. BOLD-induced signal changes scale approximately linear with BV (Baez, Kiselev), and there is ongoing discussion whether these changes are more located at the draining venous side, which then produces some BOLD changes, or feeding arteriole side (Griffeth). Therefore, an estimation of possible changes especially for the micro/macro vascular signal ratio related to BV changes is challenging.

Conclusion

The coherence pathways of rapid SSFP sequences show a strong refocusing effect within the static dephasing regime. As a result, both the conventional rapid gradient echo F^+_0 as well as the reversed F^-_0 echo (and to a less extend also higher order echoes) are sensitive to only small vessels, which is similar to the SE behavior.

References:

Constable, R.T., Kennan, R.P., Puce, A., McCarthy, G., Gore, J.C., 1994. Functional NMR imaging using fast spin echo at 1.5 T. Magn. Reson. Med. 31 (6), 686–690.

Poser, B.A., Norris, D.G., 2007. Fast spin echo sequences for bold functional MRI. Magma 20 (1), 11–17.

Chamberlain, R., Park, J.-Y., Corum, C., Yacoub, E., Ugurbil, K., Jack, C.R., Garwood, M.,2007. RASER: a new ultrafast magnetic resonance imaging method. Magn. Reson. Med. 58 (4), 794–799.

Bandettini, P.A., Wong, E.C., Jesmanowicz, A., Hinks, R.S., Hyde, J.S., 1994. Spin-echo and gradient-echo EPI of human brain activation using BOLD contrast: a comparative study at 1.5 T. NMR Biomed. 7 (1–2), 12–20.

Feinberg, D.A., Harel, N., Ramanna, S., Ugurbil, K., Yacoub, E., 2008. Sub-millimeter single-shot 3D GRASE with inner volume selection for T2 weighted fMRI applications at 7 Tesla. Proceedings 16th Annual Meeting International Society for Magnetic Resonance in Medicine, p. 2373.

Yacoub, E., Harel, N., Ugurbil, K., 2008. High-field fMRI unveils orientation columns in humans. Proc. Natl. Acad. Sci. U. S. A. 105 (30), 10607–10612.

Ogawa, S., Menon, R.S., Tank, D.W., Kim, S.G., Merkle, H., Ellermann, J.M., Ugurbil, K., 1993. Functional brain mapping by blood oxygenation level-dependent contrast magnetic resonance imaging. A comparison of signal characteristics with a biophysical model. Biophys. J. 64 (3), 803–812.

Weisskoff, R., et al., 1994. Microscopic susceptibility variation and transverse relaxation: Theory and experiment. Magn. Reson. Med. 31, 601–610.

Boxerman, J. L., Bandettini, P. A., Kwong, K. K., Baker, J. R., Davis, T. L., Rosen, B. R., & Weisskoff, R. M. (1995). The intravascular contribution to fMRI signal change: Monte Carlo modeling and diffusion-weighted studies in vivo. *Magnetic Resonance in Medicine*, *34*(1), 4–10.

Barth, M., Meyer, H., Kannengiesser, S. A. R., Polimeni, J. R., Wald, L. L., & Norris, D. G. (2010). T2 weighted 3D fMRI using S2-SSFP at 7 Tesla. *Magnetic Resonance in Medicine*, *63*(4), 1015–1020.

Goa PE, Koopmans PJ, Poser BA, Barth M, Norris DG. BOLD fMRI signal characteristics of S1- and S2-SSFP at 7 Tesla. Front Neurosci. 2014 Mar 13;8:49.

Khajehim M, Nasiraei Moghaddam A. Investigating the spatial specificity of S2-SSFP fMRI: A Monte Carlo simulation approach. Magn Reson Imaging. 2017 Apr;37:282-289. doi: 10.1016/j.mri.2016.11.016. Epub 2016 Nov 24.

Scheffler K, Seifritz E, Bilecen D, Venkatesan R, Hennig J, Deimling M, Haacke EM. Detection of BOLD changes by means of a frequency-sensitive trueFISP technique: preliminary results. NMR Biomed. 2001 Nov-Dec;14(7-8):490-6.

Miller, K.L., 2102. FMRI using balanced steady-state free precession (SSFP). NeuroImage 62, 713–719.

Ehses P, Scheffler K. Multiline balanced SSFP for rapid functional imaging at ultrahigh field. Magn Reson Med. 2018 Feb;79(2):994-1000.

Scheffler K, Ehses P. High-resolution mapping of neuronal activation with balanced SSFP at 9.4 tesla. Magn Reson Med. 2016 Jul;76(1):163-71.

Kaibao Sun, Rong Xue, Peng Zhang, Zhentao Zuo, Zhongwei Chen, Bo Wang, Thomas Martin, Yi Wang, Lin Chen, Sheng He, Danny J.J. Wang. Integrated SSFP for functional brain mapping at 7 T with reduced susceptibility artifact. Journal of Magnetic Resonance Volume 276, March 2017, Pages 22-30

Yablonskiy DA, Haacke EM. Theory of NMR signal behavior in magnetically inhomogeneous tissues: the static dephasing regime. Magn Reson Med. 1994 Dec;32(6):749-63.

Kiselev VG, Posse S. Analytical model of susceptibility-induced MR signal dephasing: effect of diffusion in a microvascular network. Magn Reson Med. 1999 Mar;41(3):499-509.

Norris DG. Spin-echo fMRI: The poor relation? NeuroImage 62 (2012) 1109–1115.

R. Kaiser, E. Bartholdi, R.R. Ernst, Diffusion and field gradient effects in NMR Fourier spectroscopy, J. Chem. Phys. 60 (1974) 2966–2979.

Scheffler K. A Pictorial Description of Steady-States in Rapid Magnetic Resonance Imaging.Concepts in Magnetic Resonance, Vol. 11(5) 291–304 (1999).

Báez-Yánez MG, Ehses P, Mirkes C, Tsai PS, Kleinfeld D, Scheffler K. The impact of vessel size, orientation and intravascular contribution on the neurovascular

fingerprint of BOLD bSSFP fMRI. Neuroimage. 2017 Sep 8;163:13-23. doi: 10.1016/j.neuroimage.2017.09.015.

Bieri, O., Scheffler, K., 2007. Effect of diffusion in inhomogeneous magnetic fields on balanced steady-state free precession. NMR Biomed. 20, 1–10.

Uludağ K, Müller-Bierl B, Uğurbil K. An integrative model for neuronal activity-induced signal changes for gradient and spin echo functional imaging. Neuroimage 2009; 48:150–65.

Pohmann R, Speck O, Scheffler K. Signal-to-noise ratio and MR tissue parameters in human brain imaging at 3, 7, and 9.4 tesla using current receive coil arrays. Magn Reson Med. 2016 Feb;75(2):801-9.

Pfrommer A, Henning A. The ultimate intrinsic signal-to-noise ratio of loop- and dipole-like current patterns in a realistic human head model. Magn Reson Med. 2018 Mar 13. doi: 10.1002/mrm.27169. [Epub ahead of print]

Markuerkiaga, I., et al., 2016. A cortical vascular model for examining the specificity of the laminar BOLD signal. NeuroImage. 132, 491–498.

Boas, D.A., et al., 2008. A vascular anatomical network model of the spatio-temporal response to brain activation. NeuroImage 40 (3), 1116–1129.

Blinder, P., et al., 2013. The cortical angiome: an interconnected vascular network with noncolumnar patterns of blood flow. Nature Neuroscience 15 (7), 889-97.

Weber, B., et al., 2008. The microvascular system of the striate and extrastriate visual cortex of the macaque. Cereb Cortex. 18 (10), 2318-30.

Duvernoy, H.M., et al., 1981. Cortical blood vessels of the human brain. Brain Res. Bull. 7 (5), 519–579.

Vovenko, E., 1999. Distribution of oxygen tension on the surface of arterioles, capillaries and venules of brain cortex and in tissue in normoxia: an experimental study on rats. Pflugers Arch. 437 (4), 617-23.

Y. Zur, M.L. Wood, L.J. Neuringer, Motion insensitive steady-state free precession imaging, Magn. Reson. Med. 16 (1990) 444–459.

Ganter C. Static susceptibility effects in balanced SSFP sequences. Magn Reson Med. 2006 Sep;56(3):687-91.

Gagnon, L., et al., 2015. Quantifying the microvascular origin of BOLD-fMRI from first principles with two-photon microscopy and an oxygen-sensitive nanoprobe. J. Neurosci. 35 (8), 3663–3675.

Fracasso A, Luijten PR, Dumoulin SO, Petridou N. Laminar imaging of positive and negative BOLD in human visual cortex at 7T. Neuroimage. 2018 Jan 1; 164:100-111.

Blockley, N.P., et al., 2008. Field Strength Dependence of R1 and R*2 Relaxivities of Human Whole Blood to ProHance, Vasovist, and Deoxyhemoglobin. Magn. Reson. Med. 60,1313–1320.

Valerie E.M. Griffeth, Richard B. Buxton. A theoretical framework for estimating cerebral oxygen metabolism changes using the calibrated-BOLD method: Modeling the effects of blood volume distribution, hematocrit, oxygen extraction fraction, and tissue signal properties on the BOLD signal. NeuroImage Volume 58, Issue 1, 1 September 2011, Pages 198-212

Budde J, Shajan G, Zaitsev M, Scheffler K, Pohmann P. Functional MRI in Human Subjects with Gradient-Echo and Spin-Echo EPI at 9.4 T. Magn Reson Med. 2014; 71:209–218.

Duong TQ, Yacoub E, Adriany G, Hu X, Ugurbil K, Kim SG. Microvascular BOLD contribution at 4 and 7 T in the human brain: gradient-echo and spin-echo fMRI with suppression of blood effects. in Magn Reson Med. 2003 Jun;49(6):1019-27.

Yacoub E, Duong TQ, Van De Moortele PF, Lindquist M, Adriany G, Kim SG, Uğurbil K, Hu X. Spin-echo fMRI in humans using high spatial resolutions and high magnetic fields. Magn Reson Med. 2003 Apr;49(4):655-64.

Schäfer A, van der Zwaag W, Francis ST, Head KE, Gowland PA, Bowtell RW. High resolution SE-fMRI in humans at 3 and 7 T using a motor task. MAGMA. 2008 Mar;21(1-2):113-20.

Boyacioğlu R, Schulz J, Müller NC, Koopmans PJ, Barth M, Norris DG. Whole brain, high resolution multiband spin-echo EPI fMRI at 7 T: a comparison with gradient-echo EPI using a color-word Stroop task. Neuroimage. 2014 Aug 15;97:142-50.

V.L. Yarnykh. Actual flip-angle imaging in the pulsed steady state: a method for rapid three-dimensional mapping of the transmitted radiofrequency field Magn Reson Med, 57 (2007), pp. 192-200